UNIVERSITY OF MIAMI

ON THE RESPONSE TO TROPICAL CYCLONES IN MESOSCALE OCEANIC EDDIES

By

Benjamin Jaimes

A DISSERTATION

Submitted to the Faculty
of the University of Miami
in partial fulfillment of the requirements for
the degree of Doctor of Philosophy

Coral Gables, Florida

December 2009

UNIVERSITY OF MIAMI

A dissertation submitted in partial fulfillment of
the requirements for the degree of
Doctor of Philosophy

ON THE RESPONSE TO TROPICAL CYCLONES IN MESOSCALE OCEANIC EDDIES

Benjamin Jaimes

Approved:

Lynn K. Shay, Ph.D. Committee Chair and Professor of Meteorology and Physical Oceanography	Terri A. Scandura, Ph.D. Dean of the Graduate School
George H. Halliwell, Ph.D. Oceanographer NOAA/AOML/PhOD Miami, Florida	William E. Johns, Ph.D. Professor of Meteorology and Physical Oceanography
Kevin D. Leaman, Ph.D. Professor of Meteorology and Physical Oceanography	Mark D. Powell, Ph.D. Atmospheric Scientist NOAA/AOML/Hurricane Research Division Miami, Florida

JAIMES, BENJAMIN (Ph.D., Meteorology and Physical Oceanography)
On the Response to Tropical Cyclones in Mesoscale Oceanic Eddies (December 2009)

Abstract of a dissertation at the University of Miami.

Dissertation supervised by Professor Lynn K. Shay.
No. of pages in text. (145)

Tropical cyclones (TCs) often change intensity as they move over mesoscale oceanic features, as a function of the oceanic mixed layer (OML) thermal response (cooling) to the storm's wind stress. For example, observational evidence indicates that TCs in the Gulf of Mexico rapidly weaken over cyclonic cold core eddies (CCEs) where the cooling response is enhanced, and they rapidly intensify over anticyclonic warm features such as the Loop Current (LC) and Warm Core Eddies (WCEs) where OML cooling is reduced. Understanding this contrasting thermal response has important implications for oceanic feedback to TCs' intensity in forecasting models. Based on numerical experimentation and data acquired during hurricanes Katrina and Rita, this dissertation delineates the contrasting velocity and thermal response to TCs in mesoscale oceanic eddies.

Observational evidence and model results indicate that, during the forced stage, the wind-driven horizontal current divergence under the storm's eye is affected by the underlying geostrophic circulation. Upwelling (downwelling) regimes develop when the wind stress vector is with (against) the geostrophic OML velocity vector. During the relaxation stage, background geostrophic circulations modulate vertical dispersion of OML near-inertial energy. The near-inertial velocity response is subsequently shifted

toward more sub-inertial frequencies inside WCEs, where rapid vertical dispersion prevents accumulation of kinetic energy in the OML that reduces vertical shears and layer cooling. By contrast, near-inertial oscillations are vertically trapped in OMLs inside CCEs that increases vertical shears and entrainment. Estimates of downward vertical radiation of near-inertial wave energies were significantly stronger in the LC bulge (12.1×10^{-2} W m^{-2}) compared to that in CCEs (1.8×10^{-2} W m^{-2}).

The rotational and translation properties of the geostrophic eddies have an important impact on the internal wave wake produced by TCs. More near-inertial kinetic energy is horizontally trapped in more rapidly rotating eddies. This response enhances vertical shear development and mixing. Moreover, the upper ocean temperature anomaly and near-inertial oscillations induced by TCs are transported by the westward-propagating geostrophic eddies. From a broader perspective, coupled models must capture oceanic features to reproduce the differentiated TC-induced OML cooling to improve intensity forecasting.

This dissertation is dedicated to my wife Sandra, and my children Andrea and Victor.

Acknowledgements

My first, and most sincere, acknowledgment must go to the advisor and chair of my Ph.D. committee, Dr. Lynn "Nick" Shay. Nearly four years ago, at the peak of the historic 2005 hurricane season, I had the good fortune to become his student. Ever since, Nick has inspired me with his passion for science, has given me the freedom to pursue my scientific research interest, and has been instrumental in ensuring my academic, professional, and financial well being. I am also grateful to committee members Drs. George Halliwell, William Johns, Kevin Leaman, and Mark Powell, whose oral and written comments were always extremely perceptive, helpful, and appropriate.

I also owe a huge debt of gratitude to several people that were instrumental during my journey toward the Ph.D. degree. My uncle, Manuel Alonso, detonated my early scientific curiosity with his passionate speeches on science. Dr. Juan Luis Peña nominated me for the Fulbright-Garcia Robles scholarship, which made it possible for me to come to the United States to pursue the Ph.D. degree. Linda Smith believed in me and turned on the light in the darkest night of my life.

During my years at RSMAS, I had the fortune to coexist in Room 234B with a group of people that, like me, came from a remote place, full of hope and determination to accomplish personal and scientific goals. I shared countless days, good and bad ones, with Marcello, Xioabio, Tania, John, Ben, and Marcela. My utmost appreciation goes out to you guys for your friendship, support, and fantastic food on those unforgettable days. I also wish to thank my group-mates Jodi, Pat, and Jorge, for their friendly support during this difficult, but fun, journey.

I also would like to thank several institutions that provided financial support for this work, via scholarships or grants: Fulbright-Garcia Robles Commission, CONACyT (Mexico), NSF, and NOAA Joint Hurricane Testbed program.

I am grateful for the efforts of the pilots, technicians, engineers, and scientists at NOAA's Aircraft Operation Center (Dr. Jim McFadden) and Hurricane Research Division (Dr. Frank Marks), who made it possible to acquire the data presented in this research. Mooring data were supported by Mineral Management Service to Evans-Hamilton Inc.

My final, and most heartfelt acknowledgment, must go to my wife, Sandra, and my children, Andrea and Victor. Their support, encouragement, and companionship turned my journey toward obtaining the Ph.D. degree into a pleasure. You guys have my everlasting love.

Contents

List of Figures x

List of Tables xxiv

List of Abbreviations xxviii

1 Introduction 1

1.1 Motivation 6

1.2 Statement of the problem 7

1.2.1 Research issues 9

1.2.2 Goal and objectives 13

1.2.3 Value of work 14

1.3 Research approach 14

1.3.1 Observational approach 15

1.3.2 Numerical studies 15

1.4 Outline 17

2 Methodology and Data 18

2.1 Observational data 18

2.1.1 Airborne measurements 18

2.1.2 Mooring data 22

2.1.3 Wind stress 23

2.1.4 Geostrophic circulation 23

2.1.5 Isotherm depth and sea surface height from altimetry 27

2.2 Hurricanes Katrina and Rita 28

2.2.1 Hurricane Katrina and mesoscale ocean variability 28

2.2.2 Hurricane Rita and mesoscale ocean variability 32

3 Forced Stage **34**

3.1 Thermal structure in the Loop Current system 34

3.1.1 Isotherm topography 34

3.1.2 Ocean thermal structure and storm intensity changes 35

3.2 Oceanic mixed layer cooling 37

3.3 Upwelling 39

3.4 Oceanic mixed layer velocity response 43

3.5 Depletion of the energy source 45

3.6 Summary and concluding remarks 51

4 Near-Inertial Wave Wake **53**

4.1 Processes involved 53

4.2 Near-inertial velocity response 56

4.3 Near-inertial temperature response 59

4.3.1 Vertical shear 59

4.3.2 Water mass evolution 62

4.3.3 Cold wake 62

4.4 Modulation of the near-inertial response 66

4.4.1 Near-inertial wave ray tracing 66

4.4.2 Effective Coriolis frequency 70

4.4.3 Frequency shifting 74

4.4.4 Vertical wavenumber spectrum 77

4.4.5 Contribution to the global internal wave power 80

4.5 The critical layer in the cold core eddy 82

4.5.1 Amplification of near-inertial waves 82

4.5.2 Relative contribution of buoyancy 85

4.5.3 Surface maximum of cyclonic relative vorticity 86

4.5.4 Origin of upgoing near-inertial waves 87

4.6 Summary and concluding remarks 88

5 Numerical Studies **91**

5.1 Ocean model 93

5.1.1 Numerical domain 94

5.1.2 Analytical model 96

5.1.3 Wind forcing 98

5.1.4 Experiments 99

5.2 Hurricane-induced upwelling in a quasi-geostrophic vortex 102

5.3 OML deepening 107

5.3.1 Entrainment model 108

5.3.2 Wind erosion during the forced stage 110

5.3.3 Shear-driven entrainment 112

5.4 Near-inertial velocity response 114

5.4.1 Decay of oceanic mixed layer near-inertial currents 114

5.4.2 Frequency shifting 120

5.4.3 Vertical wavenumber spectrum 122

5.5 Critical layer in the cold core eddy 124

5.6 Trapped internal wave wake 125

5.7 Effects of the vertical resolution 127

5.8 Summary and concluding remarks 129

6 Summary and Discussion **132**

Bibliography **136**

List of Figures

1.1 Spatial frequency (%) for the location of WCE and CCE centers in the Gulf of Mexico. (a) WCE centers using a 27-year (1977-2003) database. (b) CCE centers using a 12-year (1992-2003) database (Vukovich 2007) 5

1.2 OML topography in the eastern Gulf of Mexico on 15 September, 2005, from airborne measurements of the thermal structure. The OML base is defined as the depth of the first occurrence of $T_{oml} - T(z) > 0.5^{o}$C, where this difference is computed downward from a depth of 2 m at intervals of 2 m. T is temperature, and T_{oml} is vertically-averaged temperature upon the upper 20 m. Red and blue shades represent WCEs and CCEs, respectively 6

2.1 Airborne profilers deployed in September 2005 relative to the track and intensity of TCs Katrina and Rita (colored lines, with color indicating intensity as per the legend) over the LC System. The light-gray shades on the sides of the storm tracks represent twice the radius of maximum winds (R_{max}). The contours are envelops of anticyclonic (solid: WCE and LC) and cyclonic (dashed: CCE1 and CCE2) circulations. A set of AXBTs (not shown) was deployed after hurricane Rita (26 September), following a sampling pattern similar to pre-Rita (or post Katrina) (15 September). See Tables 2.1 and 2.2 for a description of collected data and legends. Point M indicates the position of MMS moorings used during this study, and Point C represents the drop site

for profiler comparison (AXBT versus AXCTD). The horizontal line along 27°N indicates the extent of vertical sections discussed in the text..... 19

2.2 Evaluation of airborne profilers performance during the pre-Rita flight (15 September). (a) Comparison of three drops (two AXCTDs and one AXBT) in the center of the WCE (point C, Fig. 2.1). (b) Water mass distribution in the LC System from AXCTDs: Subtropical Water (STW), and Subantarctic Intermediate Water (SAAIW)..... 21

2.3 Evolution of isotherms at the mooring site (point M, Fig. 2.1) from CTD measurements. (a) Katrina, and (b) Rita. The vertical lines indicate the time of closest approach of the hurricane's eye to the mooring site (29 August for Katrina, and 23 September for Rita). IP stands for inertial period 24

2.4 (a) Water mass distribution in the LC System on 15 September (between the passage of hurricanes Katrina and Rita), from reference AXCTDs and extended AXBTs and AXCPs (see text for details). (b) Vertical section of the geostrophic circulation of both the WCE and CCE2 at 27°N (horizontal line in Fig. 2.1), derived from the density field in (a); the color scale is for geostrophic relative vorticity ζ_g (positive is cyclonic, and negative is anticyclonic), normalized by the local Coriolis frequency f=6.62×10^{-5} s^{-1}; contours are for the meridional geostrophic velocity, with positive (negative) values indicating northward (southward) velocity..... 26

2.5 Evaluation of the altimeter-based 26°C isotherm depth h_{26}. In situ h_{26} was calculated from airborne temperature profilers and ocean drifters. The ocean drifters are of the type Autonomous Drifting Ocean Station (ADOS), and were deployed on September 21 ahead of Rita in the Gulf of Mexico (Lumpkin and Pazos 2007). Altimeter-based and in situ h_{26} were objectively-analyzed into a $1/8^{o}\times1/8^{o}$ grid for this point-wise comparison 27

2.6 Comparison of 1-day η (left panels) and 7-day AVISO (right panels). Color scale is altimeter-based absolute dynamic sea surface height (SSH). (c, g) Black circle is the position of the storm's center. Point M represents the mooring used in this study 29

2.7 Comparison of 1-day η and 7-day AVISO (from Fig. 2.6). The scatter plots in (a)–(d) are from point-wise comparisons between the two SSH products, conducted over a window from 94°W–85°W and from 22°N–29°N. The correlation coefficients were 0.92, 0.94, 0.92, and 0.94 for (a), (b), (c), and (d), respectively. In general, 7 to 9% of the data were not considered in the individual analysis as they exceeded the range of three standard deviations. Histograms of the difference between the two products [(e)–(h)] were calculated based on data from the scatter plots (Jaimes and Shay 2009a). 30

2.8 Mesoscale ocean variability during Katrina and Rita. Color scale in (a, b) is altimeter-based absolute dynamic SSH from 1-day η, and circular magenta

contours stand for standard 10-m wind speed from the NOAA H*Wind product. The external, intermediate, and inner wind circles in (a, b) are the lower limit of tropical storm winds (18 m s^{-1}), winds at saturated level (28 m s^{-1}), and category 1 hurricane winds (33 m s^{-1}), respectively. (c) Loop Current cycle from altimeter-based h_{26} (h_{26} is area-averaged within a box from 93–81°W and 22–28.5°N in the Loop Current region)..... 31

3.1 Thermal structure in the LC system before (15 September, left panels) and after (26 September, right panels) the passage of hurricane Rita, from airborne profilers. (a) and (b) The h_{26} topography; the color shade shows regions with mapping error less than 40% from the objective analysis technique. (c) and (d) are zonal vertical sections of temperature across 26°N [indicated by arrows in (a) and (b)]. Color in the best-track lines stands for storm intensity as per the legend..... 36

3.2 Along-track conditions during TCs (a) Katrina and (b) Rita. The time series were constructed with conditions at the actual position of the storm. h_{26} is altimeter-based and normalized by 60 m, while SST is normalized by 30°C. The error bars in h_{26} indicate variability within a half longitudinal degree on each side of the best-track. The maxims in h_{26} in (a) and (b) are associated with the LC bulge, while the minimum h_{26} in (b) is associated with CCE1..... 38

3.3 Upper-ocean temperature changes induced by hurricane Rita: (a) LC bulge, (b) cyclonic circulation of the growing CCE1 (between the WCE and LC, ~90°W, 26.5°N). Temperature profiles represent cluster-averaged values from airborne data. Pre-, in-, and post-storm data are from September 15, 22, and 26, respectively 39

3.4 Vertical velocity w [Eq. (3.1)] induced by TC Rita over the geostrophic flow of the LC system. Positive (negative) values indicate upwelling (downwelling). Black arrows are wind stress vectors capped at the saturation level [Eq. (3.2)] from the NOAA's H*Wind product. Red arrows are vectors for the oceanic geostrophic flow field, vertically averaged upon the OML. Solid (dashed) red contours are geostrophic flow lines of cyclonic (anticyclonic) circulations. The geostrophic flow field (assumed steady during TC passage) was derived from measurements during the pre-Rita fight (15 September) 42

3.5 OML velocity response u_s at the saturation level. (a) Katrina and (b) Rita. In each panel, u_s is computed from airborne pre-Rita data (15 September) with Eq. (3.3) by applying a spatially homogeneous wind stress at the saturation level (see Table 3.1 and text for more detail). The color shade shows regions with mapping error less than 40% from the objective analysis technique..... 44

3.6 Along-track vertical velocity w [Eq. (3.1)] induced by TC Rita in the LC system (along the storm's best-track, Fig. 3.4). Solid (dashed) line in the w curve indicates underlying cyclonic (anticyclonic) ζ_g. T_{nf} stands for the time required for the 26°C isotherm to reach the sea surface in function of w and h_{26} (see text for details) 47

3.7 Area-integrated energy $PE = 1/2 \int_A \rho_o g h_{iso}^2 dA$, required to reduce SST respect to 30°C in a 1°×2° box by adiabatic lifting of isotherms over a vertical distance h_{iso} (from airborne pre-Rita data, 15 September). For example, a 1°C (4°C) SST reduction means that the 29°C (26°C) isotherm was lifted adiabatically to the sea surface against the gravity acceleration. The rectangular area represents observed SST cooling ranges in the GOM during hurricanes Ivan (2004), and Katrina and Rita (2005). The upper limits of this rectangle are determined by the intersection of the average SST cooling observed during hurricane Ivan (~6.5°C) with the PE curve of the CCE2. The intersection of the PE curves with the dashed line indicates that about 2, 6, and 15×10^{17} J are required to adiabatically reduce SST to 26°C over CCEs, GCW, and LC/WCEs, respectively 48

3.8 Time required, $\Delta T_{nf} = PE\ h_w^{-1}$, to reduce the energy source for Katrina (a) and Rita (b), with $PE = 1/2 \int_A \rho_o g h_{26}^2 dA$, where h_{26} is the 26°C isotherm depth, dA the grid size of the objectively analyzed map, and h_w from Eq. (3.4). In (a) and (b), h_{26} is from pre-Rita (15 September) and post-Rita (26 September)

airborne data, respectively. Contour intervals are: 2 hrs from 0 to 10, and 20 hrs from 20 to 340. See caption of Fig. 3.7 for the meaning of *PE* 50

4.1 Cross-track velocity response at the mooring site (point M, Fig. 2.1). (a) Inside the CCE2 that interacted with Katrina (Fig. 2.8a), and (b) inside the LC bulge affected by Rita (Fig. 2.8b). The vertical lines indicate the time of closest approach of the hurricane's eye to the mooring site (29 August for Katrina; 23 September for Rita)..... 58

4.2 Near-inertial response to Katrina in the CCE2, as observed at the mooring site (87.839°W, 27.998°N). (a) Horizontal velocity response, and (b) square of the vertical shear of horizontal currents $S^2 = (\partial u/\partial z)^2 + (\partial \upsilon/\partial z)^2$. The black curves in each profile in (b) are $4N^2$, with $N^2 = -(g/\rho_o)(\partial \rho/\partial z)$ the square of a reference buoyancy frequency from a density profile acquired inside the CCE2 during the pre-Rita flight. The gradient Richardson number is $Ri = S^2/N^2$. The theoretical limit for shear instability is $Ri < 1/4$ 60

4.3 As in Fig. 4.2, but for the near-inertial response to Rita in the LC bulge. Notice the scale difference of the velocity vectors between 4.2a (50 cm s^{-1}) and 4.3a (25 cm s^{-1})..... 61

4.4 Water mass evolution at the mooring site (point M, Fig. 2.1). (a) Inside the CCE2 that interacted with Katrina (Fig. 2.8a), and (b) inside the LC bulge

affected by Rita (Fig. 2.8b). IP stands for inertial period (25.5 hr), and STW for Subtropical Water. In (a) and (b) the red, green, and blue colors represent pre-, in-, and post-storm (near-inertial) variability, respectively. The black line represents a reference water mass from the WCE core (Jaimes and Shay 2009a) 63

4.5 Vertical mixing induced by (a) Katrina and (b) Rita in the upper ocean, in terms of the mixing parameter ε evaluated from the thermal structure observed during the (a) post Katrina (15 September) and (b) post Rita (26 September) flights. The color shade shows regions with mapping errors less than 40% from the objective analysis technique. Flow lines are for the geostrophic flow derived from the post-storm flights. Black triangles are MMS moorings, and black squares are interpolation points to calculate vorticity from mooring data (Jaimes and Shay 2009b) 65

4.6 Near-inertial wave ray tracing based on Kunze's (1985) model, for (a) Katrina and (b) Rita. The numbers along the wave rays indicate inertial periods (one inertial period is ~25.5 hr), dots are hourly positions, color is the ray's depth level, and the flow lines are from geostrophic flow fields derived from (a) post Katrina (15 September) and (b) post Rita (26 September) airborne-based data. The gray shades represent regions where $(f_e-|S_t|)/f > 0.2$. This ratio, and the flow lines were calculated from depth-averaged velocity fields (Jaimes and Shay 2009b) 69

4.7 Evolution of background relative vorticity ζ_g (normalized by f) at the mooring array during the passage of hurricanes Katrina and Rita (5-IP running means, see text for details). The horizontal axis stands for inertial periods counted from the time of closest approach of the storm to the mooring array. Thin (bold) contours are for cyclonic (anticyclonic) relative vorticity 72

4.8 Time-averaged effective Coriolis parameter $f_e = f + \zeta_g/2$ at the mooring array, inside the CCE that interacted with Katrina (solid) and the LC bulge affected by Rita (dashed). ζ_g was time-averaged from 5 to 8 IP for the CCE, and from 7 to 10 IP for the LC bulge (see text for details). The vertical line represents the local Coriolis frequency f..... 73

4.9 Carrier frequency of the near-inertial response inside (a) the CCE that interacted with Katrina, and (b) the LC bulge affected by Rita, based on least-square fits. Contours are the correlation coefficient r (Eq. 4.7) between observed (mooring data) and modeled (Eq. 4.6) perturbation velocities. Vertical line stands for the local Coriolis frequency (f = 6.85×10^{-5} s^{-1} at 27.998^{o}N) (Jaimes and Shay 2009b)..... 75

4.10 Vertical energy propagation inside the CCE that interacted with Katrina and the LC bulge affected by Rita. (a) Rotary spectra of the near-inertial velocity response inside the CCE (from 5 to 7 IP) and LC bulge (from 8 to 10 IP). The unit nm in this log-log plot stands for normalized meters and is associated

with normalized velocities (Eq. 4.8), while sm is 'stretched' meters (Table 4.2), and c.p.sm is cycles per 'stretched' meter. Solid lines are for the CW component of the spectra, and dashed lines for the ACW component. (b) Ratios between different rotary spectra components (the *x*-axis in this plot is logarithmic): solid line is for the ratio ACW (dominant component) to CW energies inside CCE; dashed line is for the ratio CW (dominant component) to ACW energies inside the LC bulge; and, the thin line contrasts the CW energies from the LC bulge and CCE. The dotted line is a reference representing the ratio equal to one 78

4.11 Amplitude (A_m) of near-inertial currents with the carrier frequency ω_o. A_m and ω_o are normalized by max(A_m) and f, respectively (Jaimes and Shay 2009b) 84

4.12 Vertical variability of the buoyancy frequency N and time-averaged perturbation kinetic energy $\overline{K'}$, inside the CCE and LC bulge. For comparative purpose, the two profiles of N are normalized by max(N) from the LC bulge, and the two profiles of $\overline{K'}$ are normalized by max($\overline{K'}$) from the CCE. For clarity in the presentation, the normalized values of the LC bulge are shifted one unit to the right 86

4.13 Evolution of the kinetic energy of the background flow $\overline{K}$ (bold contours) and the near-inertial perturbations K' (thin contours) inside the CCE, from ADCP mooring velocities. $\overline{K}$ was calculated from 5-IP running means of cross- and

along-track velocity components ($\overline{u}$ and $\overline{\upsilon}$, respectively). K' was calculated from perturbation velocities u' and υ', where $u' = u - \overline{u}$, and $\upsilon' = \upsilon - \overline{\upsilon}$, with u and υ instantaneous WKBJ-scaled velocities (Jaimes and Shay 2009b).. 89

5.1 Dimensions of the computational domain 94

5.2 Model isopycnic layers: 12, 23, and 47, from left to right panels. Upper (lower) panels are for CCEs (WCEs). The circles represent the model density, and the red line is the observed profile (smoothed via polynomial fit). The horizontal lines represent the initial layer thickness outside the QG vortex. The top layer is the OML, and the bottom layer is not shown 95

5.3 Constant wind field used to force the ocean model (from the H*Wind product). External and inner bold contours are for standard 10-m wind speed at tropical storm winds (20 m s^{-1}) and winds at saturation level (27 m s^{-1}), respectively. Vectors are wind stress calculated with a drag coefficient capped at saturation level. The straight line is the storm track. The large and small thin circles are 0.2 m s^{-1} contours of pre-storm OML currents for model WCEs and CCEs, respectively. IP stands for inertial period. Black dots are model moorings on the cross-track direction..... 99

5.4 Initial conditions of the four types of model vortex. Vectors are the initial OML geostrophic currents. The black line is the storm track. L is the initial vortex's radius. Black dots are model moorings on the cross-track direction..... 100

5.5 Evolution of layer thickness anomaly η in the top layer of the ocean model at mooring a (see Fig. 5.3), where η(IP) = h(IP) - h(IP =-1.5), and h is the instantaneous OML thickness. Mooring a was under the storm's eye approximately from IP=-0.25 to IP=0.25. The model initial state corresponds to IP=-1.5 105

5.6 OML thickness anomaly η for WCE1 (left panels) and CCE2 (right panels), where $\eta = h(IP = 3) - h(IP = -1.5)$, and h is the instantaneous OML thickness. In (b) and (e) the storm track is shifted 0.5^{o} to the west, while in (c) and (f) the track shifting is 1^{o}. Circular contours are the initial magnitude of OML geostrophic currents; the contour interval is 0.2 m s^{-1} 106

5.7 OML deepening during the forced stage in WCE1 (a-c) and CCE2 (d-f). (a, d) Pre-storm OML thickness. (b, e) Change of layer thickness due to horizontal current divergence (as in Fig. 5.6). (c, f) OML deepening due to instantaneous turbulent wind erosion (KT model) 111

5.8 OML cooling during the forced stage at moorings a, b, and d, caused by instantaneous wind erosion (KT model), with dT(IP)=T(IP)-T(IP=-1.5)..... 112

5.9 OML cooling *dT* in WCE1 (upper panels) and CCE2 (lower panels), in terms of the KT turbulence closure (a and b), and KT+PWP (c and d). Notice the difference in the temperature scale between upper and lower panels. $dT = T(IP = 3) - T(IP = -1.5)$ 113

5.10 OML velocity response at mooring *b*, in function of vertical entrainment. The label PWP refers to KT+PWP 114

5.11 OML velocity response at mooring *b*, in function of *Ro* (see Table 5.1). KT+PWP is the turbulence closure used in this experiments..... 116

5.12 Near-inertial velocity response in the upper 200 m at mooring *b* (KT+PWP closure)..... 117

5.13 WKBJ-scaled velocity response at mooring *b* (KT+PWP closure). The unit 'sm' stands for stretched meters. Notice that depth is also scaled. These velocity fields are interpolated into a regular vertical grid..... 118

5.14 Frequency of the near-inertial response at mooring *b*, in terms of frequency fits (section 4.3.3) and the PWP turbulence closure. Contour interval is 0.1*f*..... 121

5.15 Vertical wavenumber rotary spectrum. (a, b) Mooring *b*, and (c, d) mooring *d*. Upper panels are CW spectra (downgoing energy), and lower panels are ACW

spectra (upgoing energy). Solid black lines are spectra from observational data acquired during hurricane Katrina (section 4.4.4) 123

5.16 Vertical distribution of time-averaged (from 8 to 11 IP) perturbation kinetic energy $\overline{K'}$ at mooring *b*. (a) CCE1 (*Ro*=0.06), and (b) CCE2 (*Ro*=0.08). Red lines are from direct measurements inside the CCE that interacted with Katrina. *Rc* stands for the critical limit of the gradient Richardson number 125

5.17 Hurricane-induced OML cooling in CCEs in the *f*-plane (upper panels) and β-plane (lower panels). (a, b) CCE1 (*Ro*=0.06), and (c, d) CCE2 (*Ro*=0.08). Circular black contours are the magnitude of OML currents at t = -1.5 IP (initial conditions). Red contours in (d) are the magnitude of OML currents at t = 15 IP for CCE2 in the β-plane, in absence of wind forcing 126

5.18 Vertical distribution of time-averaged near-inertial kinetic energy inside CCE2. (a) from 1 to 5 IP; (b) from 6 to 10 IP; and, (c) from 11 to 15 IP. 23 and 47 are the number of layers..... 128

5.19 OML cooling inside CCE2, as a function of vertical resolution for the KT+PWP turbulence closure; 23 and 47 are the number of layers 128

List of Tables

1.1 Observed characteristics of mesoscale oceanic eddies in the Gulf of Mexico 9

2.1 Summary of profilers deployed in the LC System before (15 September), during (22, 23 September), and after (26 September) the passage of hurricane Rita. The numbers in parentheses indicate profiler failures 19

2.2 Summary of mooring probes that were active in the northern Gulf of Mexico during the passage of TCs Katrina and Rita. T is temperature, C conductivity, and u and υ the horizontal components of the velocity vector 22

3.1 Storm parameters for hurricanes Katrina and Rita. The values of the first baroclinic mode phase speed and Froude number are for the LC bulge (non parenthesis values) and the CCE2 (values in parenthesis). The parameters of hurricane Ivan (2004) are included for comparative purposes 45

4.1 Initial conditions for near-inertial wave ray tracing, with $k_x=2\pi/\lambda_x$, $k_y=2\pi/\lambda_y$, and $k_z=2\pi/\lambda_z$ the zonal, meridional, and vertical wavenumber components, respectively. Positive values of wavelengths λ_x, λ_y, and λ_z are in the eastward, northward, and downward direction, respectively. The values of λ_z were determined from direct ADCP velocity measurements as in Brooks (1983), and $\lambda_x = 4R_{max}$, with R_{max} the radius of maximum winds of Katrina (CCE2)

and Rita (LC bulge). The initial depth of the rays was 40 m. T_i is the inertial period (see text for description of the other parameters) 67

4.2 Comparison of real (zo) and stretched (zs) depth levels at the mooring site. The unit sm stands for 'stretched' meters 77

4.3 Summary of vertical energy fluxes associated with the near-inertial waves induced by Katrina and Rita in the CCE and LC bulge, respectively. These numbers are integrated values of the product $E(m) \times Cg_z(m)$ (Leaman 1976), with $E(m)$ the spectral energy of the m-th wavenumber (from the rotary spectrum, Fig. 4.10a), and $Cg_z(m) \cong -2f\delta m^{-1}$ the vertical group velocity of the m-th wavenumber (Rossby and Sanford 1976), and δ is the departure from the local Coriolis frequency (+0.05 for downgoing energy, and -0.05 for upgoing energy, based on Fig. 4.9). Upgoing (downgoing) energy fluxes were calculated from the ACW (CW) components of the rotary spectrum. Values in parenthesis for the upgoing and downgoing energy fluxes represent the fraction of the total vertical energy flux for the particular geostrophic feature... 80

4.4 Internal near-inertial wave energy flux F_{iw} [Eq. (4.9)] radiated into the thermocline, from mooring ADCP inside the CCE2 (induced by hurricane Katrina), and the LC bulge (induced by hurricane Rita). F_{iw} represents the fraction of eddy kinetic energy not used to entrain colder thermocline water

into the OML (mixed layer energy sink). Cg_z is calculated from Eq. (4.5b) and parameters in Table 4.1..... 81

4.5 Hurricane-induced global internal near-inertial wave power for oceanic conditions similar to CCE2 (non parenthesis values) and LC bulge (values in parenthesis). W_i is the wave power induced by an individual storm over an arbitrary storm's wake of area $A=dxdy$. The values of the vertical energy flux F_{iw} are from Table 4.4. The global wave power W_g is calculated by assuming a global average of 67 storms per year (Emanuel 2001), that each individual storm was present during 20 days, and that the storms had similar characteristics than hurricanes Katrina or Rita. In an eddy-free ocean the global wave power should be somewhere in between the CCE2 and LC values 82

5.1 Characteristics of modeled QG vortex (cf. Table 1.1)..... 100

5.2 List of experiments. The symbol ρ indicates the type of density field used to initialize the ocean model. KT and PWP stand for the Kraus-Turner and Price-Weller-Pinkel turbulence closures for the OML (section 5.4.1), respectively. Beta indicates β-plane. Control experiments are in italic bold, and changed parameters in bold. *Rc* is the critical limit of the gradient Richardson number. *K* is the number of isopycnic layers, and ΔQ_k is the maximum PVA..... 101

5.3 Stratification characteristics inside the QG vortices, with $g' = g(\rho_2 - \rho_1)/\rho_0$. ρ_1 is the initial OML density, and ρ_2 is the density of the contiguous layer below..... 111

List of Abbreviations

ACW	Anticlockwise
ADCP	Acoustic Doppler current profiler
AXBT	Airborne expendable bathythermograph
AXCTD	Airborne expendable conductivity-temperature-depth sensor
AXCP	Airborne expendable current profiler
CCE	Cold core eddy
CW	Clockwise
CTD	Conductivity-temperature-depth sensor
IP	Inertial period
LC	Loop Current
GCW	Gulf Common Water
GOM	Gulf of Mexico
OHC	Oceanic heat content
OML	Oceanic mixed layer
MICOM	Miami Isopycnic Coordinate Ocean Model
MPI	Maximum potential intensity
SAAIW	Sub Antarctic Intermediate Water
SHA	Surface height anomaly
SSH	Sea surface height
SST	Sea surface temperature
STW	Sub Tropical Water

TC	Tropical cyclone
WCE	Warm core eddy

Chapter 1

Introduction

Forecasting intensity and structural changes is currently one of the most important and difficult challenges in tropical cyclone (TC) research. In spite of the availability of highly sophisticated ocean-atmosphere coupled models, the most accurate intensity forecasts remain statistically based (DeMaria et al. 2005; Mainelli et al. 2008). Although the new generation of three-dimensional ocean-atmosphere coupled models is expected to improve intensity forecasting, there are factors affecting hurricane intensity that need to be well understood and represented in coupled models. Among these processes, one of the more important is the evolution of the thermal structure of the oceanic upper boundary layer during interaction with a TC. As the intensification and maintenance of these storms –when the vertical shear of the horizontal wind is negligible– depends exclusively on self-induced heat transfer from the ocean (Emanuel 1986).

TCs are thermally driven circulations whose main energy source is release of latent heat of condensation. This heating establishes the pressure gradients that drive TC winds. The total heat content of normal tropical air raised without entrainment to the level of buoyant equilibrium is insufficient to generate central pressures below 1000 mb that are required to produce and maintain a TC. For central pressure to drop below this value, adiabatic ascent of air parcels must take place at increasing values of equivalent

potential temperature Θ_E (the temperature a parcel of air would reach if all the water vapor in the parcel were to condense, releasing its latent heat, if the parcel is brought adiabatically to a pressure of 1000 mb). This increase of Θ_E can only be obtained through a local absorption of sensible and latent heat from the ocean (Malkus and Riehl 1960). Within the TC boundary layer, air is accelerated inward along spiral-shaped trajectories. Following a particle along these trajectories, the rate and amount of heat absorption from the ocean is governed by wind speed and the difference in temperature and vapor pressure between the two fluids. Based on the first law of thermodynamics, and assuming isothermal expansion, the pressure gradient along the trajectory is limited by the rate of absorption of sensible and latent heat from the ocean. This pressure gradient drives an isothermal and horizontal motion of air parcels. The maximum speed that this air motion (wind) can attain is a function of the heat transfer, and the ratio of depth of inflow layer to the surface friction coefficient (Malkus and Riehl 1960). Two simultaneous thermal constraints thus restrict the dynamics of the TC inflow: (i) the air-sea boundary and the sensible heat transfer; and, (ii) the absorption of latent heat and the ability of the atmosphere to convert the latent to sensible heat by moist adiabatic ascent. Rather than the total amount or rate of condensation, it is the heat content at which the release occurs that affects the central surface pressure (Malkus and Riehl 1960).

The significant role of the sea surface temperature (SST) in the formation and intensification of TCs was recognized in early studies (Palmen 1948; Miller 1958). The premise of a constant SST boundary condition facilitated the development of the air-sea interaction theory for TCs (Emanuel 1986), which provided the framework for the maximum potential intensity (MPI) theory (Emanuel 1988; Holland 1997). Although this

theory was supported by numerical simulations for constant values of SST (Rotunno and Emanuel 1987), early ocean-atmosphere studies emphasized the development of negative feedback on TCs, that results from the storms cooling the upper ocean which eventually shuts down the energy source (Chang and Anthes 1978; Price 1981; Shay et al. 1992). Observational evidence indicates that it is the oceanic mixed layer (OML) temperature response rather than SST, that controls latent and sensible heat fluxes to the atmosphere during the storm passage (Jacob et al. 2000; Jacob and Shay 2003; Shay and Uhlhorn 2008).

Observational and numerical studies conducted in the Gulf of Mexico (GOM) during the last two decades have emphasized the modulation of the OML temperature response to hurricane forcing over mesoscale oceanic features. This modulated temperature response affects the heat and moisture transfer between the two fluids, and impacts the feedback to a TC's intensity. For example, during hurricane Gilbert's passage, the upper ocean cooled by about 4^{o}C in Gulf Common Water (GCW) due principally to vertical shear-induced mixing (Shay et al. 1998; Jacob et al. 2000). More recently, Ivan passage over cold core eddies (CCE) indicated elevated levels of hurricane-induced cooling where SST changes exceeded 5^{o}C (Walker et al. 2005; Halliwell et al. 2008). These two cases of ocean response are clear examples of negative feedback. That is, upper ocean cooling and the deepening of the OML impact the TC's boundary layer, eventually leading to intensity changes (Jacob and Shay 2003; Shay and Uhlhorn 2008). By contrast, in regions of the Loop Current (LC) and warm core eddies (WCE), the ocean only cools by about 1^{o}C during hurricane passage (Shay et al. 2000; Shay and Uhlhorn 2008) and there is less negative feedback than commonly assumed in

forecast models where the ocean's structure is considered to be uniform and at rest. TCs are much more likely to reach a larger fraction of their MPI over warm oceanic features of the GOM and the Caribbean Sea (DeMaria and Kaplan 1994), where subtropical water with 26^{o}C temperatures extend to depths of more than 100 m. These deeper heat reservoirs provide a continuous source of energy for hurricanes to intensify under favorable atmospheric conditions (Hong et al. 2000; Shay et al. 2000). Upper ocean cooling by TCs over WCEs and CCEs, or the lack thereof, is therefore important to TC dynamics and prediction. This contrasting OML temperature response impacts the heat content of ascending air, and the temperature difference between the two fluids, which controls the amount of absorption of sensible and latent heat from the ocean and the deepening of pressure gradients along inflow's radial trajectories of TCs.

The dependence of TC-induced OML cooling on the presence of mesoscale oceanic features is a critical issue for hurricane intensity forecasting in the GOM, as at any time the Gulf has both WCE and CCE features (Vukovich 2007) (Fig. 1.1). The LC WCEs have a vertical scale of $O(10^3)$ m and diameters between 200 and 400 km (Mooers and Maul 1998), and the heat added to the GOM by one of this eddies after separating from the LC is ~7×10^9 J m^{-2} (Elliot 1982). By contrast, the CCEs have a deep signature of ~800 m and diameters from 100 to 150 km (Hamilton 1992; Walker et al. 2003; Zavala-Hidalgo et al. 2003). The sharp horizontal thermal, haline and momentum gradients between these robust mesoscale features and the surrounding GCW occur over scales of $O(10)$ km with markedly different temperature and salinity structures (Nowlin and Hubertz 1972; Shay et al. 1998). These gradient regimes usually induce the strongest air-sea fluxes during hurricane passage, with values of 1.5 to 2 kW m^{-2} (Hong et al. 2000;

Shay and Uhlhorn 2008). This mesoscale variability is often not captured by the satellite-derived near uniform SST distribution that prevails in the GOM during the hurricane season.

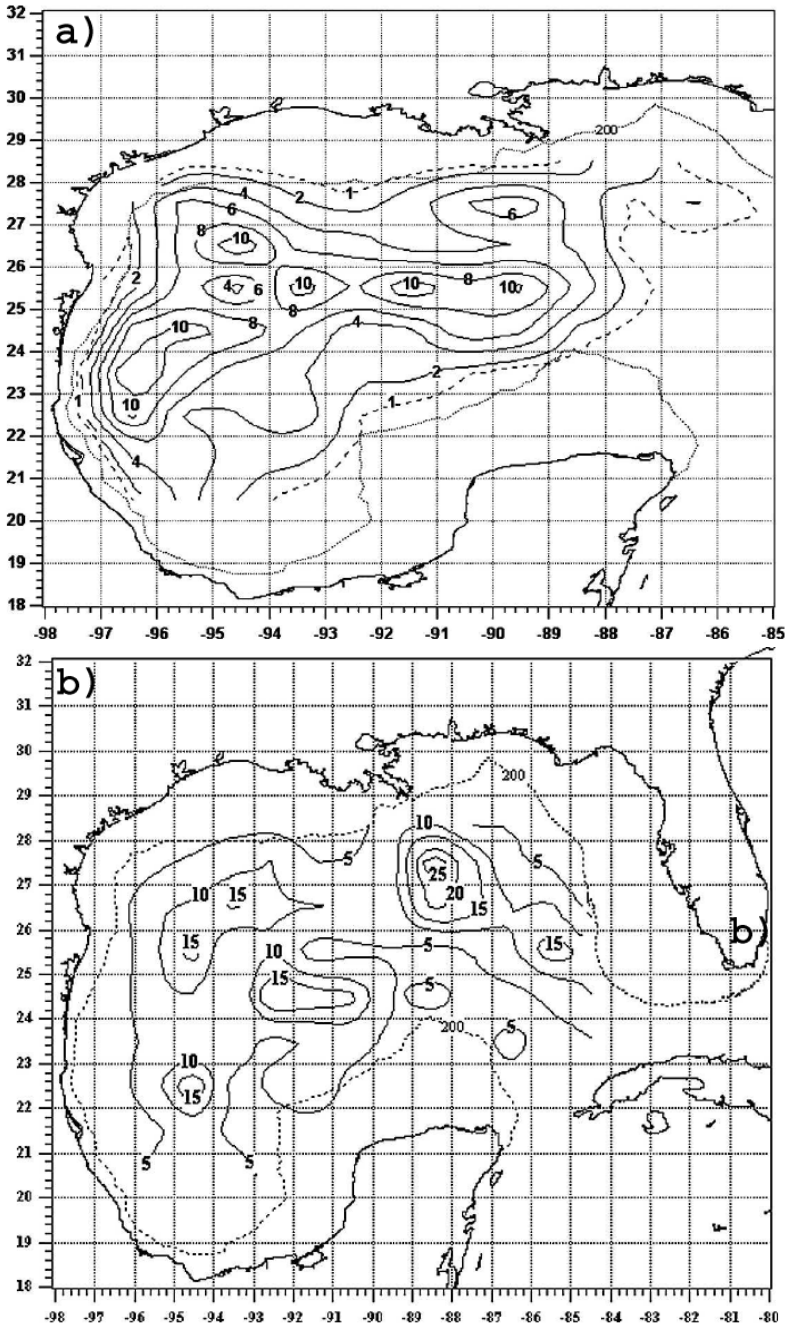

Figure 1.1: Spatial frequency (%) for the location of WCE and CCE centers in the Gulf of Mexico. (a) WCE centers using a 27-year (1977-2003) database. (b) CCE centers using a 12-year (1992-2003) database (Vukovich 2007).

1.1 Motivation

This dissertation is motivated by the non-linear modulation of the OML thermal and velocity response to TCs Katrina and Rita (2005), observed over mesoscale oceanic features in the eastern GOM. These hurricanes propagated in the LC system during the bulging and shedding of a LC WCE, where several frontal CCEs moved along the periphery of the LC and the bulge (Fig. 1.2). Both TCs deepened to category 5 status over the warm LC bulge (where OML cooling was reduced), then subsequently weakened to a category 3 status after encountering one of the frontal CCEs (where significant OML cooling was observed) coupled with unfavorable atmospheric conditions prior to making landfall.

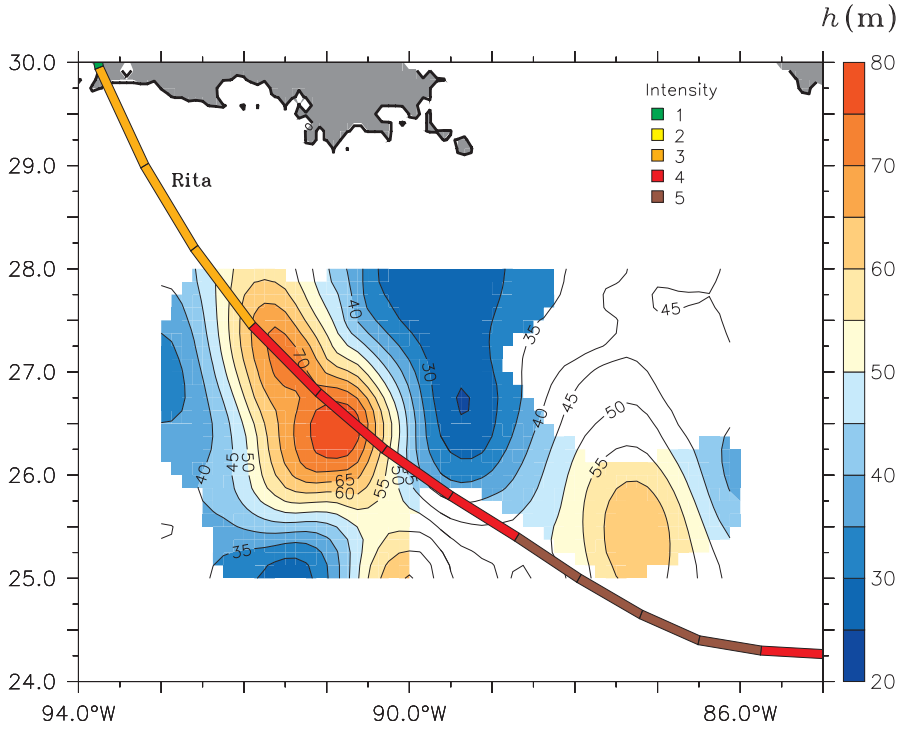

Figure 1.2: OML topography in the eastern Gulf of Mexico on 15 September, 2005, from airborne measurements of the thermal structure. The OML base is defined as the depth of the first occurrence of T_{oml} -$T(z)$ > 0.5°C, where this difference is computed downward from a depth of 2 m at intervals of 2 m. T is temperature, and T_{oml} is vertically-averaged temperature upon the upper 20 m. Red and blue shades represent WCEs and CCEs, respectively.

1.2 Statement of the problem

The TC-induced OML thermal response is principally governed by three processes: (i) sensible and latent heat loss to the TC across the air-sea interface, (ii) upwelling of colder thermocline water due to the horizontal divergence of wind-driven OML currents during the forced stage, and (iii) turbulent entrainment of colder thermocline water due to either instantaneous wind stirring (forced stage) or instability of the vertical shear of forced near-inertial oscillations (relaxation stage). In quiescent ocean regimes, vertical shear-driven entrainment generally accounts for 75 to 90% of the OML cooling (Price 1981; Greatbatch 1984; Shay et al. 1992, 2000; Hong et al. 2000; Jacob et al. 2000). By contrast, air-sea fluxes explain only 5 to 15% of the total OML cooling, while horizontal advective tendencies can be comparable to the heat loss across the air-sea interface (Jacob et al. 2000).

Several processes in mesoscale oceanic eddies can however modulate the efficiency for the storm's wind stress to accelerate horizontal OML currents, affecting the rate of wind-induced upwelling and vertical entrainment for layer cooling. For instance, it has been speculated that the rate of wind-driven upwelling can be affected by the geostrophic flow, as the wind stress acting on a geostrophic vortex tends to tilt its' axis away from the vertical, but the strong geostrophic relative vorticity ζ_g allows the vortex to maintain vertical coherence by developing vertical velocities that balance the wind-induced horizontal advective tendency to first order (Stern 1965).

The density structure and ζ_g associated with the geostrophic features [i.e., shallower (deeper) isopycnals/OML in CCEs (WCEs)] set the amplitude of the OML velocity response (Gill 1984; Zervakis and Levine 1995; Jacob and Shay 2003), and

impose a contrasting spatial distribution of allowable near-inertial wave frequencies excited by storms. That is, the geostrophic relative vorticity ζ_g shifts the lower bound of the internal waveband from the local Coriolis frequency f to an effective Coriolis frequency $f_e = f + \zeta_g / 2$. This broadening or narrowing of the near-inertial wave passband impacts the accumulation of momentum and vertical shear development in the upper ocean (Kunze 1985). Gill (1984) showed that deeper (shallower) OML increases (decreases) the rate of energy loss due to radiation of internal near-inertial waves from the OML into the thermocline. This energy loss can reduce the rate of OML deepening and entrainment across the OML interface up to 50%, as suggested by Linden (1975).

Although the incorporation of WCEs and oceanic background flow in numerical experiments has reproduced more realistic storms during interactions with warm oceanic features (Emanuel 1999; Jacob and Shay 2003; Emanuel et al. 2004), it is unclear what actual oceanic processes reduce OML cooling, and whether these processes are properly represented in OML entrainment parameterizations. It is also unclear if, in contrast, upwelling and vertical entrainment are increased when TCs interact with the cyclonic circulation of CCEs. To assess these effects, this dissertation investigates the thermal and velocity response to TCs in mesoscale oceanic eddies. Thus, the **objective** here is to understand the processes that modulate OML cooling in differing geostrophic regimes.

The **working scientific hypothesis** is that in WCE regimes the OML temperature remains at effective levels (> 26^{o}C) due to deeper isotherms and modulation of both upwelling and vertical entrainment by the anticyclonic circulation, which should allow TCs to reach intensities closer to their theoretical MPI values. By contrast, thinner OMLs and the cyclonic circulation in CCEs regimes should facilitate upwelling and vertical

Table 1.1: Observed characteristics of mesoscale oceanic eddies in the Gulf of Mexico.

Parameter	WCE/LC	CCE
U [m s^{-1}]	1–2	0.5–0.8
L [km]	200–400	100–150
OML [m]	~80	~30
Ro (U/fL)	0.05–0.1	0.05–0.08

entrainment, thus enhancing the onset of the negative feedback stage. Mixed layer conditions in WCEs and CCEs are expected to produce below and above *average* TC-induced OML cooling, respectively, compared with the cooling that can be expected in an eddy-free ocean (GCW). In this context, mesoscale eddies are defined as slowly varying closed circulations nearly in geostrophic balance, with horizontal scales on the order of a few hundreds of kilometers, and vertical scales of O(1 km).

1.2.1 Research issues

Classical aspects of the ocean response to a TC –generally well understood under quiescent ocean conditions– are addressed here in presence of very rapidly rotating mesoscale oceanic eddies (CCEs and WCEs with Rossby number Ro < 0.1, Table 1.1). Research issues are: (i) development of the hurricane-induced upwelling; (ii) amplitude of the OML velocity response during the forced stage; (iii) OML deepening driven by the frictional velocity $w_* = \left(\tau/\rho_0\right)^{1/2}$ during the forced stage (τ is the wind stress or the momentum flux from the air to the water, and ρ_0 is the seawater density); (iv) OML deepening by vertical shear instability during the relaxation stage; and (v) dispersion of forced near-inertial waves that reduces the amount of kinetic energy available for vertical mixing across the OML base (OML energy sink).

Development of the TC-induced upwelling

According to Stern (1965), the classical Ekman theory should be extended in the case of the interaction of the wind stress with a geostrophic vortex, because the work done by the frictional velocity w_* against the gradient of OML geostrophic currents tends to develop an additional vertical velocity that complements Ekman pumping at the OML base. Therefore, under similar wind forcing conditions, a contrasting vertical velocity response can be expected at the OML base depending on whether the pre-storm OML geostrophic currents rotate cyclonically or anticyclonically. The resulting upwelling of cold thermocline water, or the lack thereof, impacts the OML thermal response and feedback to storm intensity. By reducing the OML thickness h, the upwelling facilitates wind erosion driven by w_*. By contrast, reducing the OML thickness increases the buoyancy frequency N (a function of h), which reduces the efficiency for vertical shear-driven mixing. The importance of upwelling for entrainment therefore depends on how much OML shallowing is achieved in WCEs and CCEs. In this context, Stern's (1965) theory is applied here to estimate vertical velocities inside WCEs and CCEs that are compared with observational data and numerical experiments.

OML velocity response

It has been shown that the OML velocity response to a TC is a function of the pre-storm layer thickness, as the momentum input from the wind stress is distributed over the layer (Jacob and Shay 2003). In the Gulf of Mexico, the OML thickness is ~80 m inside WCEs and ~30 m inside CCEs, compared with mean values of ~40 m in surrounding GCW (Fig. 1.2). From the simplest OML models, differing amplitudes of the OML

velocity response are expected inside WCEs compared with CCEs and GCW. This response provides a bound on levels of vertical shears and entrainment mixing across the OML base of these oceanic features.

OML deepening during the forced stage

OML deepening during the forced stage is mainly a function of the third power of the frictional velocity w_*, and the buoyancy frequency N at the layer base (Kraus and Turner 1967; Price et al. 1978). The vertical entrainment velocity is $w_e = 2m_1 w_*^3 /(g'h)$, where $g' = g\Delta\rho / \rho_0$ is reduced gravity, $\Delta\rho$ the density jump at the layer base, and m_1 is a mixing efficiency parameter that depends on the sea state (Huang 1986). The theoretical limit for layer deepening is $h_{max} = 2^{\frac{3}{4}} w_* /(Nf)^{\frac{1}{2}}$ (Pollard et al. 1973). Again, the dependence of w_e on h and $\Delta\rho$ suggests a temperature response as a function of the distribution of cyclonic and anticyclonic geostrophic eddies.

OML deepening during the relaxation stage

TC-forced OML currents become more near-inertial during the second half of the inertial period, when the currents rotate anticyclonically with depth (northern hemisphere) that tends to increase vertical shears (Price 1981, 1983; Shay and Elsberry 1987). Vertical shear instability (bulk Richardson number R_b<1/4) causes turbulent vertical mixing between a bulk OML and thermocline waters (OML cooling/deepening). Critical for developing vertical shear instability is the influence of the wave-supporting medium on the kinematical properties of near-inertial waves. The horizontal kinetic energy of these waves typically scales with N (Leaman 1976), and wave breaking and

turbulent mixing can occur if the waves attain a critical limit (Bretherton and Garrett 1969). In rapidly rotating background flows, the geostrophic relative vorticity ζ_g can also contribute in wave amplification and breaking (Kunze 1985). Therefore, it is of interest to evaluate the relative contribution of N and ζ_g during the potential development of vertical shear instability of near-inertial currents propagating inside WCEs and CCEs, which shift the lower bound of the internal waveband from f to f_e.

Dispersion of near-inertial waves

The frequency shifting, from f to f_e, allows near-inertial waves to disperse vertically. The rate of vertical dispersion impacts the amount of kinetic energy available at the OML base for vertical shear development and entrainment (Linden 1975), and is a function of N and the underlying geostrophic relative vorticity ζ_g. The shorter the time near-inertial waves remain in the OML, the less the amount of kinetic energy available for potential shear-driven cooling. The fraction of TC-forced near-inertial waves that is vertically radiated into the thermocline contributes to the global internal wave power in the world ocean. It has been speculated that this contribution plays a major role in driving the Meridional Overturning Circulation (Emanuel 2001). It is therefore important to evaluate the impact of vertical dispersion of hurricane forced near-inertial waves on the OML cooling in WCEs and CCEs, and to assess the contribution from these waves to the global internal wave power.

Underlying geostrophic flow not only facilitates near-inertial vertical wave dispersion, but also the horizontal flow gradients produce a Doppler effect that impacts the horizontal dispersion of near-inertial waves (Mooers 1975; Kunze 1985). Waves

initially propagating downward from the OML are trapped horizontally in WCEs, which enhances vertical dispersion into the thermocline. By contrast, near-inertial waves are stalled in OMLs of CCEs, and are dispersed radially outward from the eddy center (Lee and Niiler 1998). Thus, the effect of the GOM's geostrophic eddies on the horizontal dispersion of TC-forced near-inertial waves will be evaluated, as this dispersion could have an impact on the amount of kinetic energy available for shear-driven OML cooling.

1.2.2 Goal and objectives

This dissertation addresses two related sub-problems of the current discussion on the ocean's role during TC intensity change: the reduced and enhanced negative feedback in WCEs and CCEs, respectively. By isolating the appropriate characteristics of the ocean component that should be included in coupled ocean-atmosphere models to better reproduce hurricane-induced OML cooling, the overriding goal of this dissertation is to determine the OML cooling dependence on oceanic background processes (pre-storm OML thickness, OML base density jump, stratification underneath the OML, and geostrophic relative vorticity). To accomplish this goal, specific objectives are:

1. To determine the TC-induced OML cooling levels in the Loop Current system from observations during TCs Katrina and Rita (2005). For this purpose, 3-D fields from data acquired in WCEs and CCEs during the passage of both TCs are analyzed. These fields are used to: (i) evaluate the OML thermal and velocity response to hurricane forcing in GOM's WCEs and CCEs; (ii) create initial conditions for numerical models; and (iii) evaluate numerical outputs.

2. To identify the physical processes governing OML cooling in mesoscale oceanic eddies during TC passage. Idealized numerical experiments are conducted to evaluate the relative contribution of stratification and potential vorticity anomalies in the modulation of: (i) the hurricane-induced upwelling, and (ii) entrainment cooling across the OML base.

1.2.3 Value of work

This research provides insight into physical processes that work to keep SST nearly constant during TC passage over warm oceanic features, and those that enhance OML cooling over CCEs. The knowledge generated in this dissertation may have important consequences on TC intensity forecasting, by providing guidance for both the optimal initialization of an oceanic component, and the processes that should be included in entrainment parameterizations used in operational and climate-scale coupled ocean-atmosphere models. The poor initialization of the ocean component in operational coupled numerical models is one of the major factors producing unrealistic storm intensity change forecasts for the Gulf of Mexico and the Caribbean Sea.

1.3 Research approach

Although air-sea fluxes are a critical process for storm development and intensification, the OML deepening and cooling that they induce is ignored here, because the interest is on OML cooling due to upwelling and vertical entrainment. This choice is justified in that OML cooling is primarily a function of mechanical processes internal to the OML and upper thermocline. It is the OML temperature response driven by these

internal processes that controls latent and sensible heat fluxes into the atmosphere during TC passage (Jacob et al. 2000; Jacob and Shay 2003; Shay and Uhlhorn 2008).

Airborne-, mooring-, and altimeter-based data are used here to contrast the levels of the OML thermal and velocity response induced by Katrina and Rita inside cyclonic and anticyclonic geostrophic ocean eddies. Numerical experimentation complements this research, as it provides a broader spectrum of controlled cases of study.

1.3.1 Observational approach

The approach is to diagnose the three dimensional structure of the hurricane energy source available in the LC system for Katrina and Rita, and to understand the role of the LC cycle (Sturges and Leben 2000) in building up the mesoscale spatial variability encountered by the two TCs. The temperature and velocity response induced in the upper layers of the LC bulge (warm anticyclonic feature) and CCE that interacted with the two hurricanes is investigated, where the foci includes: (i) OML deepening, (ii) upwelling during the forced stage, (iii) near-inertial velocity response and vertical mixing, and (iv) radiation of near-inertial internal waves form the OML into the thermocline. Implications of the modulated velocity response and negative feedback for the prediction of OML cooling are also discussed.

1.3.2 Numerical studies

The lack of a comprehensive data set of direct measurements of 3-dimensional upwelling and vertical mixing processes at the OML base during TC passage is addressed with numerical experimentation. However, there are two important issues to address: (i)

the production of spurious diapycnal mixing in numerical models of stratified flows when the models do not control numerical mixing to maintain the adiabatic property of advection (Griffies at al. 2000); and (ii) the inability of the numerical representation of the ocean to capture the full spectrum of natural oceans' variability, as only scales larger than the time step and the grid size of the discrete model can be solved deterministically by the discrete version of the governing equations.

To solve issue (i), which applies to background quasi-geostrophic flow *z*-coordinates used in OML domains, the numerical experimentation is conducted with the Miami Isopycnic Coordinate Ocean Model (MICOM) (Bleck and Chassignet 1994), because this model is explicitly built to maintain the adiabatic property of advection in each isopycnic layer. MICOM mixes isopycnic layers only through the explicit introduction of irreversible processes, thus eliminating spurious numerical diapycnal mixing; a feature not provided by σ-coordinates and geopotential level models (Chassignet et al. 1996; Griffies et al. 2000). This is also true for the non-isopycnic slab OML in MICOM, because entrainment and detrainment are explicitly controlled by the slab mixed layer model. To address issue (ii), several grid resolutions are used to resolve the evolving spatial scales identified from observational data.

To keep the analysis both as simple as possible, and as realistic as possible, idealized quasi-geostrophic vortices (WCEs and CCEs) are generated that reproduce the distinctive characteristics of the GOM mesoscale eddies. A constant wind stress derived from observations of Katrina at maximum intensity (category 5 status) is then applied over the ocean model vortices. More details on the numerical approach, computational domain, and numerical experiments are given in Chapter 5.

1.4 Outline

This dissertation is organized as follows: experiments conducted in the LC system during the passage of TCs Katrina and Rita, and data resources and processing are described in Chapter 2. Based on observational data, the thermal and velocity response to these hurricanes inside the GOM mesoscale features is discussed in Chapters 3 and 4, for the forced and relaxation stages, respectively. A description and discussion of the numerical experiments and results are presented in Chapter 5, where the focus of attention is on the thermal and velocity response inside idealized WCEs and CCEs influenced by an idealized hurricane wind stress. A summary and discussion from a broader perspective are presented in Chapter 6, along with concluding remarks.

Chapter 2

Methodology and Data

Observational data acquired in the Gulf of Mexico during the passage of TCs Katrina and Rita, and the data processing methodology are described. The propagation of these hurricanes over the Gulf's mesoscale ocean features is delineated.

2.1. Observational data

2.1.1 Airborne measurements

The 3-dimensional upper ocean thermal and salinity structure in the LC system was surveyed with Airborne eXpendable BathyThermographs (AXBT), Current Profilers (AXCP), and Conductivity-Temperature-Depth sensors (AXCTD) deployed from four aircraft flights during September 2005, as part of a joint National Oceanographic and Atmospheric Administration (NOAA) and National Science Foundation experiment (Rogers et al. 2006; Shay 2009). Flight patterns were designed to sample the mesoscale features in the LC system: the LC bulge (amplifying WCE), the WCE that separated from the LC a few days before the passage of Rita, and two of the CCEs (CCE1 and CCE2) that moved along the LC periphery during the WCE shedding event (Fig. 2.1).

Table 2.1: Summary of profilers deployed in the LC System before (15 September), during (22, 23 September), and after (26 September) the passage of hurricane Rita. The numbers in parentheses indicate profiler failures.

Flight name	Date	AXBT	AXCTD	AXCP	Total
pre-Rita	15 September	20(1)	30(12)	2(0)	52 (13)
Rita-22	22 September	18(2)	–	–	18 (2)
Rita-23	23 September	12(2)	–	–	12(2)
post-Rita	26 September	56(6)	–	–	56 (6)

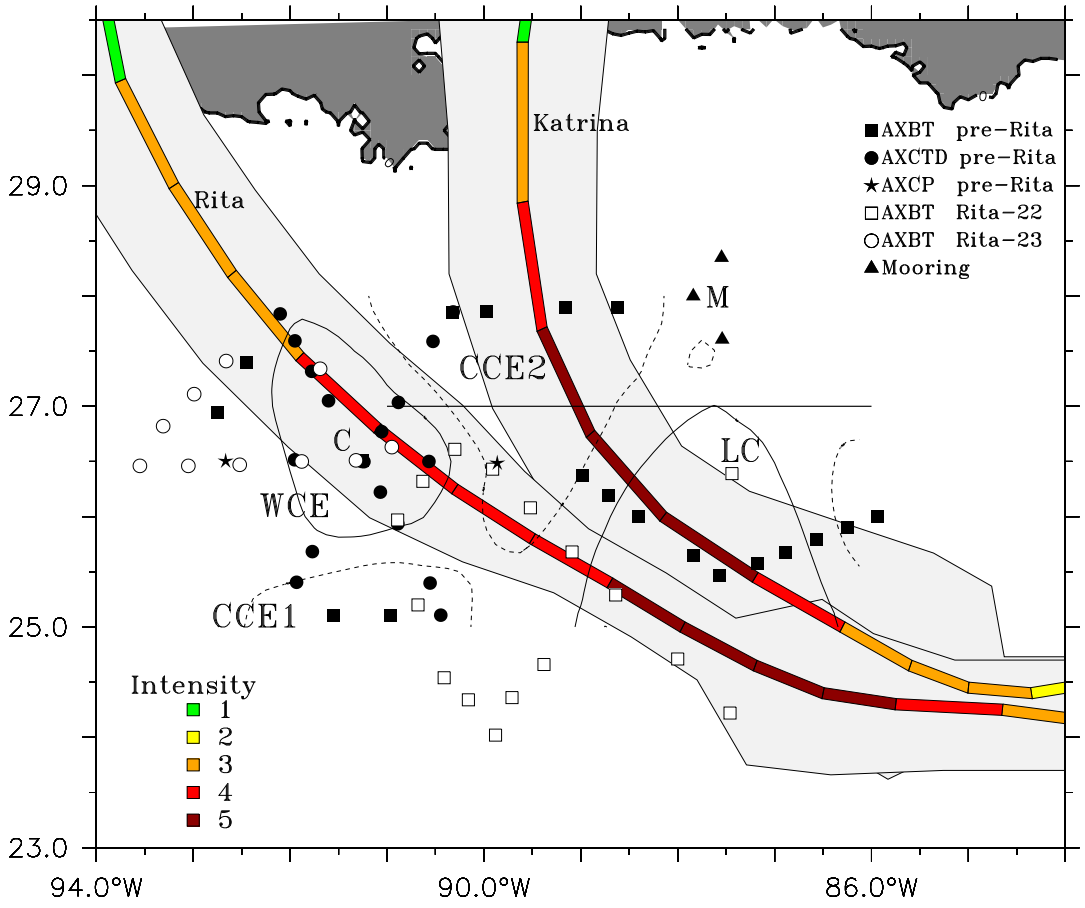

Figure 2.1: Airborne profilers deployed in September 2005 relative to the track and intensity of TCs Katrina and Rita (colored lines, with color indicating intensity as per the legend) over the LC System. The light-gray shades on the sides of the storm tracks represent twice the radius of maximum winds (R_{max}). The contours are envelops of anticyclonic (solid: WCE and LC) and cyclonic (dashed: CCE1 and CCE2) circulations. A set of AXBTs (not shown) was deployed after hurricane Rita (26 September), following a sampling pattern similar to pre-Rita (or post Katrina) (15 September). See Tables 2.1 and 2.2 for a description of collected data and legends. Point M indicates the position of MMS moorings used during this study, and Point C represents the drop site for profiler comparison (AXBT versus AXCTD). The horizontal line along 27°N indicates the extent of vertical sections discussed in the text.

The first aircraft flight was conducted on 15 September (two weeks after Katrina or one week before Rita, i.e. pre-Rita), the second and third flights were conducted during Rita's passage (22 and 23 September, respectively), and the final flight was conducted on 26 September, a few days after Rita's passage (Fig. 2.1 and Table 2.1). Pre-Rita and post-Rita (not shown) flights followed the same pattern, while Rita-22 and Rita-23 focused on high wind regions along Rita's track. Data acquired during pre-Rita flight includes temperature profilers from AXBTs, temperature and salinity profilers from AXCTDs, and current and temperature profilers from two AXCPs deployed in the western and eastern sides of the WCE (Fig. 2.1). During the other three flights, only temperature profiles from AXBTs were acquired to ~350 m depth, compared to 1000 m and 1500 m for AXCTDs and AXCPs, respectively. The accuracy of the thermistor is $\pm 0.12^{o}$C for AXCTDs (Johnson 1995), and $\pm 0.2^{o}$C for AXBTs and AXCPs (Boyd 1987).

To evaluate these temperature profilers from the various sources, one AXBT and one AXCTD were simultaneously deployed in the center of the WCE during pre-Rita; a second AXCTD was deployed at this site on a subsequent leg of the flight pattern. Temperature profilers from these three probes are consistent where RMS differences are comparable to the accuracy of the AXBT thermistor (Fig. 2.2a). The water mass distribution from AXCTDs consists of Subtropical Water (STW) in the upper ocean layers, and Sub Antarctic Intermediate Water (SAAIW) in deeper waters underneath the STW (Fig. 2.2b), in accord with previously reported observations from ship-borne measurements (e.g., Hofmann and Worley 1986).

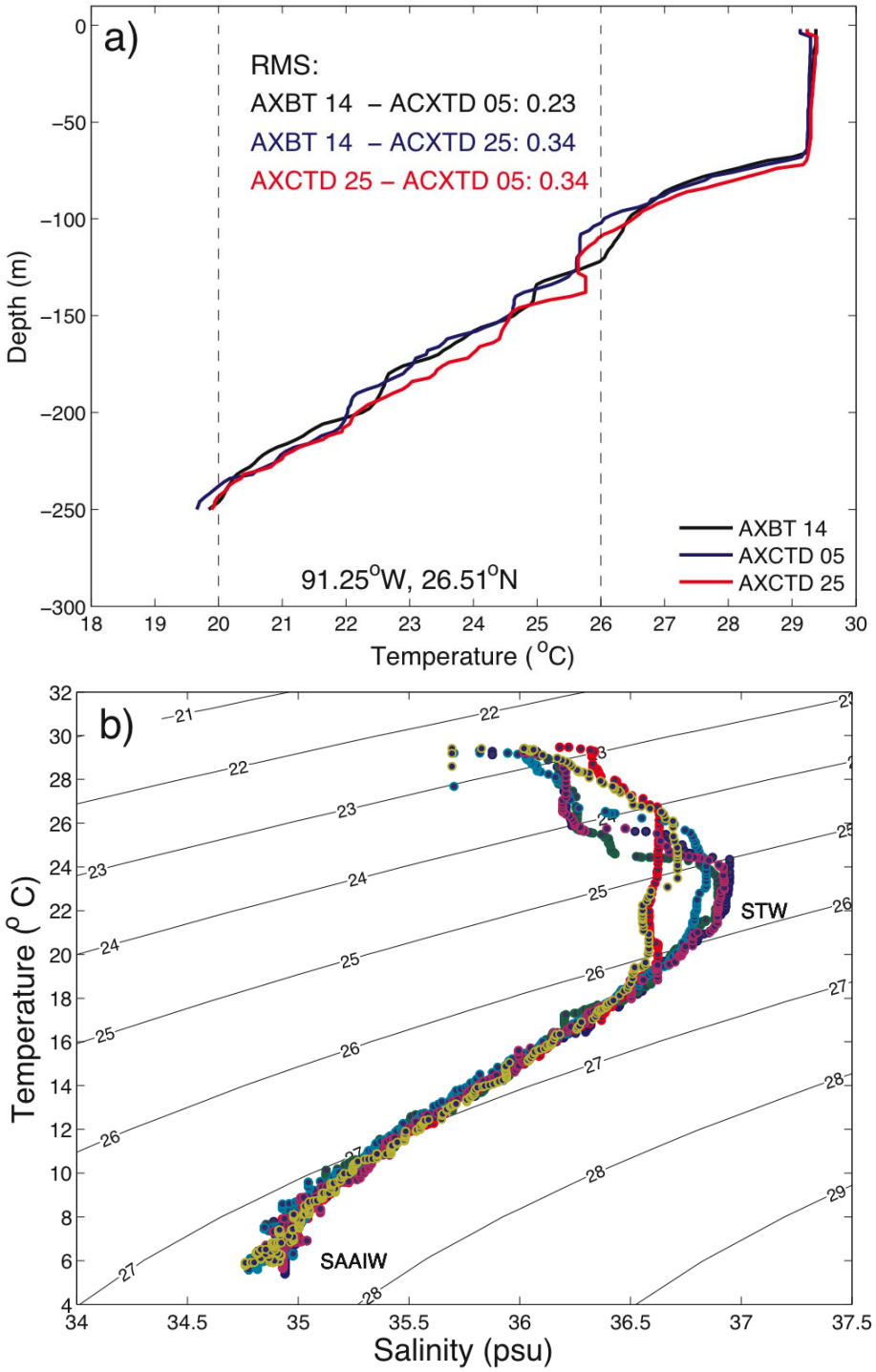

Figure 2.2: Evaluation of airborne profilers performance during the pre-Rita flight (15 September). (a) Comparison of three drops (two AXCTDs and one AXBT) in the center of the WCE (point C, Fig. 2.1). (b) Water mass distribution in the LC System from AXCTDs: Subtropical Water (STW), and Subantarctic Intermediate Water (SAAIW).

Table 2.2: Summary of moorings that were active in the northern Gulf of Mexico during the passage of TCs Katrina and Rita. *T* is temperature, *C* conductivity, and *u* and υ the horizontal components of the velocity vector.

Probe type	Lat (^{o}N)	Lon (^{o}W)	Deployment time	Parameter	Depth range (m)	Vertical sampling interval (m)
ADCP	28.347	87.547	08/2005-01/2006	u, υ	~50-500	~8
ADCP	27.998	87.839	’’	u, υ	~60-500	~8
ADCP	27.606	87.541	’’	u, υ	~30-470	~8
CTD	28.347	87.547	’’	T, C	~75-400	~40
CTD	27.998	87.839	’’	T, C	~75-400	~40
CTD	27.606	87.541	’’	T, C	~60-380	~40

A salient characteristic of the STW (e.g., WCE) is the salinity maximum of ~36.4 to 36.8 psu in σ_t space. This σ_t behavior must be incorporated into numerical models, as a climatological salinity profile is insufficient to accurately initialize the ocean model with a WCE. Realistic salinity profiles to match the temperature profiles would then resolve horizontal density gradients and the corresponding geostrophic flows associated with a warm eddy feature (Nowlin and Hubertz 1972; Shay et al. 1998).

2.1.2 Mooring data

Minerals Management Service (MMS)-sponsored Acoustic Doppler Current Profilers (ADCP) and CTD moorings were deployed in the northeastern Gulf (Fig. 2.1 and Table 2.2). Continuous measurements of oceanic temperature, conductivity, and currents were acquired from the mooring sensors at intervals of 0.5 and 1 hr for CTDs and ADCPs, respectively. Although the moorings were located outside the radius of maximum winds R_{max} of hurricanes Katrina (~4.5 R_{max} where R_{max} = 47 km) and Rita (~17.5 R_{max} where R_{max} = 19 km) (Fig. 2.1), the CCE2 that was affected by Katrina (category 5 status) propagated over the mooring site ≈2 days after interacting with the

storm [convex orientation of low-frequency isotherm fluctuations, Fig. 2.3a, from ~1 to 7 Inertial Periods (IP)]. The anticyclonic circulation of the LC bulge that interacted with Rita (category 5 status) extended over the mooring ≈3 days after having been affected by the storm (concave orientation of low-frequency isotherm fluctuations, Fig. 2.3b from -1 to 5 IP). Altimeter-based evidence of the intrusion of the CCE2 and LC over the mooring is presented in section 2.2.

2.1.3 Wind stress

Wind fields used in this investigation are from the NOAA/Hurricane Research Division H*Wind product, which blends wind measurements from a variety of observational platforms into high-resolution objectively analyzed fields of standard 10-m surface winds (Powell et al. 1996). Based on the H*Wind product, wind stress fields for hurricanes Katrina and Rita were derived using a drag coefficient C_d computed from the Large and Pond (1981) relationship, but capped at a maximum value of 2.6×10^{-3} based on recent results indicating a saturation value of C_d between 27 to 35 m s^{-1} wind speeds (Powell et al. 2003; Donelan et al. 2004; Shay and Jacob 2006; Jarosz et al. 2007).

2.1.4 Geostrophic circulation

As the GOM circulation is dominated by mesoscale features in nearly geostrophic balance with horizontal velocities of approximately 1 m s^{-1} (e.g. Molinari and Morrison 1988; Nowlin and Hubertz 1972), the effects of this energetic geostrophic variability need to be resolved to understand the OML response to TC forcing.

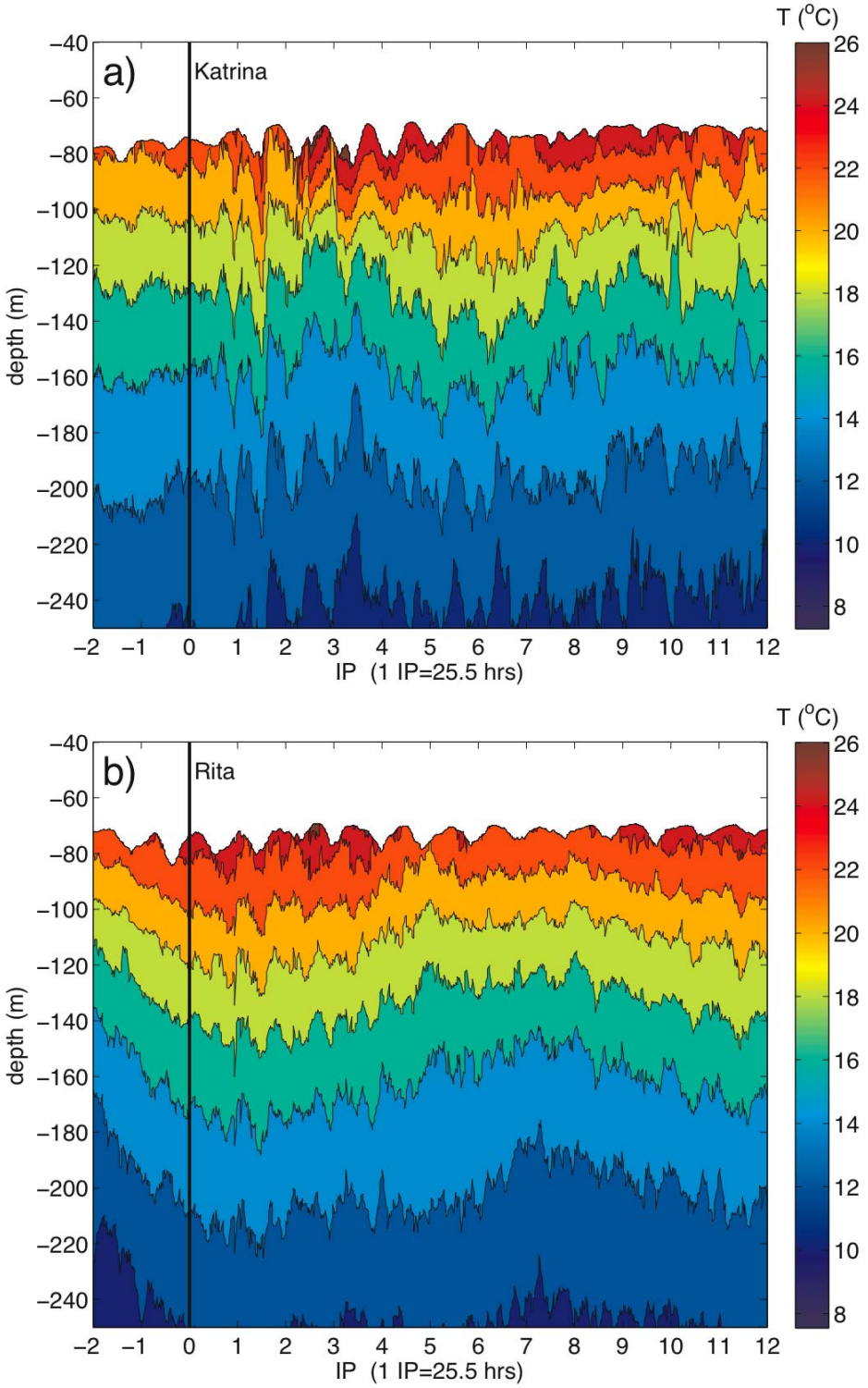

Figure 2.3: Evolution of isotherms at the mooring site (point M, Fig. 2.1) from CTD measurements. (a) Katrina, and (b) Rita. The vertical lines indicate the time of closest approach of the hurricane's eye to the mooring site (29 August for Katrina, and 23 September for Rita). IP stands for inertial period.

Deriving geostrophic flow from the shallow AXBTs (~350 m) measurements is not trivial, as the vertical scale of the mesoscale features is ~800–1000 m. Nevertheless, the water mass homogeneity in the GOM beneath the thermocline (or below the 20^{o}C isotherm depth, Fig. 2.2b), together with the fact that in this region the density is primarily a function of temperature, allows us to extend the shorter AXBT temperature profiles to 1000 m by following the next approach:

1. utilize the reference temperature T_r from the closest (deeper) AXCTD profile to extend the AXBT profile to 1000 m; the original AXBT's upper thermal structure is preserved in the new profile T_t;
2. determine the optimal polynomial fit to the T_r-S_r relationship by using the reference salinity S_r from the closest (deeper) AXCTD together with T_r;
3. utilize polynomial coefficients from above to get the target salinity S_t in terms of T_t;
4. estimate seawater density ρ in function of T=[T_r, T_t] and S=[S_r, S_t];
5. analyze ρ, T, and S via objective technique with the appropriate mapping error (Mariano and Brown 1992); and,
6. estimate geostrophic velocities relative to an assumed level of no motion at 1000 m.

The water mass distribution obtained with this method is shown in Fig 2.4a. The upper ocean variability arises from the original profilers. The inferred geostrophic circulation (Fig. 2.4b) is consistent with observations reported in the literature where the maximum surface velocities are O(1) m s^{-1}. The magnitude of the geostrophic relative vorticity in both WCEs and CCEs is of the same order as the local Coriolis frequency (f =6.39×10^{-5} s^{-1} at 26^{o}N) (Fig. 2.4b), suggesting an important process for modulation of the forced near-inertial response (Kunze 1985, 1986).

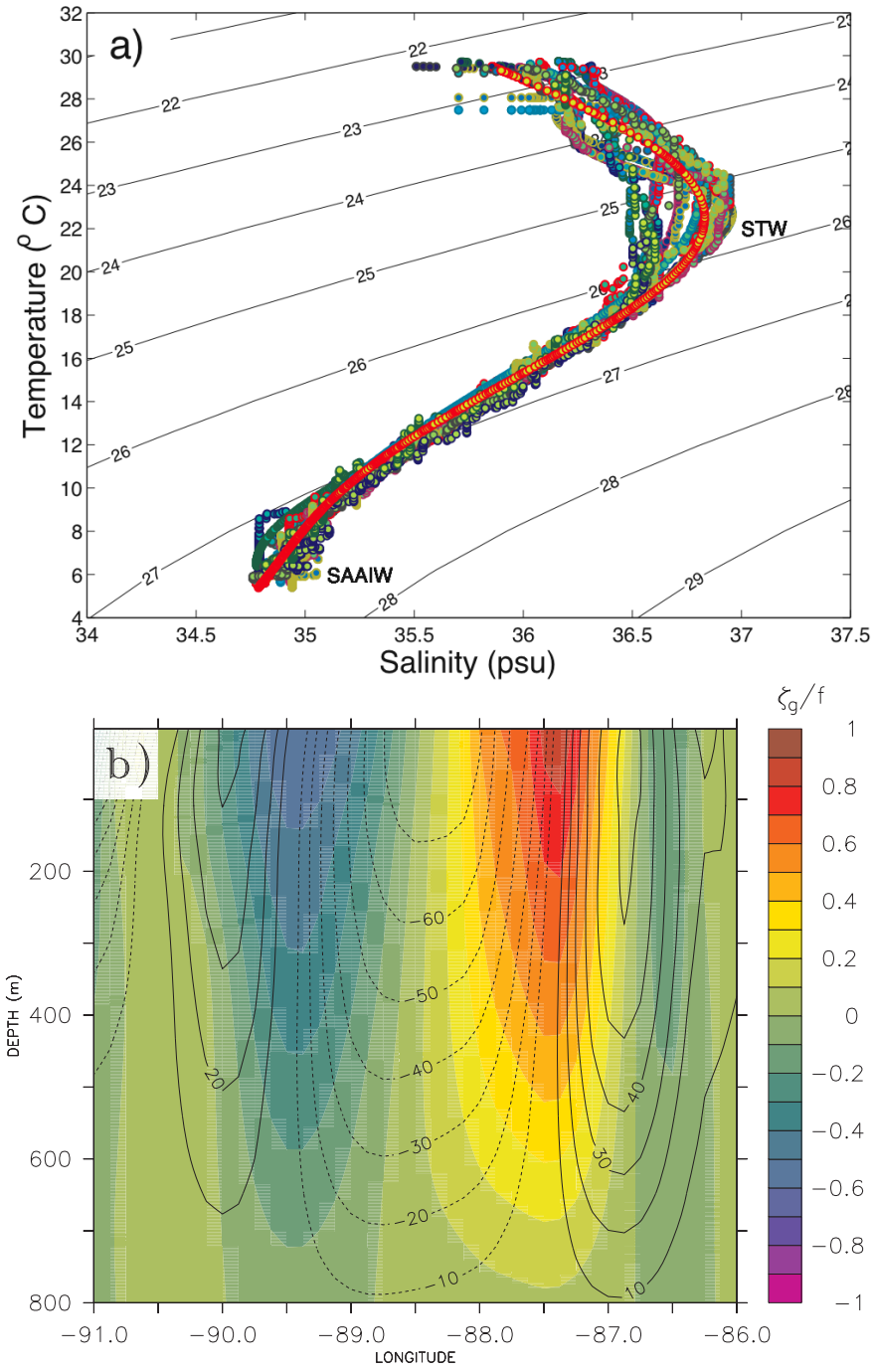

Figure 2.4: (a) Water mass distribution in the LC System on 15 September (between the passage of hurricanes Katrina and Rita), from reference AXCTDs and extended AXBTs and AXCPs (see text for details). (b) Vertical section of the geostrophic circulation of both the WCE and CCE2 at 27°N (horizontal line in Fig. 2.1), derived from the density field in (a); the color scale is for geostrophic relative vorticity ζ_g (positive is cyclonic, and negative is anticyclonic), normalized by the local Coriolis frequency f=6.62×10^{-5} s^{-1}; contours are for the meridional geostrophic velocity, with positive (negative) values indicating northward (southward) velocity.

2.1.5 Isotherm depth and sea surface height from altimetry

In situ data are complemented with altimeter-based 20°C and 26°C isotherm depths (h_{20} and h_{26}, respectively), estimated with a two-layer approach based on the sum of mean and perturbation isotherm depths (Goni et al. 1996; Shay et al. 2000; Mainelli et al. 2008). Mean fields are from a hurricane season climatology of hydrographic measurements (Mainelli 2000), and perturbation fields are estimated from satellite-based radar altimetry measurements of the surface height anomaly (SHA) field from NASA Jason-1, TOPEX, and the NOAA Geosat Follow-on-Mission (GFO). The method to produce daily maps of altimeter-based SHA and isotherm depths is described in detail by Mainelli et al. (2008).

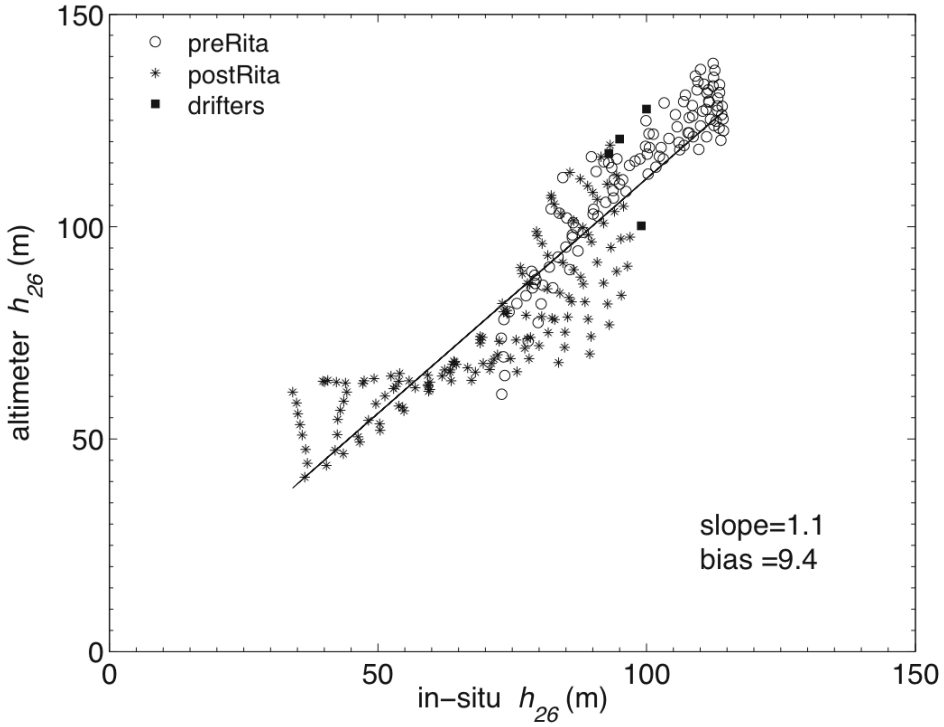

Figure 2.5: Evaluation of the altimeter-based 26°C isotherm depth h_{26}. In situ h_{26} was calculated from airborne temperature profilers and ocean drifters. The ocean drifters are of the type Autonomous Drifting Ocean Station (ADOS), and were deployed on September 21 ahead of Rita in the Gulf of Mexico (Lumpkin and Pazos 2007). Altimeter-based and in situ h_{26} were objectively-analyzed into a 1/8°×1/8° grid for this point-wise comparison.

Altimeter-based isotherm depths capture the observed mesoscale features in the GOM, which agree with those determined from in situ measurements to within ~10% uncertainty, for both h_{26} (Fig. 2.5) and h_{20} (not shown). Moreover, daily maps of absolute sea surface height η were reproduced for the entire GOM by adding the daily SHA fields to the Combined Mean Dynamic Topography Rio05 (Rio and Hernandez 2004). The correlation between four daily snapshots of η and the absolute sea surface height from the 7-day merged AVISO product was between 0.92 to 0.94 for point-wise comparisons over the entire GOM, and for the period from 31 August to 28 September 2005 (Figs. 2.6 and 2.7).

2.2 Hurricanes Katrina and Rita

2.2.1 Hurricane Katrina and mesoscale ocean variability

Tropical storm Katrina emerged over the warm waters of the southeastern GOM at 0500 UTC 26 August, and quickly reached hurricane status at 0600 UTC with maximum sustained winds of 33 m s^{-1}. During this time period, the LC was undergoing a complex shedding event of the WCE (Fig. 2.8a). Weak wind shear dominated the entire GOM basin, and coupled with an efficient upper-level atmospheric outflow facilitated two periods of rapid intensification over the LC between 26 and 28 August (Knabb et al. 2005). Rapid intensification is defined as a 23 to 24 mb or greater pressure decrease in a 24-h period (J. Kaplan 2008, personal communication).

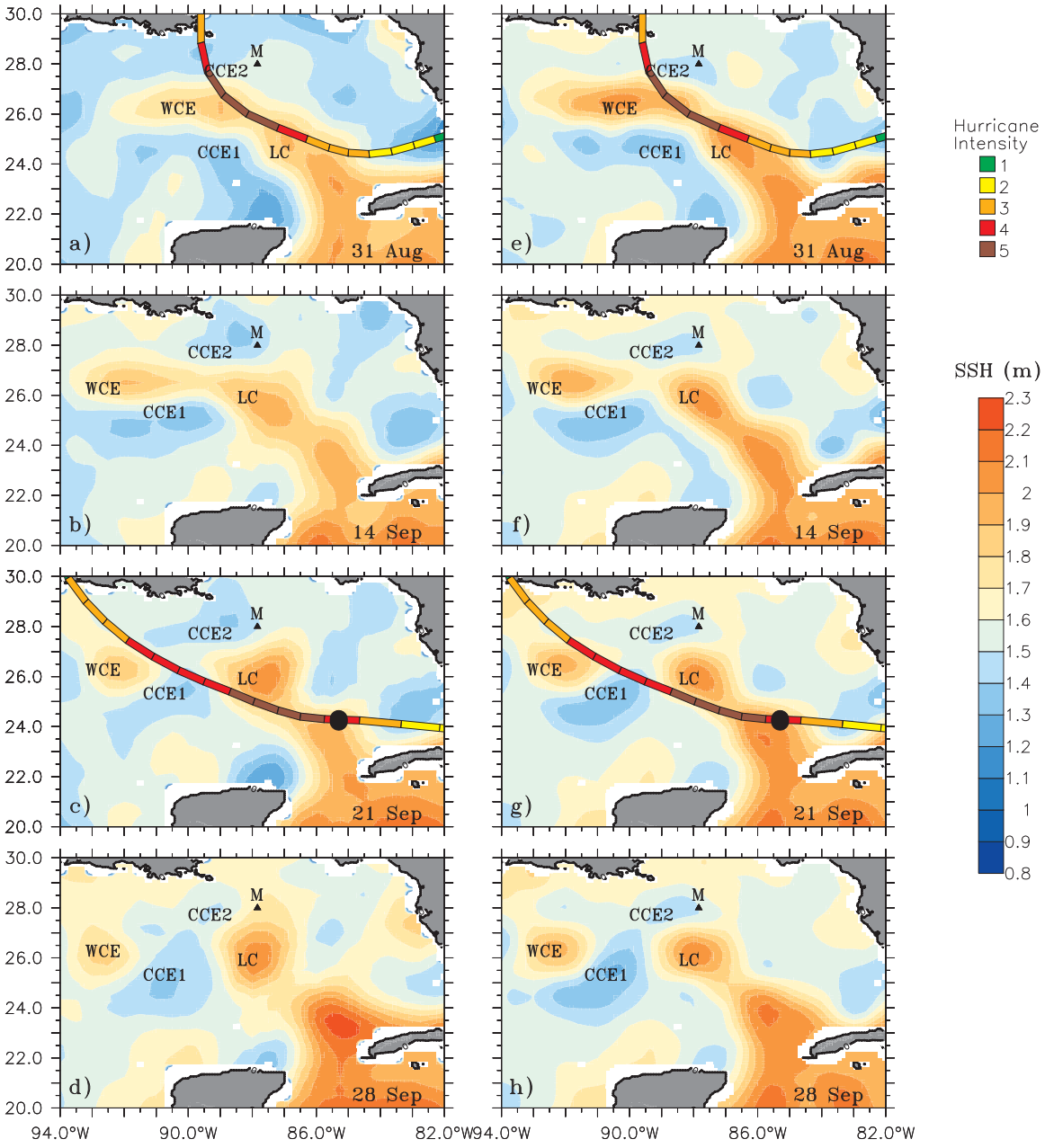

Figure 2.6: Comparison of 1-day η (left panels) and 7-day AVISO (right panels). Color scale is altimeter-based absolute dynamic sea surface height (SSH). (c, g) Black circle is the position of the storm's center. Point M represents the mooring used in this study.

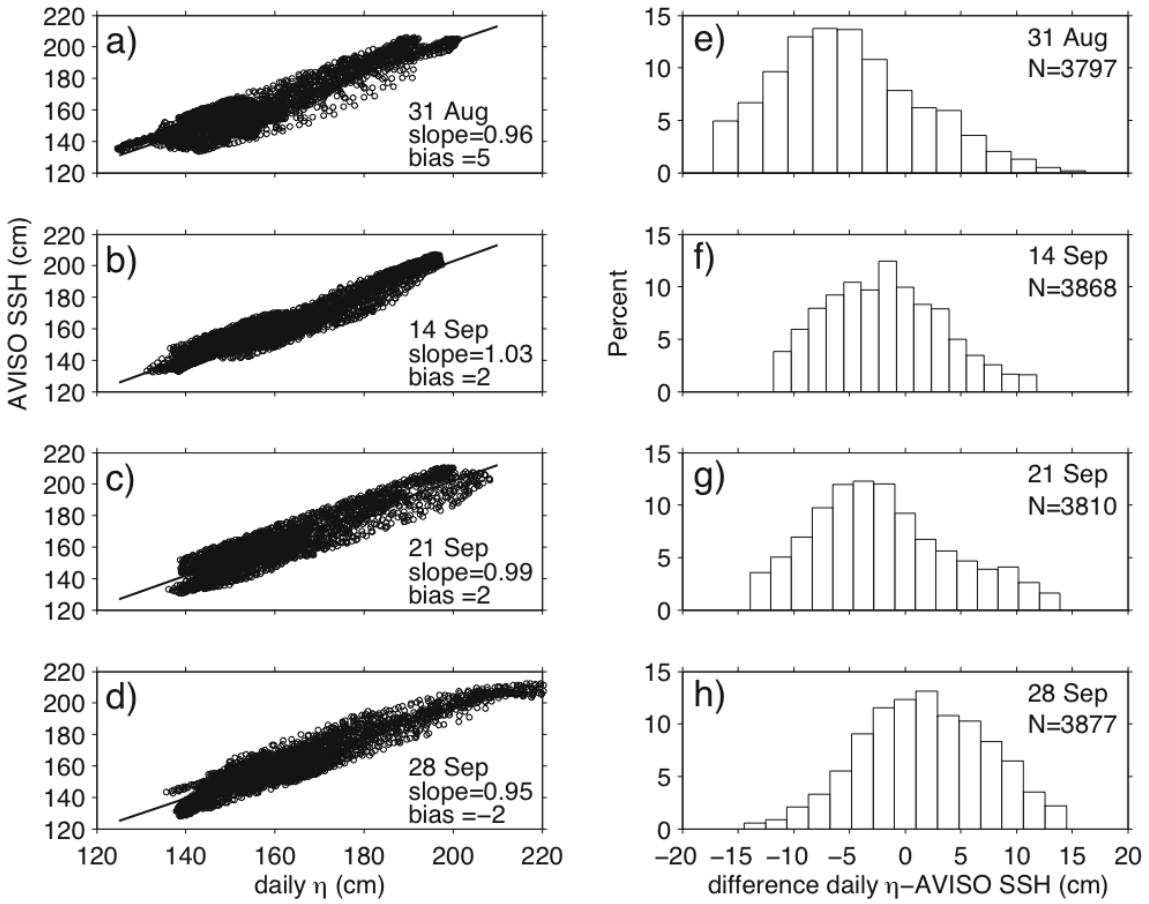

Figure 2.7: Comparison of 1-day η and 7-day AVISO (from Fig. 2.6). The scatter plots in (a)–(d) are from point-wise comparisons between the two SSH products, conducted over a window from 94°W–85°W and from 22°N–29°N. The correlation coefficients were 0.92, 0.94, 0.92, and 0.94 for (a), (b), (c), and (d), respectively. In general, 7 to 9% of the data were not considered in the individual analysis as they exceeded the range of three standard deviations. Histograms of the difference between the two products [(e)–(h)] were calculated based on data from the scatter plots (Jaimes and Shay 2009a).

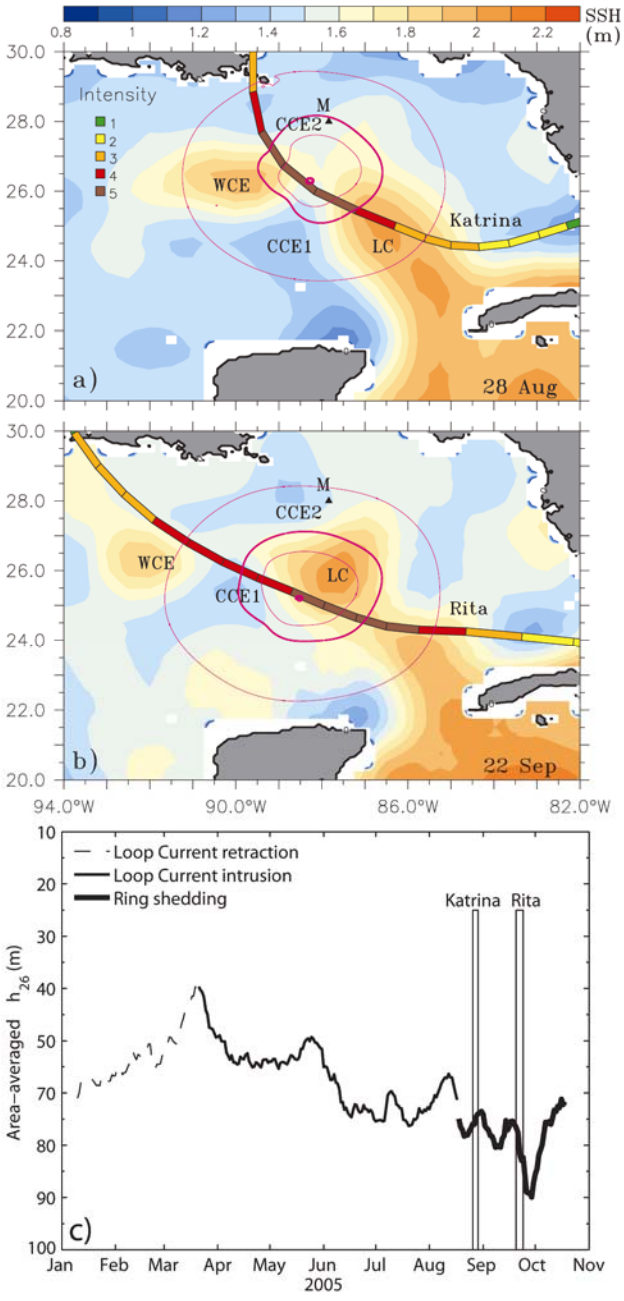

Figure 2.8: Mesoscale ocean variability during Katrina and Rita. Color scale in (a, b) is altimeter-based absolute dynamic SSH from 1-day η, and circular magenta contours stand for standard 10-m wind speed from the NOAA H*Wind product. The external, intermediate, and inner wind circles in (a, b) are the lower limit of tropical storm winds (18 m s^{-1}), winds at saturated level (28 m s^{-1}), and category 1 hurricane winds (33 m s^{-1}), respectively. (c) Loop Current cycle from altimeter-based h_{26} (h_{26} is area-averaged within a box from 93–81°W and 22–28.5°N in the Loop Current region).

The first intensification of Katrina occurred on 1200 UTC 27 August, when the storm increased to category 3 status where surface winds exceeded 51 m s^{-1}. By 1200 UTC 28 August, Katrina had a second and more rapid intensification over the LC bulge during an eyewall cycle as it strengthened from category 3 to category 5 status in less than 12 h. Late on 28 August, Katrina moved over a frontal cold cyclonic feature (growing CCE2) located on the northwestern edge of the LC (Fig. 2.8a). Simultaneously, the hurricane underwent eyewall erosion, while another outer ring of convection developed. Eyewall erosion continued early on 29 August, and the hurricane rapidly weakened making final landfall as a category 3 at 1100 UTC. Structural changes during eyewall erosion appear to have dominated Katrina's rapid weakening before landfall, although colder SST over the CCE, gradually increasing wind shear, entrainment of dry air, and interactions with land could have contributed to this weakening (Knabb et al. 2005).

The amplifying CCE2 that was directly affected by Katrina's wind stress moved over the mooring site by 31 August and it remained over this point for more than 2 weeks (Fig. 2.6a–b, e–f). On 21 September, the WCE was completely detached from the LC as the eddy moved westward (Fig. 2.6c, g).

2.2.2 Hurricane Rita and mesoscale ocean variability

On 20 September 2005, tropical storm Rita approached the Florida Straits with maximum winds of 31 m s^{-1}. As observed during hurricane Katrina, the atmospheric environment had weak vertical wind shear (Knabb et al. 2006). By 1200 UTC 20 September, Rita became a hurricane with an intensity of 36 m s^{-1}, reaching category 3

intensity early on 21 September as it moved westward over the southeastern GOM. Rita's wind reached an intensity of 74 m s^{-1} by 1800 UTC, with a peak intensity of 80 m s^{-1} over the LC bulge on 22 September (Fig. 2.8b). The inner eyewall subsequently collapsed later on 22 September as Rita weakened to category 4 strength. Steady weakening continued on 23 September as the hurricane moved over the frontal CCE1 with increased southwesterly wind shear causing it to weaken to a category 3 status with 57 m s^{-1} maximum winds by 1800 UTC. This intensity level persisted until the time of landfall, which occurred at 0800 UTC 24 September with an estimated intensity of 51 m s^{-1} (Knabb et al. 2006). On 28 September, the LC bulge that previously interacted with Rita (category 5 status) extended over the mooring array (Fig. 2.6d).

Chapter 3

Forced Stage

The thermal and velocity response to hurricanes Katrina and Rita is analyzed in terms of observational data acquired in the eastern Gulf of Mexico. The thermal structure of the Loop Current system is delineated, and the TC-induced oceanic mixed layer cooling levels are diagnosed. A theoretical model is used to estimate the upwelling velocity induced by hurricane Rita over the geostrophically balanced features associated with the Loop Current system. A parametric expression derived from the equations of motion is used to predict the oceanic mixed layer velocity response to Katrina and Rita inside mesoscale oceanic features. The amount of energy required by these tropical cyclones to deplete the energy source is estimated from the density structure in the Loop Current system. An expression to evaluate the time for the depletion of the energy source as a function of the work done by a TC in geostrophic flow is presented.

3.1 Thermal structure in the Loop Current system

3.1.1 Isotherm topography

The LC cycle (Sturges and Leben 2000) is the predominant dynamical process that determines isotherm topography due to advection of warm STW in the eastern GOM through the Yucatan Straits, and by horizontal convergence of mass during WCE

formation. These dynamical processes essentially delineated the thermal structure over which Katrina and Rita moved. As shown in Fig. 2.8c, by March 2005 the LC started to grow as warm STW from the northwest Caribbean Sea was entrained into the current's bulge. The layer thickness with waters warmer than 26^{o}C gradually increased, attaining peak h_{26} values from mid-August through September. During this period, Katrina and Rita moved over the LC where h_{26} supported oceanic heat content (OHC) levels of more than 100 kJ cm^{-2} relative to the 26^{o}C isotherm depth (Mainelli et al. 2008; Shay 2009), as observed during hurricanes Opal (Shay et al. 2000), and Isidore and Lili (Shay and Uhlhorn 2008).

3.1.2 Ocean thermal structure and storm intensity changes

On 28 August, Katrina rapidly deepened to a category 5 status (with an estimated maximum surface wind stress of 7.6 N m^{-2}) as it moved at a speed of ~6 m s^{-1} along the LC's western flank, over a lobe-like structure where peak h_{26} depths were ~110 m (Fig. 3.1a). The corresponding OHC values in this warm feature were ~120 kJ cm^{-2}, or more than five times the threshold of ~17 kJ cm^{-2} d^{-1} needed to sustain a hurricane (Leipper and Volgenau 1972). Prior to landfall, Katrina crossed over the shallower isotherms of a growing CCE where h_{26} depths were ~40 m (CCE2, Fig. 3.1a). The presence of this cooler feature contributed to Katrina's rapid weakening prior to landfall (Knabb et al. 2006).

Three weeks later, Rita translated over the GOM. While Rita's path did not exactly follow Katrina's in the south-central part of the basin, Rita moved over the LC bulge at a speed of ~5 m s^{-1} and rapidly deepened where the maximum wind stress

exceeded 8 N m^{-2}. On 23 September, Rita moved over the eastern tip of the WCE and then began a weakening period due in part to an eyewall-replacement cycle (Knabb et al. 2006) and the previous interaction with the intensifying CCE1 located between the WCE and LC (Fig. 3.1b). Comparison of pre-Rita and post-Rita observations (Fig. 3.1c, d) reveals significant oceanic surface cooling of more than 4°C over this strong frontal regime where Rita interacted with the CCE1.

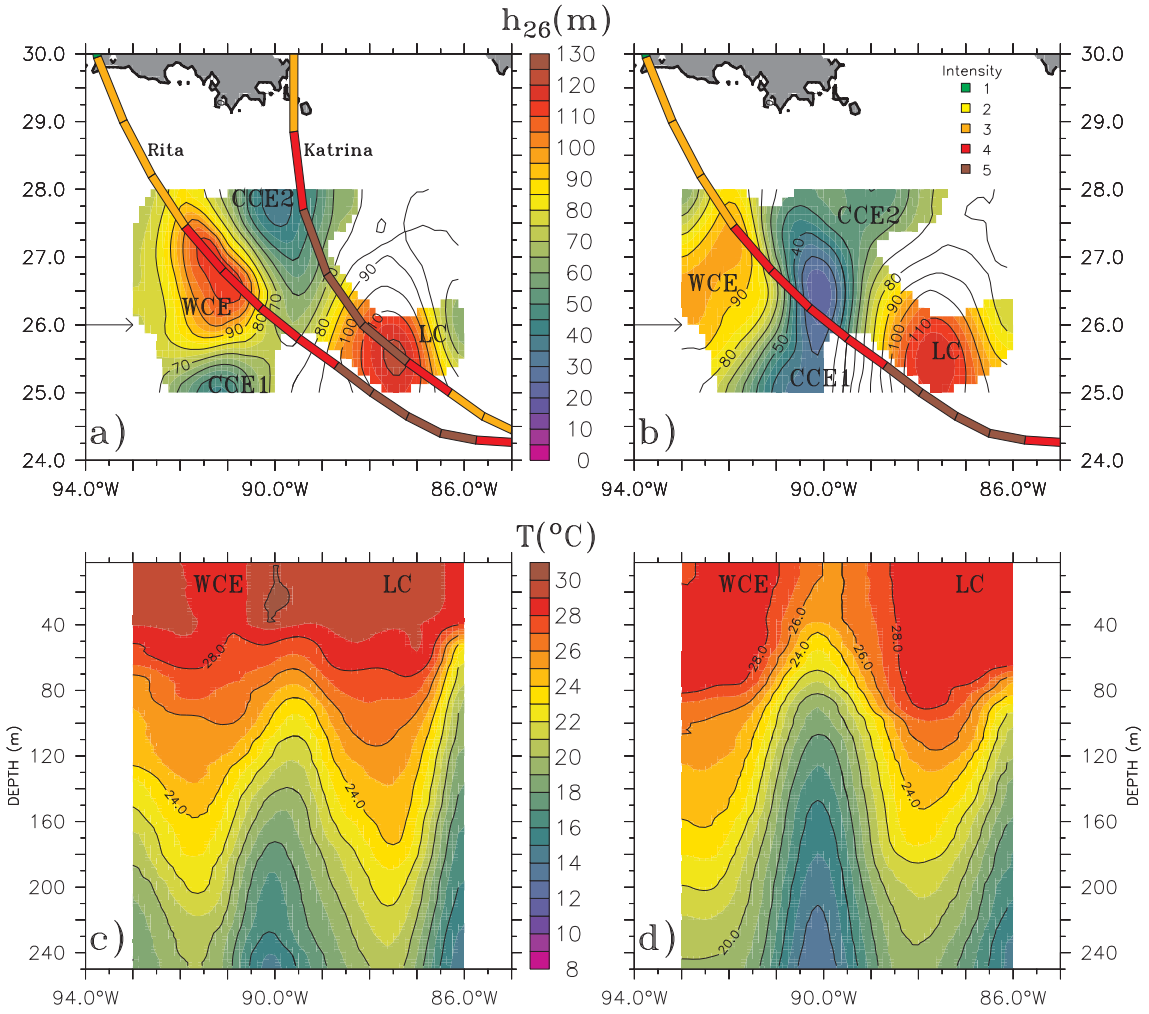

Figure 3.1: Thermal structure in the LC system before (15 September, left panels) and after (26 September, right panels) the passage of hurricane Rita, from airborne profilers. (a) and (b) The h_{26} topography; the color shade shows regions with mapping error less than 40% from the objective analysis technique. (c) and (d) are zonal vertical sections of temperature across 26°N [indicated by arrows in (a) and (b)]. Color in the best-track lines stands for storm intensity as per the legend.

To illustrate this interaction, along-track surface pressure fluctuations are compared to along-track h_{26} and SST variations. The longitude, latitude, and pressure from the National Hurricane Center best-track 6-h files were interpolated to estimate storm position and pressure at 2-hour intervals (Fig. 3.2). Altimeter-based h_{26} fields were used to obtain an averaged value at 2-h storm positions using 9 points from -0.5^o to 0.5^o relative to the best-track position from -2h to 2h. Uncertainty bars represent the standard deviation estimated at each 6-hourly position based on this running 9-point averaging scheme. Generally, normalized h_{26} values vary inversely to pressure changes. That is, as surface pressure decreases, the h_{26} tendency has an upward trend that suggests an impact to TC intensity. The high variability of h_{26} over relatively short distances induced a large OHC gradient, which has been shown to impact the surface enthalpy fluxes due to wind speed variations over thermal gradients (Shay and Uhlhorn 2008). By contrast, along-track SSTs were essentially flat during the life cycle of Katrina and Rita within the GOM (Sun et al. 2006), and did not reveal the mesoscale variability of the LC system. In this case, radar-altimeter derived products were more closely related to intensity variations than SSTs (cf. Scharroo et al. 2005; Shay 2009).

3.2 Oceanic mixed layer cooling

In the case of hurricane Rita, the OML temperature response was differentiated along the storm's track with reduced cooling $\Delta T < 1^oC$ in the region where Rita deepened to category 5 status (LC bulge, Fig. 3.3a), and increased cooling $\Delta T \sim 4$ to 5^oC over the region where Rita started to weaken (shedding front between the WCE and LC, Fig. 3.3b). Similar values of reduced OML cooling over GOM's warm features have been

documented elsewhere (Shay et al. 2000; Shay and Uhlhorn 2008), while increased OML cooling of $O(3 \text{ to } 7)$ ^{o}C was observed during TC Ivan's interactions with CCEs (Walker et al. 2005; Halliwell et al. 2008).

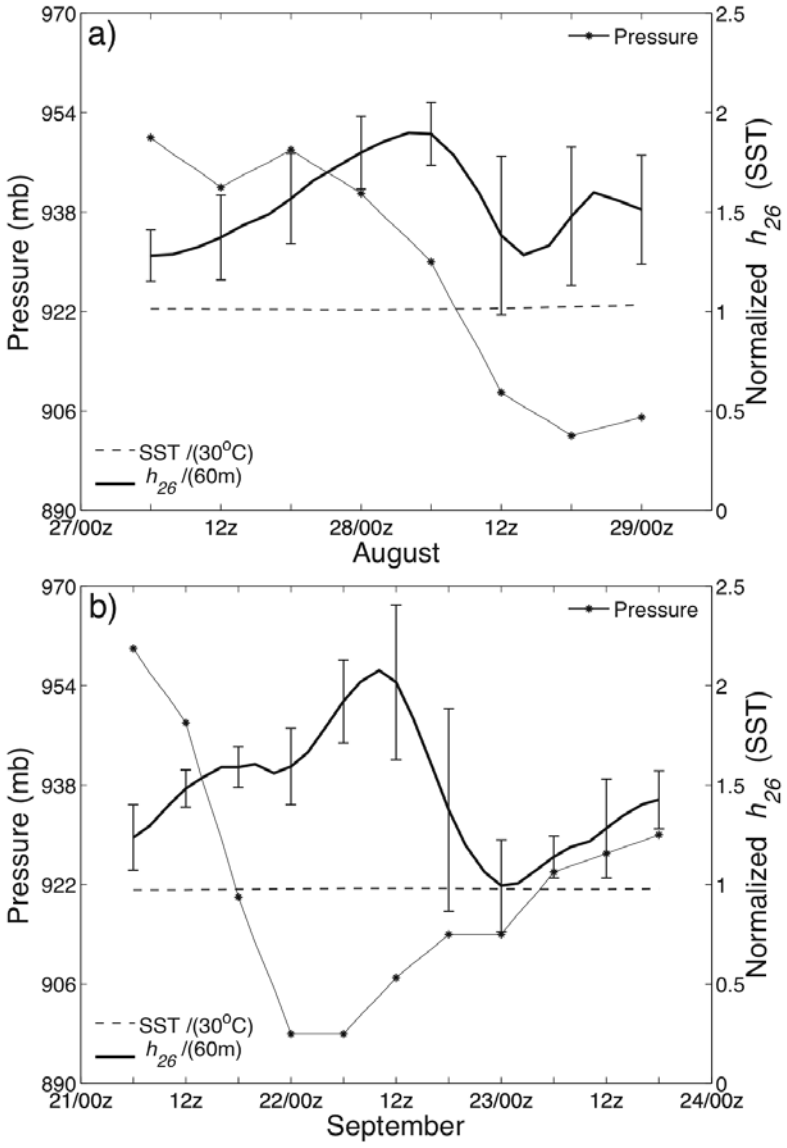

Figure 3.2: Along-track conditions during TCs (a) Katrina and (b) Rita. The time series were constructed with conditions at the actual position of the storm. h_{26} is altimeter-based and normalized by 60 m, while SST is normalized by 30^{o}C. The error bars in h_{26} indicate variability within a half longitudinal degree on each side of the best-track. The maxims in h_{26} in (a) and (b) are associated with the LC bulge, while the minimum h_{26} in (b) is associated with CCE1.

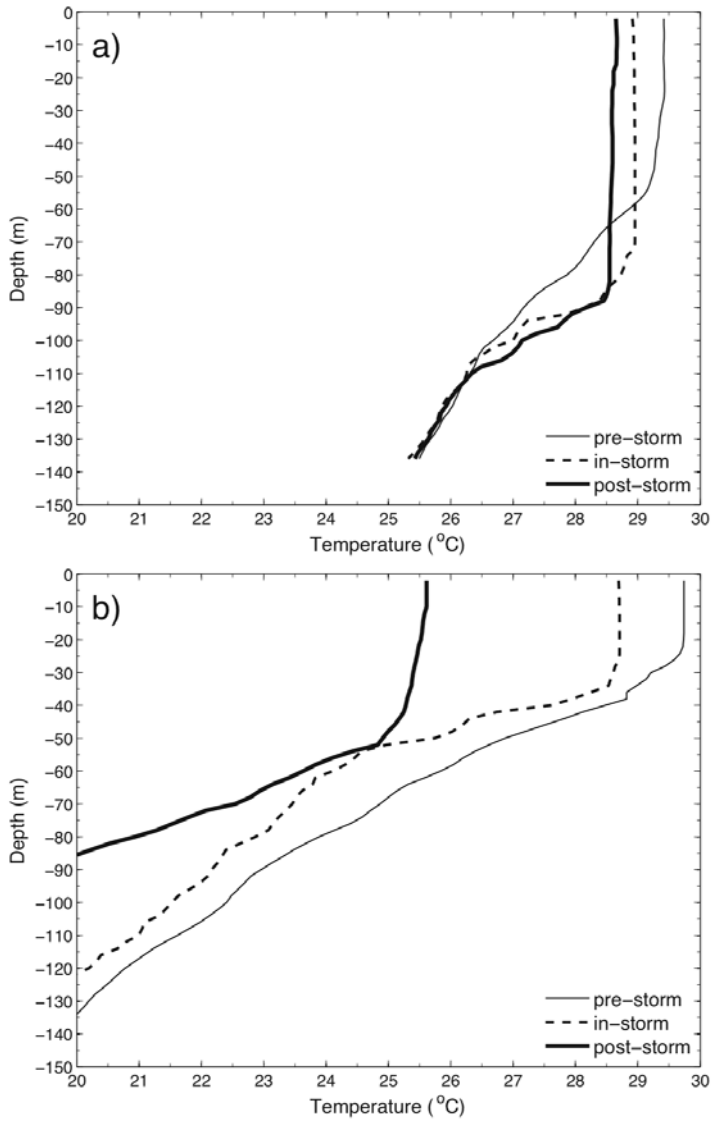

Figure 3.3: Upper-ocean temperature changes induced by hurricane Rita: (a) LC bulge, (b) cyclonic circulation of the growing CCE1 (between the WCE and LC, ~90°W, 26.5°N). Temperature profiles represent cluster-averaged values from airborne data. Pre-, in-, and post-storm data are from September 15, 22, and 26, respectively.

3.3 Upwelling

The comparison of pre- and in-storm temperature profiles for the case of Rita indicates that the storm's wind stress induced downwelling of isotherms over the LC bulge, and upwelling over the region dominated by the CCE1 (Fig. 3.3). To investigate the effects of the underlying geostrophic eddies on this contrasting vertical velocity

response, consider the vorticity balance in the OML resulting from the interaction of the wind stress with a geostrophic vortex, which to the lowest order is given by (Stern 1965):

$$\frac{\partial}{\partial z}\mathbf{k}\cdot\nabla\times\boldsymbol{\theta}_s + f\frac{\partial w_b}{\partial z} = \mathbf{V}_b\cdot\nabla\zeta_g\,,$$

where the first and second terms on the left hand side represent the turbulent stress and vortex stretching, respectively. The term on the right hand side is advection of $\nabla\zeta_g$ by the frictional velocity $\mathbf{V}_b$ (ζ_g is the vertical component of the geostrophic relative vorticity, vertically averaged over the OML). After integrating from $z = -h$ (bottom of the OML) to $z = 0$ (sea surface), this equation becomes

$$\frac{1}{f}\left(\frac{\partial\tau_{sy}}{\partial x} - \frac{\partial\tau_{sx}}{\partial y}\right)_0 + w_b(0) = \frac{1}{f}\int_{-h}^{0}\mathbf{V}_b dz\cdot\nabla\zeta_g\,.$$

In this application of Stern's (1965) theory, $\boldsymbol{\theta}_s(z = 0) \cong \boldsymbol{\tau}_s$ is the wind stress vector. By using the undisturbed Ekman relation $\int_{-h}^{0}\mathbf{V}_b dz = -\frac{1}{\rho_0 f}\mathbf{k}\times\boldsymbol{\tau}_s$, the vorticity balance becomes

$$\frac{1}{f}\left(\frac{\partial\tau_{sy}}{\partial x} - \frac{\partial\tau_{sx}}{\partial y}\right)_0 + w_b(0) = -\frac{\mathbf{k}\times\boldsymbol{\tau}_s}{\rho_0 f^2}\cdot\nabla\zeta_g\,,$$

or,

$$w \cong -w_E - w_b(0) = \frac{\mathbf{k}\times\boldsymbol{\tau}_s}{\rho_0 f^2}\cdot\nabla\zeta_g\,, \tag{3.1}$$

where $w = -w_E - w_b$ is the total vertical velocity, w_E the vertical velocity due to Ekman pumping, and $\boldsymbol{\tau}_s = \tau_{sx}\,\mathbf{i} + \tau_{sy}\,\mathbf{j}$, with

$$\tau_{sx} = \rho_a C_d|\mathbf{U}_{10}|U_{10}, \quad \tau_{sy} = \rho_a C_d|\mathbf{U}_{10}|V_{10}, \tag{3.2}$$

where ρ_a is the air density, U_{10} and V_{10} are the zonal and meridional 10-m wind components, $|\mathbf{U}_{10}| = \left(U_{10}^2 + V_{10}^2\right)^{1/2}$, and C_d is the surface drag coefficient. For a saturation level defined as in Powell et al. (2003), maximum values of $\tau_{sx} = \tau_{sy} \sim 3.8$ Pa were obtained with $C_d = 2.6 \times 10^{-3}$ and $U_{10} = V_{10} = 35$ m s^{-1} from the H*Wind product.

The upwelling velocity w induced by Rita winds over geostrophic eddies is estimated in terms of Eq. (3.1) (Fig. 3.4). The approach is to project time-dependent wind stress fields for this TC over ζ_g from the pre-Rita flight (15 September). Thus, the assumption here is that the geostrophic features were stationary between September 15–23. This assumption is reasonably valid, as the features on which this investigation is focused (LC bulge and CCE2) do not change position significantly during this time period relative to hurricane wind fields (Fig. 2.6). The main point of this calculation is to highlight the sensitivity of the upwelling velocity to the differentiated acceleration of OML geostrophic currents (cyclonic or anticyclonic) by the cyclonic wind stress, which might explain the observed contrasting upwelling regimes discussed here and elsewhere (Halliwell et al. 2008).

Compared to hurricane-induced upwelling over an ocean initially at rest (O'Brien 1967; O'Brien and Reid 1967), in the presence of geostrophic flow the vertical velocity w induced by Rita according with Eq. (3.1) did not show a continuous upwelling maximum underneath the storm's center, since w is a strong function of the projection of the wind stress vector on the geostrophic flow. Upwelling (downwelling) processes can typically be expected when $\boldsymbol{\tau}_s$ is with (against) the geostrophic flow (Fig. 3.4). The wind stress vector orientation along the right side of the storm's track (and within $2R_{max}$) in general coincided with the orientation of the geostrophic flow over the LC frontal zone that

separated cyclonic and anticyclonic circulations (Fig. 3.4b). Over this region, Rita weakened to category 4 status at the same time that upwelling of cooler water persisted with values of ~1 cm s^{-1}, consistent with upwelling velocities of about 1 cm s^{-1} found during hurricanes Gilbert (Shay et al. 1998) and Ivan (Teague et al. 2007).

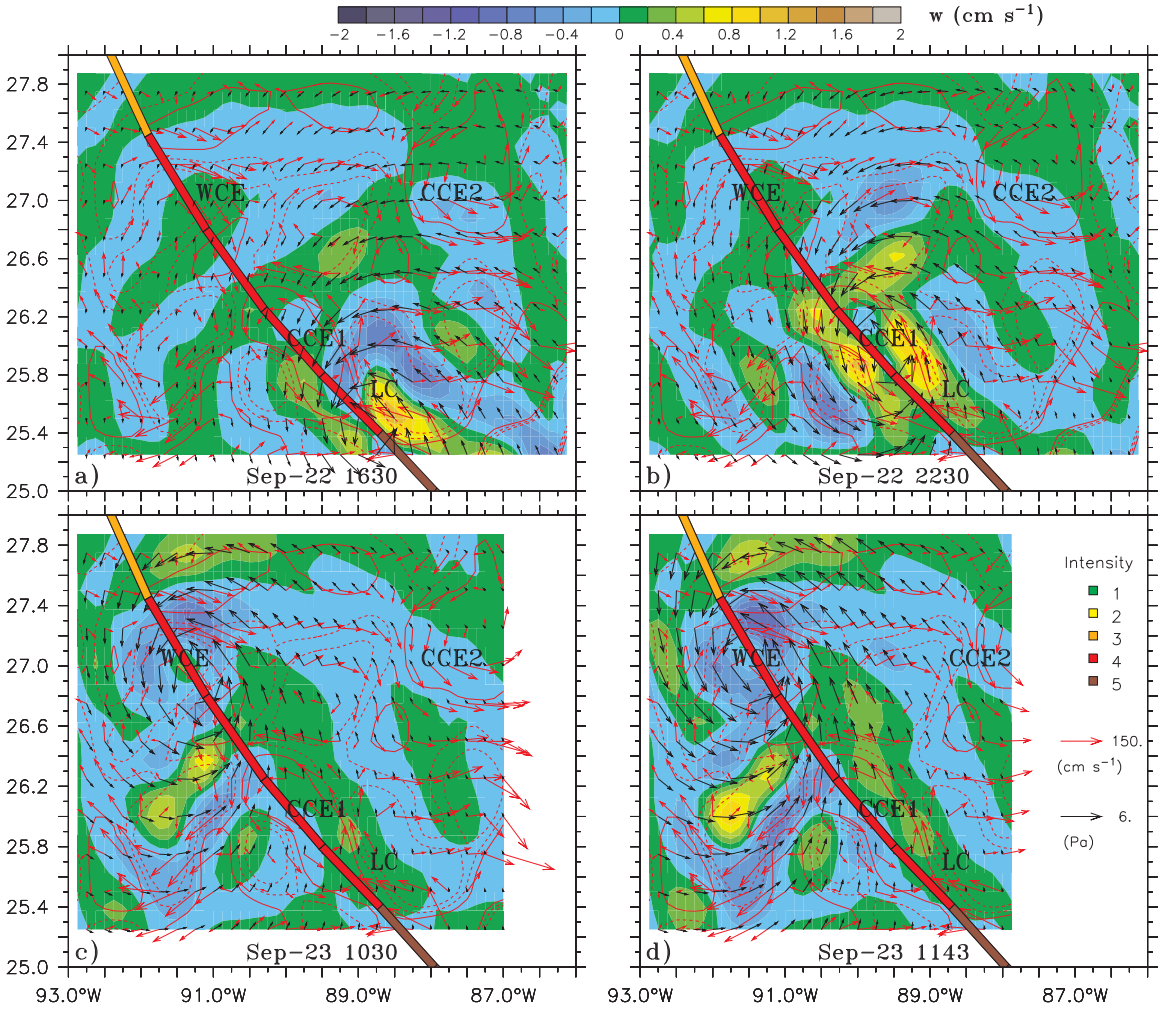

Figure 3.4: Vertical velocity *w* [Eq. (3.1)] induced by TC Rita over the geostrophic flow of the LC system. Positive (negative) values indicate upwelling (downwelling). Black arrows are wind stress vectors capped at the saturation level [Eq. (3.2)] from the NOAA's H*Wind product. Red arrows are vectors for the oceanic geostrophic flow field, vertically averaged upon the OML. Solid (dashed) red contours are geostrophic flow lines of cyclonic (anticyclonic) circulations. The geostrophic flow field (assumed steady during TC passage) was derived from measurements during the pre-Rita fight (15 September).

Observed pre- and in-storm temperature profiles (Fig. 3.3b) support the presence of the upwelling region along the LC front. Wind-driven downwelling velocities of approximately 1 cm s^{-1} were calculated over the WCE that was directly underneath Rita's eye by 23 September (Fig. 3.4c,d) since the wind stress and geostrophic flow were anti-correlated. The comparison of the observed pre- and in-storm temperature profiles seems to support this downwelling over WCEs (Fig. 3.3a), though vertical entrainment also contributes to OML deepening. This issue is addressed in more detail in Chapter 5. Notice that upwelling/downwelling regimes extended over broad regions ahead of the storm's eye, indicating important SST cooling before the arrival of the storm's center (D'Asaro 2003; Jacob and Shay 2003).

3.4 Oceanic mixed layer velocity response

The lack of systematic and comprehensive ocean measurements prevents incorporating the realistic state of the ocean in coupled hurricane models. Hence, an ocean initially at rest and constant OML thickness h are commonly assumed in these models. To evaluate the implications of this practice, consider the OML velocity response u_s that can be expected from a storm with a constant translation speed U_h and wind stress τ_s at the saturation level, which to the lowest order is given by

$$\frac{\partial u_s}{\partial t} \cong U_h \frac{\partial u_s}{\partial x} = \frac{1}{\rho_o} \frac{\partial \tau_s}{\partial z},$$

which can be parameterized as (adapted from Price 1983):

$$u_s(x,y) = \frac{R_{\max} \tau_s}{\rho_o h(x,y) U_h}, \tag{3.3}$$

where $\tau_s=|\boldsymbol{\tau}_s|$ is the magnitude of the wind stress vector as per Eq. (3.2). Notice that Eq. (3.3) indicates that for homogeneous U_h and τ_s the OML velocity response is only a function of the pre-storm mixed layer thickness $h(x,y)$, as less (more) work is required to accelerate a shallow (deep) OML current.

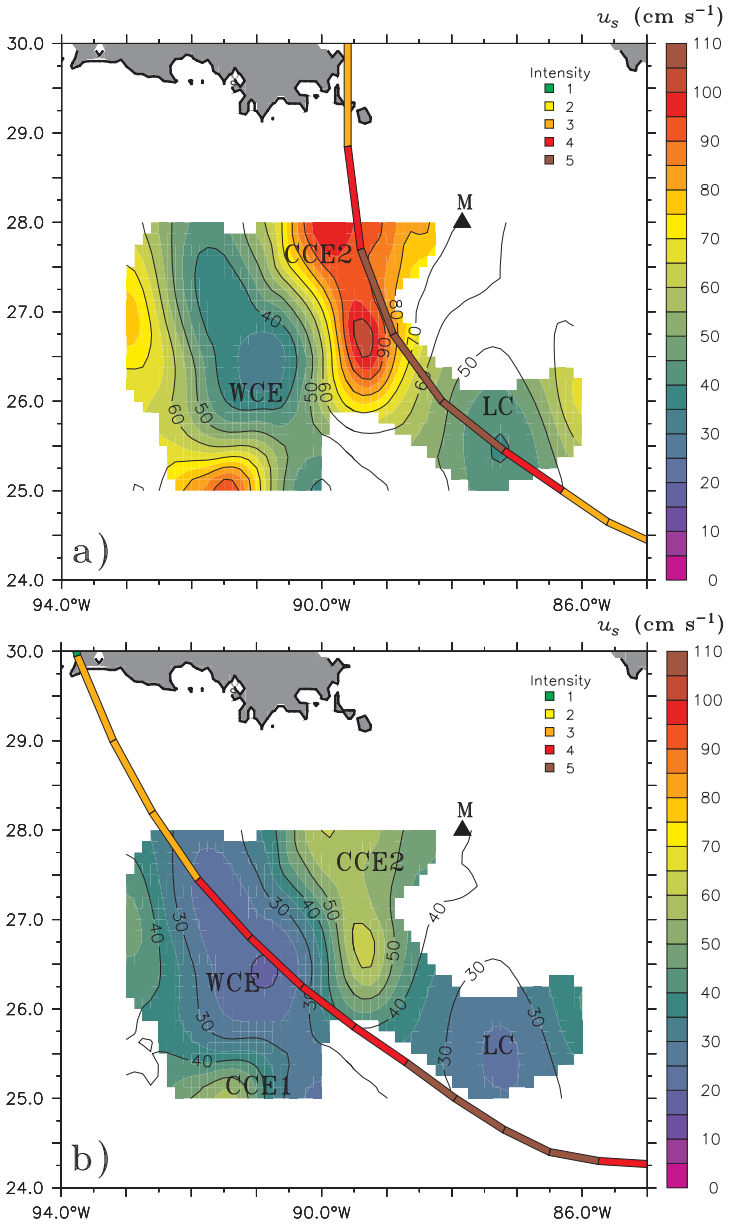

Figure 3.5: OML velocity response u_s at the saturation level. (a) Katrina and (b) Rita. In each panel, u_s is computed from airborne pre-Rita data (15 September) with Eq. (3.3) by applying a spatially homogeneous wind stress at the saturation level (see Table 3.1 and text for more detail). The color shade shows regions with mapping error less than 40% from the objective analysis technique.

Table 3.1: Storm parameters for hurricanes Katrina and Rita. The values of the first baroclinic mode phase speed and Froude number are for the LC bulge (non parenthesis values) and the CCE2 (values in parenthesis). The parameters of hurricane Ivan (2004) are included for comparative purposes.

	Parameter	Ivan	Katrina	Rita
Radius of maximum winds	R_{max} [km]	32	42	19
Speed of the hurricane	U_h [m s^{-1}]	5.5	6.3	4.7
1st baroclinic mode phase speed	c_1 [m s^{-1}]	–	2.9 (2.1)	2.9 (2.1)
Froude number	Fr = U_h (c_1)$^{-1}$	–	2.2 (3)	1.6 (2.2)

For example, by considering the values of R_{max} and U_h (Table 3.1), and *h(x,y)* from the pre-Rita data (15 September), the parametric OML velocity response is about two times larger over the shallower mixed layer of CCEs than over WCEs for similar wind conditions (Fig. 3.5). The parametric velocity response u_s inside the CCE2 (Katrina) and LC bulge (Rita) is comparable to that observed in upper layers at the mooring site (i.e., ~80 cm s^{-1} and ~40 cm s^{-1}, respectively, Chapter 4). This result indicates that, to the lowest order, the amplitude of the OML velocity response is primarily a function of the pre-storm layer thickness (cf. Zervakis and Levine 1995; Jacob and Shay 2003). An OML velocity response of ~35 to 40 cm s^{-1} was observed in deep OMLs of LC warm features during hurricanes Isidore and Lili in 2002 (Shay and Uhlhorn 2008).

3.5 Depletion of the energy source

The spatial variability of both h_{26} and the hurricane-induced upwelling velocity in presence of geostrophic flow add an important thermodynamic constraint on hurricane intensity, as more (less) work is required over WCEs (CCEs) to deplete the energy source and decrease the surface heat and moisture fluxes. The interest on the 26^{o}C isotherm is because observations, theoretical developments, and numerical experiments, indicate that

TC development and maintenance rarely take place when SST is below this value. In the context of the air-sea interaction theory for TCs (Emanuel 1986), the observed absence of TC formation and development when SST is less than 26^{o}C is due to the absence of extensive deep conditional instability or neutrality over those parts of the ocean with SST less than this critical value. Thus, the 26^{o}C value is an empirical and theoretical critical limit to maintain the thermodynamic efficiency (proportional to the temperature difference between the sea surface and lower stratosphere) for TC development (Emanuel 1988).

In the case of hurricane Rita, the storm experienced a rapid weakening over a 6-hr period (from 00 to 06 UTC 23 September) after passing over the LC frontal zone where upwelling velocities ranged from 1 to 2 cm s^{-1}. Direct measurements of the thermal structure acquired during the pre-Rita flight, indicate that h_{26} and the OML base extended nearly at the same depth over this frontal regime. Although the upwelling velocity asymptotically approaches zero at the sea surface, bulk vertical velocities from about 1 to 2 cm s^{-1} along the storm track (from Eq. 3.1) are assumed to estimate the time for h_{26} to reach the sea surface (ignoring air-sea heat fluxes). This is equivalent to assume that all the work done by the wind-driven OML frictional velocity will be used to create a bulk vertical velocity that raises h_{26} from the OML base to the sea surface against the gravitational acceleration (see below). Under these assumptions, the estimated time T_{nf} for the surfacing of h_{26} over this region was ~2 to 3 hr (Fig. 3.6). At a constant translation speed of 4.7 m s^{-1}, Rita traveled a distance smaller than 2.5 R_{max} over a 3-hr interval, indicating that h_{26} may have reached the sea surface before the storm left the maximum upwelling regime. This suggests that the rapid surfacing of waters colder than 26^{o}C shut

down the energy source and reduced the thermodynamic efficiency of Rita along the LC frontal zone. Notice that the above bulk estimate represents the upper bound of the time required to reduce the energy source along Rita's track, based on the work done by the hurricane in the upper ocean and the position of isotherms in the gravitational field. In addition to the asymptotic decay of the vertical velocity in the OML, other processes discussed below should affect this adiabatic estimate.

In this context, the energy required to adiabatically reduce SST to a level in which the TC's energy source vanishes over CCEs, GCW, and WCEs, is respectively 2, 6, and 15 $\times 10^{17}$ J (Fig. 3.7). Notice that the assumption is that a minimum SST of 26^{o}C is required to maintain a TC (Palmen 1948). The energy source is significantly reduced when SST (proxy of the OML temperature under strong winds) falls below this limit.

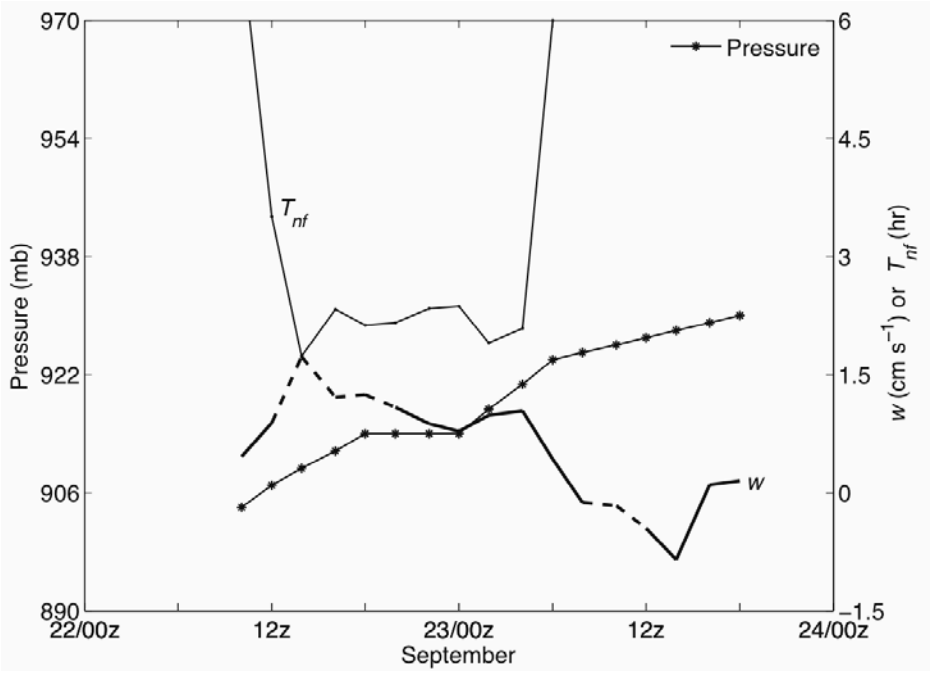

Figure 3.6: Along-track vertical velocity w [Eq. (3.1)] induced by TC Rita in the LC system (along the storm's best-track, Fig. 3.4). Solid (dashed) line in the w curve indicates underlying cyclonic (anticyclonic) ζ_g. T_{nf} stands for the time required for the 26^{o}C isotherm to reach the sea surface in function of w and h_{26} (see text for details).

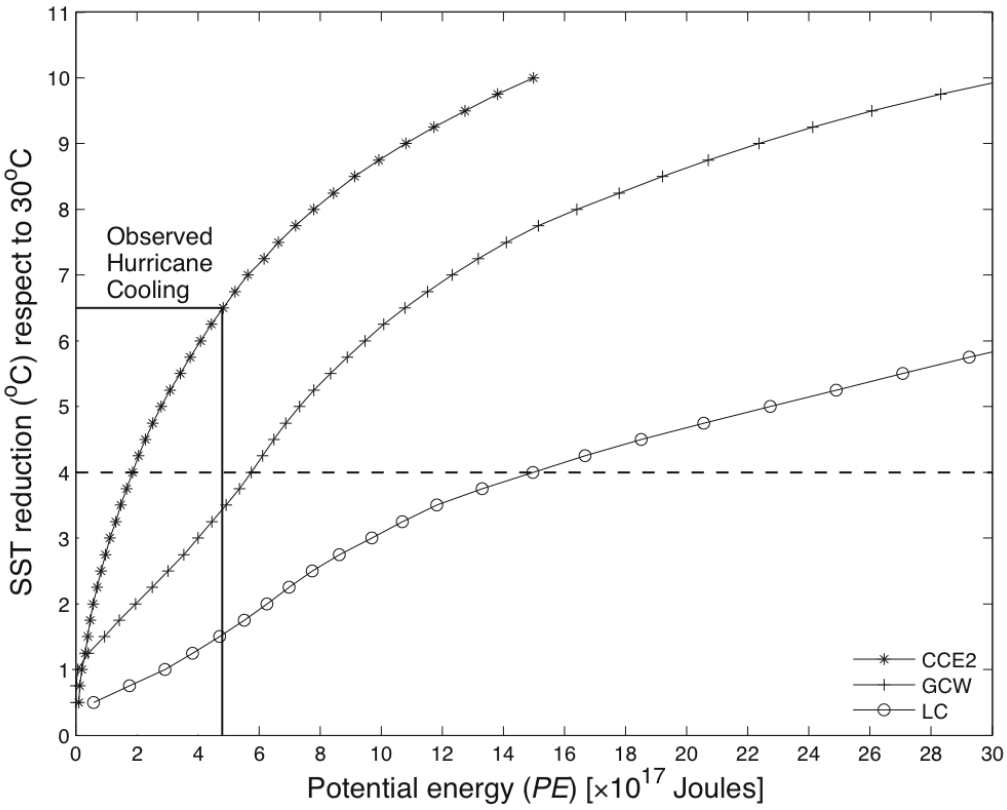

Figure 3.7: Area-integrated energy $PE = 1/2\int_A \rho_o g h_{iso}^2 dA$, required to reduce SST respect to 30°C in a 1°×2° box by adiabatic lifting of isotherms over a vertical distance h_{iso} (from airborne pre-Rita data, 15 September). For example, a 1°C (4°C) SST reduction means that the 29°C (26°C) isotherm was lifted adiabatically to the sea surface against the gravity acceleration. The rectangular area represents observed SST cooling ranges in the GOM during hurricanes Ivan (2004), and Katrina and Rita (2005). The upper limits of this rectangle are determined by the intersection of the average SST cooling observed during hurricane Ivan (~6.5°C) with the PE curve of the CCE2. The intersection of the PE curves with the dashed line indicates that about 2, 6, and 15×10^{17} J are required to adiabatically reduce SST to 26°C over CCEs, GCW, and LC/WCEs, respectively.

To estimate the time required ΔT_{nf} for hurricanes Katrina and Rita to cool the OML to 26°C, we assume (i) an ocean initially in geostrophic balance; (ii) stationary mesoscale eddies relative to hurricane passage; (iii) the momentum flux excites ageostrophic OML currents (no energy lost to dissipation, internal wave radiation into the thermocline, or to strengthen the background flow); (iv) the momentum flux into the

OML is bounded by the saturation level of the sea state; and, (v) the kinetic energy of the hurricane-induced ageostrophic currents is used for adiabatic lifting of isotherms (conversion to available potential energy). The rate of energy transfer from the storm to the OML (hurricane work h_w) is defined as:

$$h_w = \int_A \frac{1}{2} \rho_o u_s^2 U_h \, dA \,, \tag{3.4}$$

where u_s is the OML ageostrophic velocity response, and the term $\rho_o u_s^2/2$ is the kinetic energy injected by the storm into the OML currents. The hurricane work (h_w) on the OML is proportional to the product of the translation speed of the storm U_h and the square of u_s (Geisler 1970; Nilsson 1995). For slow moving or stationary storms ($U_h \rightarrow 0$, or Fr = $U_h c_1^{-1} < 1$), the product $u_s^2 U_h$ must be replaced by u_s^3 in Eq. (3.4). Thus, the time required to shut down the energy source is given by $\Delta T_{nf} = \text{PE}\ h_w^{-1}$, with potential energy defined in the caption of Fig. 3.8.

For storms similar to Katrina or Rita propagating over CCEs, the energy source could be shut down during the first few hours of wind action even at tropical storm force (Fig. 3.8) (consistent with T_{nf} in Fig. 3.6). By contrast, over WCEs the energy source could be depleted only if a series of storms with characteristics similar to Katrina propagated over the warm features during a period of 2 days, or during 10 to 14 days for conditions comparable to Rita. The storm intensity changes observed in Fig. 3.8 indicate that both Katrina and Rita reached category 5 status over regions where the negative feedback was reduced, while they weakened over regions where this negative feedback was increased (i.e., GCW).

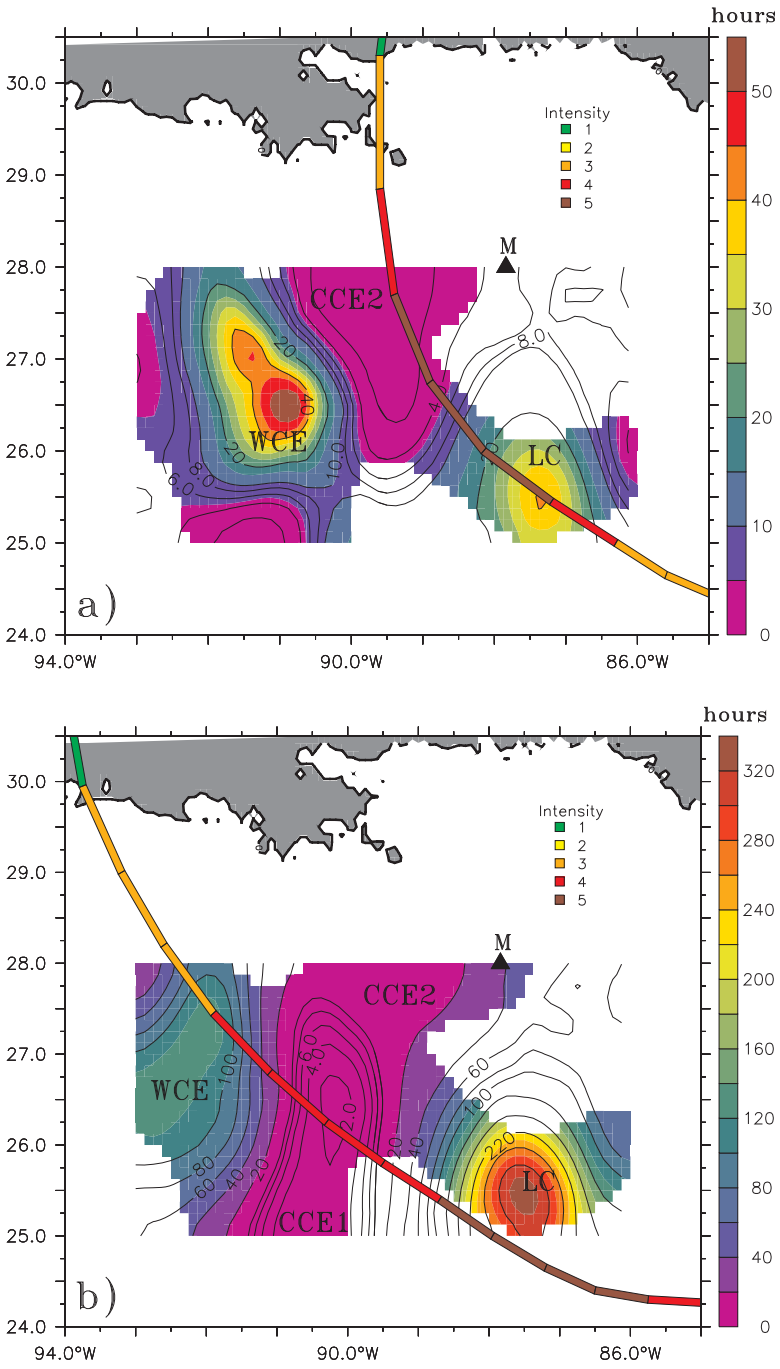

Figure 3.8: Time required, $\Delta T_{nf} = PE\ h_w^{-1}$, to reduce the energy source for Katrina (a) and Rita (b), with $PE = 1/2 \int_A \rho_o g h_{26}^2 dA$, where h_{26} is the 26°C isotherm depth, dA the grid size of the objectively analyzed map, and h_w from Eq. (3.4). In (a) and (b), h_{26} is from pre-Rita (15 September) and post-Rita (26 September) airborne data, respectively. Contour intervals are: 2 hrs from 0 to 10, and 20 hrs from 20 to 340. See caption of Fig. 3.7 for the meaning of *PE*.

Given the assumptions made during the derivation of h_w [Eq. (3.4)], the values of ΔT_{nf} represent an upper bound of the time required to shut down the energy source, as some of the ignored processes, such as diabatic mixing, horizontal advection of thermal structure, and OML kinetic energy lost to dissipation and internal wave radiation will impact these estimates. However, the spatial variability of ΔT_{nf} underscores the importance of the presence of mesoscale oceanic eddies for oceanic feedback mechanisms to hurricanes.

3.6 Summary and concluding remarks

Rapid intensity changes were observed during Katrina and Rita passages over mesoscale ocean features in the eastern GOM. Data acquired during both storms indicated that rather than with SST, the storm's sea-level pressure decreases correlated better with the 26^{o}C isotherm depth and OHC relative to this isotherm, which exhibited spatial variability associated with the presence of WCEs and CCEs as found during hurricane Ivan (Walker et al. 2005; Halliwell et al. 2008). Reduced OML cooling (~1^{o}C) was measured over the LC bulge where both storms reached category 5 status, and increased OML cooling (~4 to 5^{o}C) was observed over the cold cyclones where the storms weakened to category 3 status prior to landfall in the northern Gulf coast.

Pre-storm geostrophic flow imposes important dynamical constraints on the wind-driven vertical velocity. Observational data of the Loop Current system's thermal structure indicate that Rita's wind stress caused upwelling of isotherms inside a CCE, and downwelling inside a WCE. Based on a simplified vorticity balance (Stern 1965), the hypothesis here is that upwelling regimes occur in regions where the wind stress vector is with surface geostrophic flows, while downwelling regimes occur over regions where the

wind stress vector is against surface geostrophic currents. In this context, upwelling velocities of ~0.5 cm s^{-1} were calculated for regions more than $2R_{max}$ ahead of the storm's center for Rita, in agreement with previous studies (D'Asaro 2003; Jacob and Shay 2003).

A parametric OML velocity response from the forced equations of motion predicted that the amplitude of the OML current response is mainly a function of the pre-storm OML depth associated with the geostrophic features, as noticed during the OML response to hurricane Gilbert (Jacob and Shay 2003). Density and thermal structures associated with these ocean features determine *a priori* the time required to shut down the TC energy source. Shallow 26^{o}C isotherm depths inside CCEs have a negative impact on storm intensity, even during the first three hours of the forced stage. By contrast, deeper 26^{o}C isotherm depths in the LC and WCEs provide a continuous energy source for tropical cyclones to intensify under favorable atmospheric conditions.

The contrasting levels of OML turbulent cooling induced by a hurricane in WCEs and CCEs during the forced stage, and the wind-driven upwelling in geostrophic vortices, are addressed in more detail in Chapter 5 via numerical experimentation.

Chapter 4

Near-Inertial Wave Wake

Data acquired in the LC system, during and subsequent to the passage of hurricanes Katrina and Rita, are used to investigate the contrasting evolution of near-inertial currents forced by severe hurricanes over oceanic cyclones (CCEs) and anticyclones (LC and WCEs). The processes involved are introduced, and the near-inertial velocity and temperature responses are resolved. The modulation of the near-inertial response is analyzed in terms of a ray-tracing technique of near-inertial waves in geostrophic shear, the evolution of the effective Coriolis parameter f_e, frequency shifting, and vertical energy dispersion. The development of a "critical layer" inside a CCE affected by Katrina is discussed. An assessment of the contribution from Katrina and Rita wind stress to the global internal wave power is presented.

4.1 Processes involved

Within the framework of linear theory a wake develops in the ocean behind a moving hurricane when the storm's translation speed U_h exceeds the phase speed of the first baroclinic mode c_1 (Froude number $Fr = U_h / c_1 > 1$, Geisler 1970; Shay et al. 1989). Following the TC-induced upwelling, the currents in the wake become more near-inertial after the first half IP, and their transport converges toward the storm track which forces

the downwelling of isotherms. A near-inertial cycle of upwelling and downwelling develops, and horizontal pressure gradients couple the wind-forced OML with the thermocline as part of the three-dimensional wave wake (Price 1981, 1983; Brooks 1983; Shay and Elsberry 1987; Shay et al. 1989, 1998). The representation of the wave wake as a sum of forced baroclinic vertical modes has been shown to be in good agreement with observational data: about 70 to 80% of the near-inertial energy is contained in the four gravest vertical modes, which govern the wake dynamics (Shay and Elsberry 1987; Shay et al. 1989, 1998). Vertical shear instability (gradient Richardson number $R_i < 1/4$) of near-inertial currents in the upper ocean has been found to be associated with the third and fourth forced baroclinic modes (Shay et al. 1989). This shear instability causes turbulent vertical mixing between OML and thermocline waters and produces about 85% of the TC-induced OML cooling, based on measurement (Shay et al. 1992; Jacob et al. 2000; Shay et al. 2000), theoretical studies (Greatbatch 1984) and numerical experiments (Price 1981; Hong et al. 2000). A rightward bias in the SST response is commonly observed, as the velocity response is stronger on the right of the storm track under quiescent or weak background flow conditions (Price 1981, 1983; Jacob and Shay 2003).

Although the kinetic energy (KE) supplied by the wind stress is initially confined in the OML, vertical and horizontal wave dispersion associated with near-inertial motions spread this KE (e.g. Rubenstein 1983; Gill 1984; Nilsson 1995). Vertical dispersion beneath the OML typically depends on the stratification, and the largest dispersion occurs for a large buoyancy frequency N and for the smallest vertical wavenumber (Klein and Treguier 1993). The vertical transfer of energy is more efficient when the OML is deeper (as in WCEs) because the initial velocity profile has a larger projection on the first

baroclinic mode (Gill 1984). The rate of vertical dispersion of near-inertial KE affects the efficiency to cool the OML, by reducing the amount of KE available in the layer to entrain colder thermocline waters (Linden 1975).

Even though linear theory predicts that the wake's horizontal scales are proportional to the inertial period and the storm's translation speed (Geisler 1970; Greatbatch 1984), direct measurements of near-inertial currents consistently show smaller coherent horizontal scales that are apparently affected by background conditions. This has important implications because vertical dispersion of near-inertial energy strongly depends on the horizontal scale of the near-inertial motion, and it is enhanced for small horizontal scales (Gill 1984). For instance, the local variability of background vorticity causes the near-inertial oscillations to lose their initial horizontal coherence, thus the oscillations accumulate a phase shift over short horizontal length scales of order tens of kilometers and, as a result of the reduction of the horizontal scale, the vertical transfer of energy is more effective because ageostrophic horizontal velocity gradients and inertial pumping become stronger (Rubenstein and Roberts 1986). Moreover, background flow divergence dampens near-inertial motions (Weller 1982), while background vorticity shifts the frequency of the inertial response to either above (in cyclonic background flow) or below (in anticyclonic background flow) the local inertial frequency (Mooers 1975; Olbers 1981; Weller 1982; Kunze 1985). The polarization of inertial motions by the background flow can lead to non-negligible Ekman transport divergence (inertial pumping), even with a uniform wind stress (Klein and Hua 1988).

Vertically propagating wave groups much more energetic than the local downgoing near-inertial wave field have been observed in anticyclonic circulations

(Kunze and Sanford 1984; Kunze 1986; Mied et al. 1986; Kunze et al. 1995). This behavior was explained with a wave-mean flow interaction model that predicted trapping and amplification of linear waves in regions of anticyclonic vorticity (Kunze 1985). In this model, the waves' frequency is shifted from f to $f_e = f + \zeta_g / 2$ in the presence of geostrophic background flow (f_e is the effective Coriolis parameter, and ζ_g the background geostrophic relative vorticity), such that horizontal gradients in f_e refract the waves leading to trapping in anticyclonic flows. Predictions from three-dimensional, nonlinear dynamical models (Lee and Niiler 1998) were consistent with Kunze's (1985) linear model: (i) in anticyclones, the propagation direction is downward and toward the core, such that near-inertial energy is radiated downward from the surface to the thermocline; (ii) in cyclones, wave propagation was outward from the core of the eddy, and near-inertial energy was found only in OMLs.

The geostrophic modulation of the wake of Katrina and Rita is discussed below. Understanding the processes driving this modulation is important, because by changing the scales and dispersion characteristics of near-inertial motions they can affect timing, extension, and rate of TC-induced vertical mixing and cooling in the upper ocean, thereby limiting the contribution from the TC-induced near-inertial motions to the global ocean internal wave power.

4.2 Near-inertial velocity response

The contrasting hurricane-induced near-inertial response is a function of the underlying geostrophic flow as observed at the mooring locations. The velocity response inside the CCE2 consisted of strong cross-track currents of approximately 80 cm s^{-1}

rotating anticyclonically with depth (Fig. 4.1a). Similar near-inertial properties were observed in the northern portion of the LC (Fig. 4.1b), although in this case the velocity response was considerably weaker with maximum velocities of ~40 cm s^{-1}. Despite differing velocity responses, the CCE2 and LC bulge were under the action of comparable wind forcing because Katrina and Rita surface winds were about 70 m s^{-1} when they impacted these eddies (Fig. 2.8a, b).

The coupling between the translation speed of the storm U_h and the phase speed of the first baroclinic mode c_1 determines whether the upper ocean response is in the form of upwelling or a near-inertial wave wake (Geisler 1970, Nilsson 1995). To evaluate the contrasting near-inertial velocity response excited by a wind stress over WCEs and CCEs, consider a two-layer approach in which c_1 is given by

$$c_1^2 = g\frac{(\rho_{dn} - \rho_{20})h_{20}h_{dn}}{\rho_{dn}(h_{20} + h_{dn})},$$

where h_{20} is the 20°C isotherm depth (proxy for the thermocline in the GOM, Shay et al. 1998), h_{dn} is the thickness of the layer extending from h_{20} down to 1000 m, and ρ_{20} and ρ_{dn} are vertically-averaged densities upon h_{20} and h_{dn}, respectively. The maximum values of c_1 from this thermal structure were ~2.9 m s^{-1} in the LC and 2.1 m s^{-1} in CCE2 (Table 3.1). As Katrina and Rita translation speeds were faster than c_1, their respective Froude numbers (defined as $Fr = U_h\, c_1^{-1}$) exceeded unity (Table 3.1), indicating a baroclinic near-inertial current response driven by wind stress (Geisler 1970). This behavior is consistent with the velocity response observed at the mooring site. By contrast, the Fr is larger in CCE2 because c_1 is slower than in the LC. This indicates that the spatial variability of c_1 contributes to the differentiated near-inertial velocity response observed in WCEs and CCEs during Katrina and Rita.

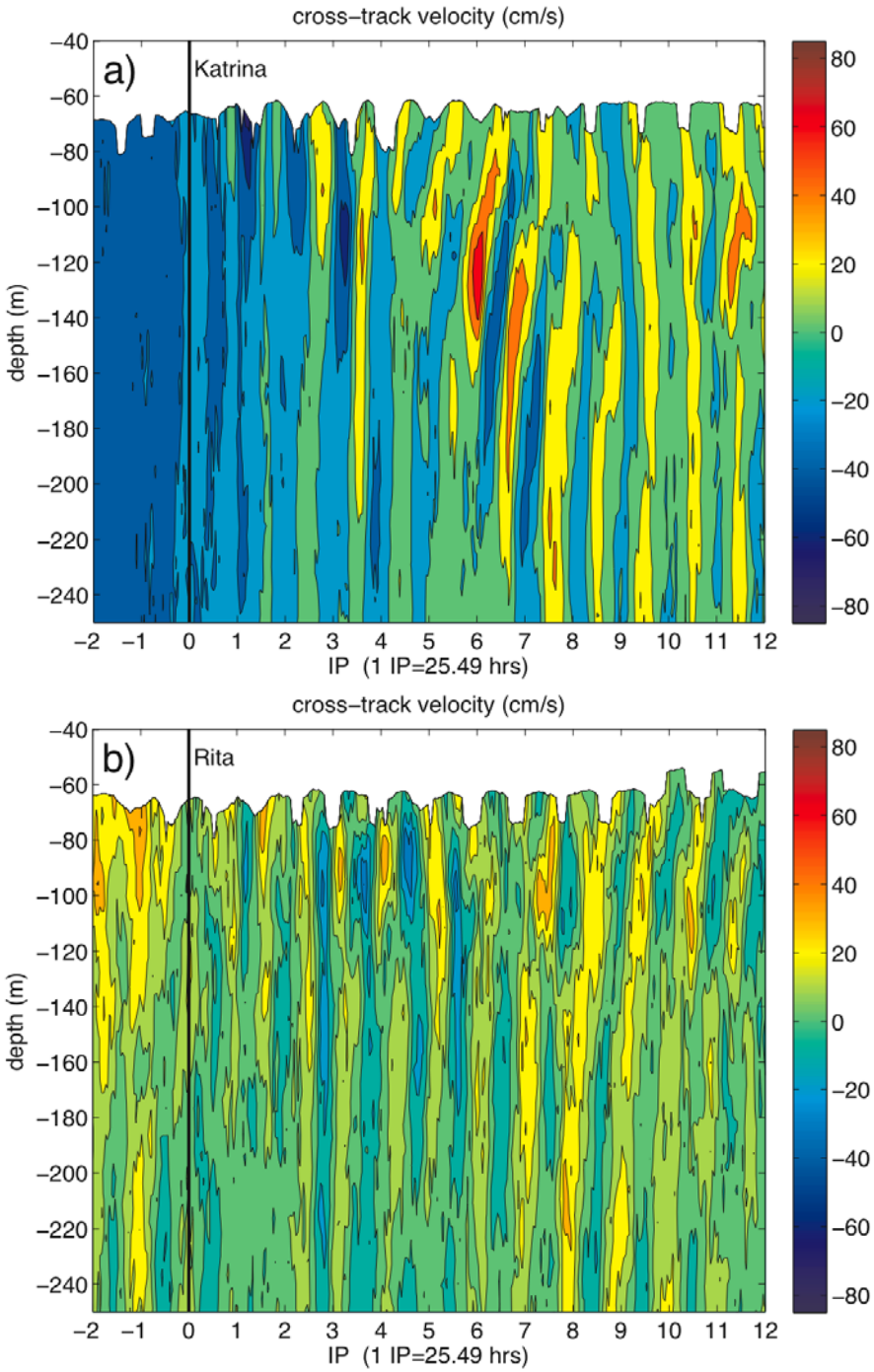

Figure 4.1: Cross-track velocity response at the mooring site (point M, Fig. 2.1). (a) Inside the CCE2 that interacted with Katrina (Fig. 2.8a), and (b) inside the LC bulge affected by Rita (Fig. 2.8b). The vertical lines indicate the time of closest approach of the hurricane's eye to the mooring site (29 August for Katrina; 23 September for Rita).

4.3 Near-inertial temperature response

4.3.1 Vertical shear

The near-inertial response inside the CCE2 shows a clockwise (CW) rotation of horizontal currents with depth, with two regimes separated at about the 250-m depth (Fig. 4.2a). In the surface regime, the rotating helices of the velocity vector (envelops of the stick vectors) resemble a downward phase propagation that indicates upward energy propagation (Leaman and Sanford 1978). By contrast, beneath 250-m depth, the phase propagates upward (downward energy propagation). Vertical energy propagation is investigated in more detail in section 4.4.4. Notice that in the surface regime, the current amplitudes increased from the depth to the surface, reaching maximum levels of O(60 cm s^{-1}) between 100 to 200-m depths. At these depth levels, the maximum cooling occurred (see for instance the change in color of the stick vectors near the 100-m depth from 6 to 7 IP, indicating a cooling of ~4 to 5^{o}C). The vertical distribution of the gradient Richardson number (Ri) indicates that this maximum cooling was driven by shear instability (Fig. 4.2b). Notice that wave activity diminished above the depth of maximum shear instability.

Inside the LC bulge, the near-inertial response exhibited CW velocity rotation with depth (Fig. 4.3a), though the amplitude was about one-half the value observed in the CCE2. Other important differences with respect to the CCE2 were: (i) in the LC bulge there was no significant amplification of the velocity response with depth; (ii) downward energy propagation predominated (section 4.4.4); and, (iii) cooling was negligible, as Ri was above criticality (Fig. 4.3b).

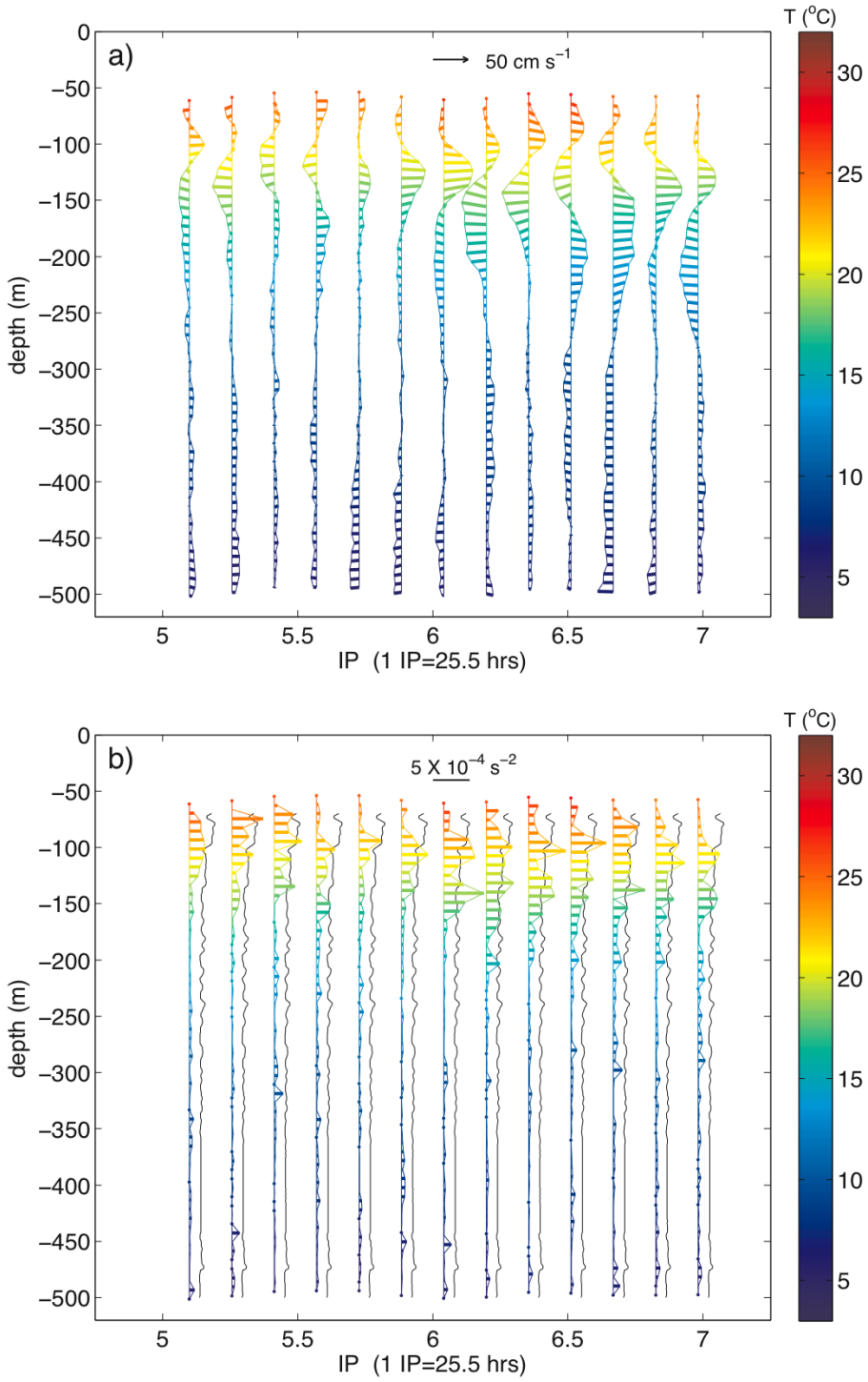

Figure 4.2: Near-inertial response to Katrina in the CCE2, as observed at the mooring site (87.839°W, 27.998°N). (a) Horizontal velocity response, and (b) square of the vertical shear of horizontal currents $S^2 = (\partial u/\partial z)^2 + (\partial \upsilon/\partial z)^2$. The black curves in each profile in (b) are $4N^2$, with $N^2 = -(g/\rho_o)(\partial \rho/\partial z)$ the square of a reference buoyancy frequency from a density profile acquired inside the CCE2 during the pre-Rita flight. The gradient Richardson number is $Ri = S^2/N^2$. The theoretical limit for shear instability is $Ri < 1/4$.

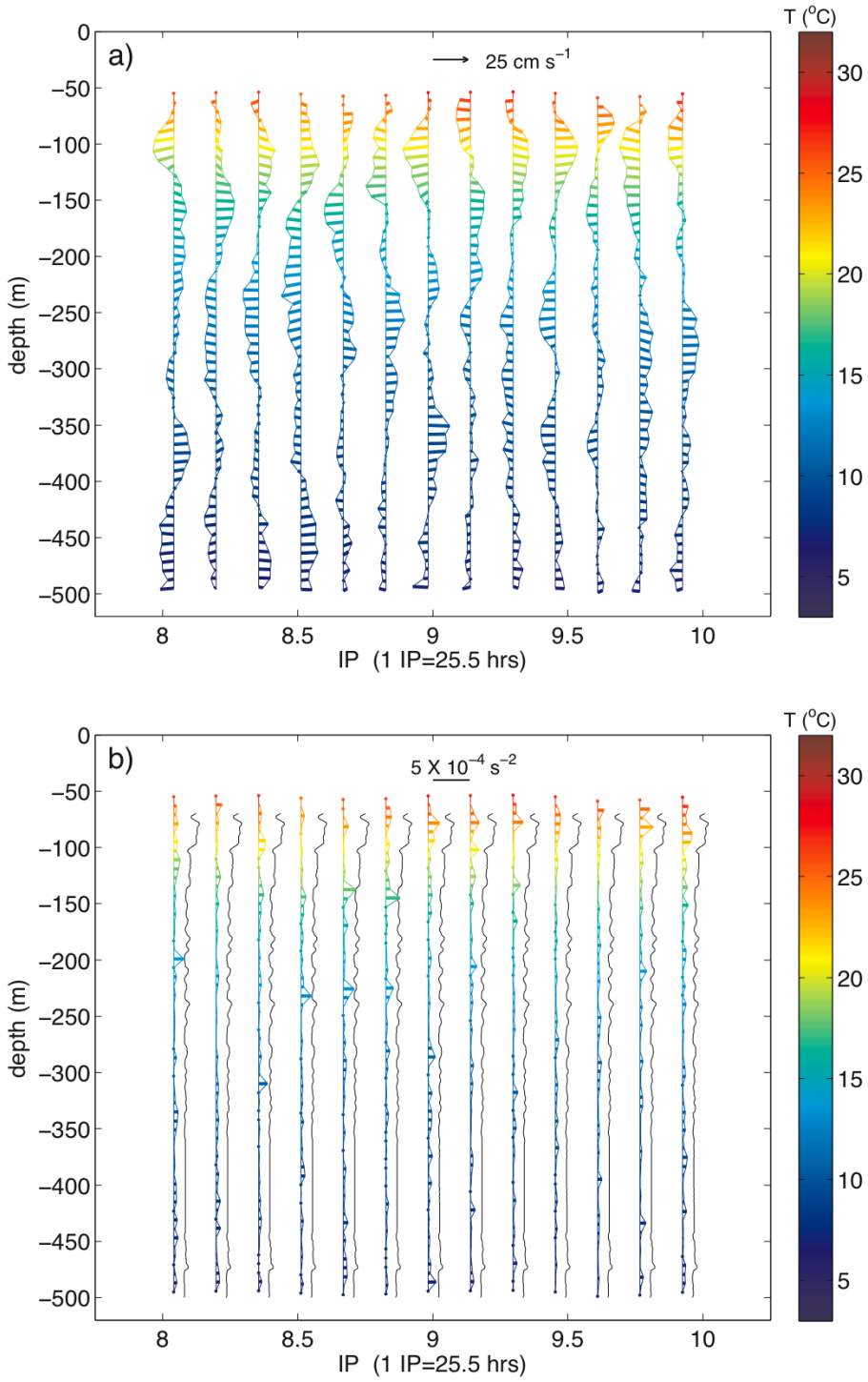

Figure 4.3: As in Fig. 4.2, but for the near-inertial response to Rita in the LC bulge. Notice the scale difference of the velocity vectors between 4.2a (50 cm s^{-1}) and 4.3a (25 cm s^{-1}).

4.3.2 Water mass evolution

The evaluation of water mass at the mooring site reveals that most of the upper ocean cooling was driven by forced near-inertial processes (Fig. 4.4). Given that the near-inertial OML velocity response was stronger inside the CCE2, the vertical current shear caused more intense mixing within this oceanic cyclone. By contrast, mixing and cooling processes were reduced in the LC as both the velocity response and vertical shears were weaker, consistent with measurements in the LC during Isidore and Lili (Shay and Uhlhorn 2008). Notice that in the two cases, shear-induced mixing was confined to neutral surfaces lighter than $\sigma_t = 27$ (within STW).

4.3.3 Cold wake

Temperature profiles acquired during the post-Katrina and post-Rita flights resolved the geostrophic eddy field over which the two storms propagated as major TCs. These data sets provide a unique opportunity to evaluate the contrasting OML cooling levels produced by severe TCs over the LC, WCEs, and CCEs. To this end, we consider the non-dimensional parameter $\varepsilon = a(T_{oml}\text{-}T_B)$ (Chang and Anthes 1978), where $a = 2.9\times10^{-4}/^{o}\text{C}$ is the expansion modulus of water at 25°C and 30 psu, and T_{oml} and T_B are vertically-averaged temperatures over the OML, and between the OML base and the 20°C isotherm depth, respectively. This parameter is multiplied by the gravitational acceleration constant g thereby providing a measure of the reduced gravity g'.

Given that ε accounts for the temperature (and density) difference between OML and thermocline waters, it is used here as a cooling mixing parameter, such that smaller values of ε would indicate well-mixed waters between the OML and the thermocline.

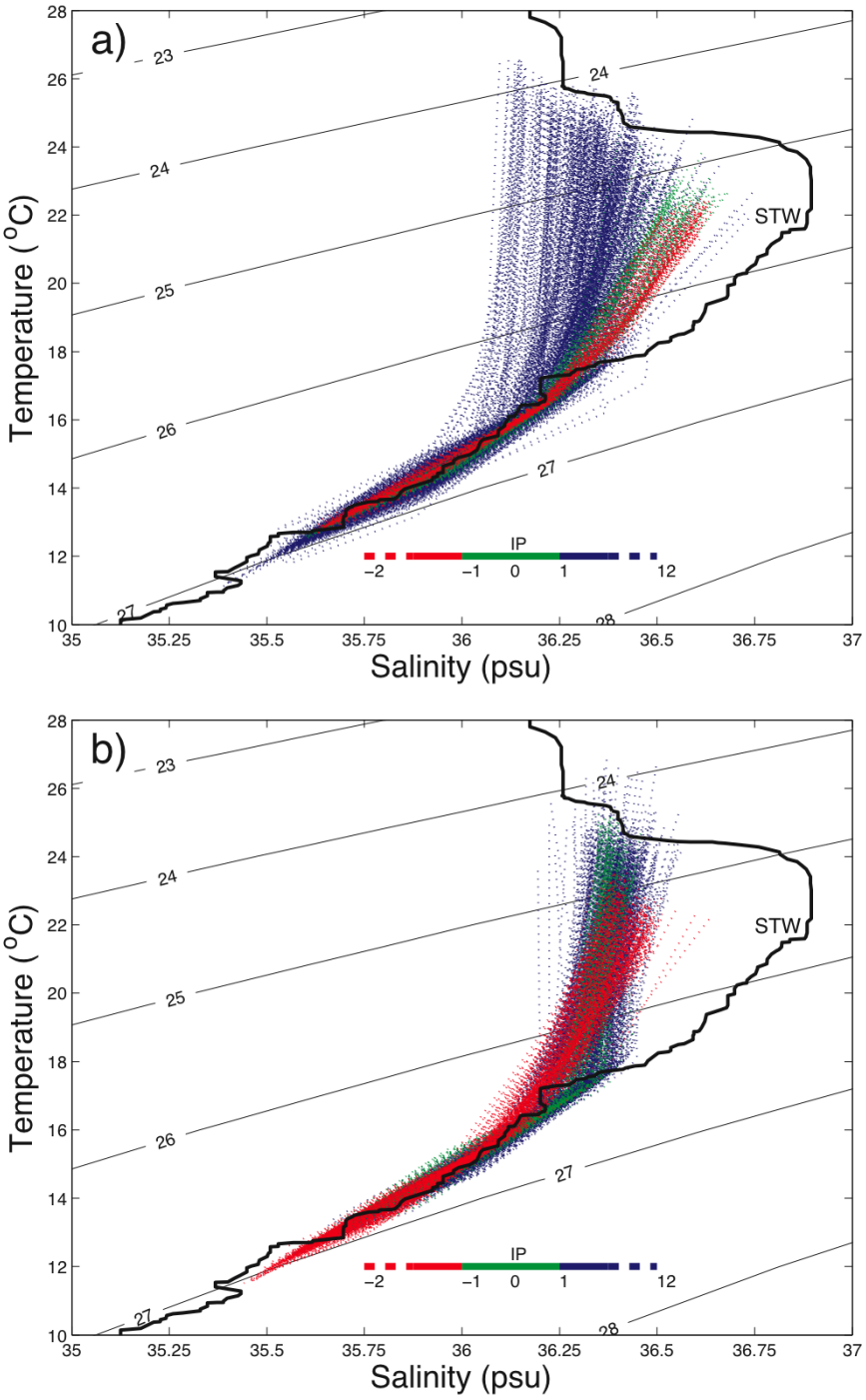

Figure 4.4: Water mass evolution at the mooring site (point M, Fig. 2.1). (a) Inside the CCE2 that interacted with Katrina (Fig. 2.8a), and (b) inside the LC bulge affected by Rita (Fig. 2.8b). IP stands for inertial period (25.5 hr), and STW for Subtropical Water. In (a) and (b) the red, green, and blue colors represent pre-, in-, and post-storm (near-inertial) variability, respectively. The black line represents a reference water mass from the WCE core (Jaimes and Shay 2009a).

Under relatively quiescent ocean conditions, the cold wake of a hurricane is typically elongated, and extends along the right side of the storm's track over a distance of $O(10^3$ km) in the direction of storm propagation (e.g. Chang and Anthes 1978; Price 1981, 1983; Greatbatch 1984; Shay et al. 1989). However, these characteristics were not necessarily observed following the passage of Katrina over the LC system eddies, as the region of maximum cooling was located to the left of the storm's track two weeks after storm passage (Fig. 4.5a), indicating important horizontal advection in the wake by the background geostrophic flow. Notice the high correlation levels between the region of maximum cooling and the underlying cyclonic-rotating flow isolines, suggesting that the wake was arrested by a westward-propagating CCE. Similar displacement of the cold wake was observed after the passage of TC Ivan over LC system's CCEs (Walker et al. 2005; Halliwell et al. 2008, 2009).

In the case of Rita, the region of maximum cooling remained on the right side of the track three days following the storm's passage, and was confined to an area where CCE1 and CCE2 apparently merged (Fig. 4.5b). Notice that the region of maximum cooling in Rita's wake is larger than that for Katrina. This enhanced wake could have resulted because Rita moved over the wake of Katrina. The high cooling levels on the left of Rita's track are remnants of Katrina's wake that apparently were advected by the geostrophic flow. Similar to Katrina's case, Rita produced reduced cooling levels over anticyclonic features (LC bulge). Overall, the contrasting upper-ocean mixing levels associated with the passage of the two storms exhibited the following pattern (in terms of ε): (i) increased mixing in CCEs; (ii) intermediate mixing along frontal regions that separate CCEs and WCEs; and (iii) reduced mixing in anticyclones (LC and WCEs).

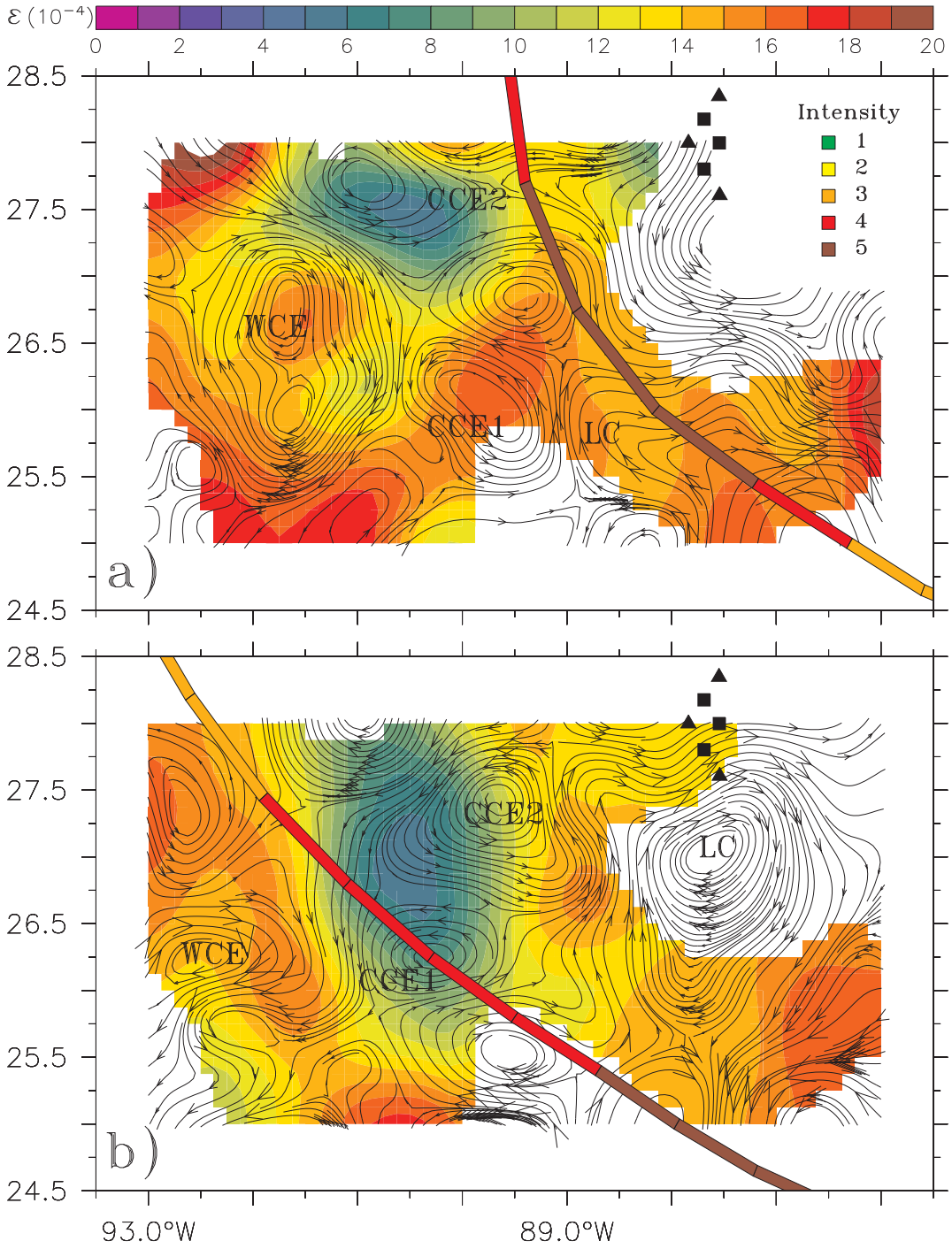

Figure 4.5: Vertical mixing induced by (a) Katrina and (b) Rita in the upper ocean, in terms of the mixing parameter ε evaluated from the thermal structure observed during the (a) post Katrina (15 September) and (b) post Rita (26 September) flights. The color shade shows regions with mapping errors less than 40% from the objective analysis technique. Flow lines are for the geostrophic flow derived from the post-storm flights. Black triangles are MMS moorings, and black squares are interpolation points to calculate vorticity from mooring data (Jaimes and Shay 2009b).

4.4 Modulation of the near-inertial response

4.4.1 Near-inertial wave ray tracing

To explore the effects of the geostrophic eddies on the near-inertial wave wake structure, a ray trace model is used here to investigate the propagation of near-inertial waves in a geostrophically balanced flow field (Kunze 1985). In this model, the wave's position is given by

$$\frac{d\mathbf{r}}{dt} = \mathbf{C}_g + \mathbf{V}_g , \tag{4.1}$$

and wavenumber vector

$$\frac{d\mathbf{K}}{dt} = -\nabla\omega , \tag{4.2}$$

where $\mathbf{r} = x\,\mathbf{i} + y\,\mathbf{j} + z\,\mathbf{k}$, $\mathbf{K} = k_x\,\mathbf{i} + k_y\,\mathbf{j} + k_z\,\mathbf{k}$, and the dispersion relation is

$$\omega = \omega_o + \left(\mathbf{K}\cdot\mathbf{V}_g\right) = \text{constant} , \tag{4.3}$$

with

$$\omega_o \approx f_e + \frac{N^2 k_H^2}{2 f k_z^2} + \frac{1}{k_z}\left(\frac{\partial U_g}{\partial z}k_y - \frac{\partial V_g}{\partial z}k_x\right), \tag{4.4}$$

where $k_H^2 = k_x^2 + k_y^2$, ω and ω_o the Eulerian and intrinsic frequencies, respectively, $\mathbf{V}_g = U_g\,\mathbf{i} + V_g\,\mathbf{j}$ the geostrophic flow, and $\mathbf{K}\cdot\mathbf{V}_g$ represents a Doppler shift.

Given the strength of horizontal advection of $O(1)$ m s^{-1} in the LC system, the Doppler shift term in Eq. (4.3) becomes potentially larger. Note that Eq. (4.4) contains only the real part of the dispersion relation as Kunze (1985) ignored the imaginary part based on heuristic scaling arguments, thus neglecting the energy exchange between waves and mean flow and mean horizontal straining of waves by ray confluence.

Table 4.1: Initial conditions for near-inertial wave ray tracing, with $k_x=2\pi/\lambda_x$, $k_y=2\pi/\lambda_y$, and $k_z=2\pi/\lambda_z$ the zonal, meridional, and vertical wavenumber components, respectively. Positive values of wavelengths λ_x, λ_y, and λ_z are in the eastward, northward, and downward direction, respectively. The values of λ_z were determined from direct ADCP velocity measurements as in Brooks (1983), and $\lambda_x = 4R_{max}$, with R_{max} the radius of maximum winds of Katrina (CCE2) and Rita (LC bulge). The initial depth of the rays was 40 m. T_i is the inertial period (see text for description of the other parameters).

	Δz (m)	ΔT_z (hr)	T_i (hr)	$\overline{N}$ (c.p.h.)	λ_x (km)	λ_y (km)	λ_z (m)
CCE2	425	8.1	23.7	4.8	168	0	144
LC	425	12.3	24.3	6.1	76	0	214

Theoretical studies suggest that when straining dominates relative vorticity, the wave rays can experience exponential stretching, such that the waves are captured by the background flow eventually enhancing eddy-mean energy exchanges (Bühler and McIntyre 2005). Under these circumstances straining cannot be ignored.

To obtain the initial values of **K** (Table 4.1), current measurements from the ADCP mooring (point M, Fig. 2.1) were used to calculate the near-inertial wave parameters by assuming a constant buoyancy frequency (Brooks 1983). For a constant buoyancy frequency the group velocity vector is $\mathbf{C}g = Cg_x\mathbf{i} + Cg_z\mathbf{k}$, with **i** and **k** the unity vectors in the cross-track and vertical direction, respectively, and Cg_x and Cg_z given by

$$Cg_x = \omega_i k_x^{-1}(\overline{N}\omega_i^{-1}\tan\theta)^2, \tag{4.5a}$$

$$Cg_z = \omega_i k_z^{-1}(\overline{N}\omega_i^{-1}\tan\theta)^2, \tag{4.5b}$$

where $k_x=2\pi/\lambda_x$, $k_z=2\pi/\lambda_z$, and ω_i is the near-inertial wave frequency. $\overline{N}$ is a constant buoyancy frequency vertically-averaged over a water column of thickness Δz that excludes the OML; $\tan\theta = \lambda_z/\lambda_x$ where $\lambda_x = 4R_{max}$ and $\lambda_z = \omega_i \Delta z \Delta t_z$ are the wavelengths in the cross-track and vertical direction, respectively. Here, it is assumed that initially $\lambda_y=\lambda_x$, Δz is the distance traveled by a wave (measured perpendicular to the crest line) in the

vertical direction, and Δt_z is the phase lag between the two depth levels (Δz). The layer thickness used during this analysis was Δz = 425 m, and the upper and lower depth levels were taken as 75 and 500 m, respectively. Cross-track velocity time series from these depth levels were used to calculate time-averaged phase lags (Δt_z) of 8.1 and 12.3 hrs for the CCE2 and LC bulge, respectively. A least-squares frequency fit analysis conducted over the time span when the CCE2/LC intruded over the mooring site (section 4.4.3) indicated that the near-inertial response was shifted toward higher (lower) frequencies inside the CCE2 (LC bulge). On average, the corresponding near-inertial periods were 23.7 and 24.3 hrs for the CCE2 and LC, respectively. Since AXBTs provide a higher vertical resolution of the thermal structure, a profile from the pre-Rita flight was used to calculate a vertically-averaged buoyancy frequency $\overline{N}$ = 4.7 c.p.h for the CCE2, and a profile from the post-Rita flight was used to calculate $\overline{N}$ = 6 c.p.h inside the LC bulge.

The set of equations (4.1)–(4.2) was numerically solved with a fourth-order Runge-Kutta method, and the geostrophic fields $\mathbf{V}_g$ are from the post-Katrina and post-Rita ocean profilers (section 2.1.4). Initial wave positions were aimed to capture propagation characteristics in the LC flow regimes (Fig. 4.6). The ratio $(f_e - |S_t|)/f$ was calculated to assess the choice of neglecting the horizontal straining terms in Eq. (4.4), where $s_t = \left(\left(\partial U_g / \partial x - \partial V_g / \partial y \right)^2 + \left(\partial V_g / \partial x + \partial U_g / \partial y \right)^2 \right)^{1/2}$. As shown in Fig. 4.6, f_e was in general larger than S_t over most of the region of study. For practical purposes, Kunze's (1985) model can be used without the geostrophic straining terms in this particular case.

In accord with the theoretical expectation (Kunze 1985) and numerical experiments (Lee and Niiler 1998), the model predicted that Katrina-forced near-inertial waves initially propagating downward from the OML (k_z > 0) are trapped in WCEs,

reaching the seasonal thermocline (~200 m depth) in about 5 IP (Fig. 4.6a). By contrast, waves propagating in CCEs remained at a nearly constant depth (vertical stalling), but were horizontally radiated from the eddy center toward the periphery of the feature.

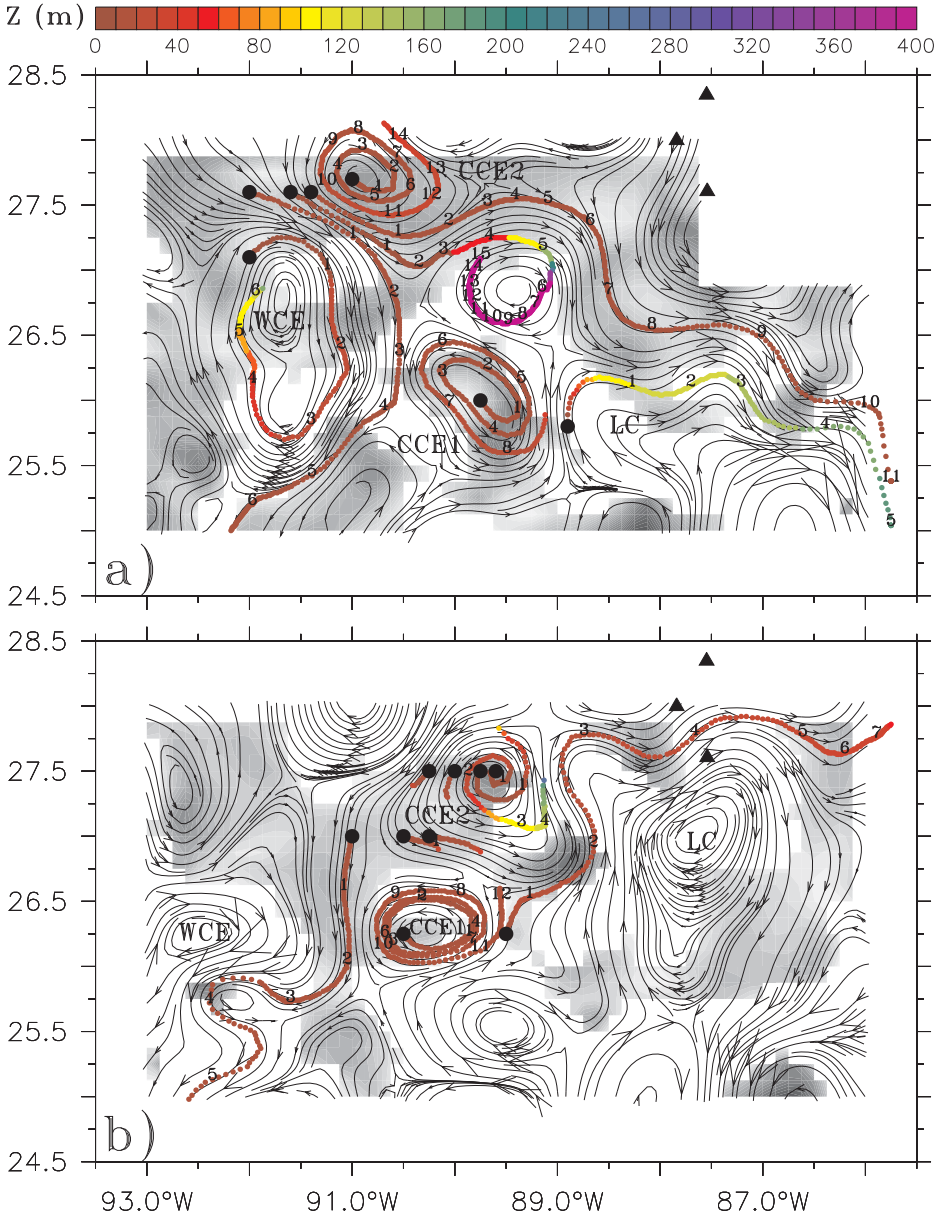

Figure 4.6: Near-inertial wave ray tracing based on Kunze's (1985) model, for (a) Katrina and (b) Rita. The numbers along the wave rays indicate inertial periods (one inertial period is ~25.5 hr), dots are hourly positions, color is the ray's depth level, and the flow lines are from geostrophic flow fields derived from (a) post Katrina (15 September) and (b) post Rita (26 September) airborne-based data. The gray shades represent regions where $(f_e-|S_t|)/f > 0.2$. This ratio, and the flow lines were calculated from depth-averaged velocity fields (Jaimes and Shay 2009b).

Notice the strong mean advection of waves along the LC's northern portion, where the waves rapidly propagated downward in the side of negative relative vorticity. In the case of the Rita-forced near-inertial waves, the model predicted similar propagation patterns to those in Katrina, although the waves propagated over a region with stronger geostrophic horizontal straining (Fig. 4.6b). Several rays inside the CCE2 were short over the region of maximum vertical mixing (at about 90.5^{o}W, 27–27.5^{o}N; cf. Fig. 4.5b, 4.6b) as the predicted wave amplitude grew exponentially during the first IP due to strong horizontal gradients in the cyclonic geostrophic flows.

Near-inertial waves were predicted to slowly disperse only in the horizontal plane, so that they spend more time in surface waters of CCEs that coincide with regions of enhanced vertical mixing and upwelling. This vertical stalling of downward propagating waves in the CCE may induce an accumulation of near-inertial energy in surface layers that may amplify vertical current shears. By contrast, reduced upper ocean vertical mixing occurred over regions of anticyclonic ζ_g where near-inertial waves were rapidly dispersed downward.

4.4.2 Effective Coriolis frequency

Hourly velocity and temperature data from the mooring array (ADCP with a vertical sampling interval of ~8 m, and CTDs deployed every ~40 m, Table 2 of JS09) allow incorporating time dependence, and are used here to complement the investigation of the effects of the geostrophic flow on the wakes of Katrina and Rita. For this purpose, background (mean) relative vorticity ζ_g was calculated to identify the periods over which the mooring array was under the action of the CCE2 and LC bulge that previously

interacted with Katrina and Rita, respectively. To calculate ζ_g, horizontal velocity data from the three moorings (deployed in a triangular array) were first interpolated into midpoints between the moorings (squares in Fig. 4.5). Gaussian-weighted averaging, given by

$$\overline{Q}(z,t) = \frac{\sum_i Q_i(z,t) e^{-r_i^2/r_o^2}}{\sum_i e^{-r_i^2/r_o^2}},$$

was used to obtain interpolated values $\overline{Q}(z,t)$ at these midpoints, where $Q_i(z,t)$ are the velocity data [$u(z,t)$ or $\upsilon(z,t)$], r_i are the distances between the interpolation point and the data points, and r_o is the maximum r_i distance. Hourly velocities from these three midpoints, for each depth level, were used together with the most western mooring data (diamond-type array with vertices at the cardinal points) to compute hourly values of $\zeta(x_c, y_c, z, t) = (\upsilon_E - \upsilon_W)/\Delta x - (u_N - u_S)/\Delta y$ at the diamond's center (x_c, y_c). Finally, ζ_g was calculated, for each depth level, at ¼IP intervals with

$$\zeta_g(x_c, y_c, z, IP) = \frac{1}{M} \sum_{t=IP-2}^{t=IP+2} \zeta(x_c, y_c, z, t),$$

where M is the number of hourly data used to calculate this 5-IP running mean (from IP-2 to IP+2). This 5-IP length was selected based on the estimated time that the eddies remained over the mooring, and to increase the statistical significance of the mean compared with 1-IP running means aimed to resolve near-inertial waves in other context.

The evolution of ζ_g at the mooring array shows alternations as a function of the arrival of cyclonic and anticyclonic features (Fig. 4.7). Notice that the IP scaling in Fig. 4.7 is reset to zero at the time of closest approach of Rita to the mooring array. Thus, the

first IP segment corresponds to Katrina and the second to Rita. The period from about 4 to 13 IP (Katrina segment) is associated with the arrival of the CCE2, and the negative values of ζ_g from 15 to 19 IP correspond to an intrusion of the LC bulge prior to Rita's passage. The period from about 6 to 10 IP (Rita segment) captures the intrusion of the LC bulge under the influence of Rita. For the remainder of this chapter the focus is on the periods from 5 to 8 IP in the case of the CCE2 (Katrina segment, or CCE hereafter), and from 7 to 10 IP in the case of the LC bulge (Rita segment).

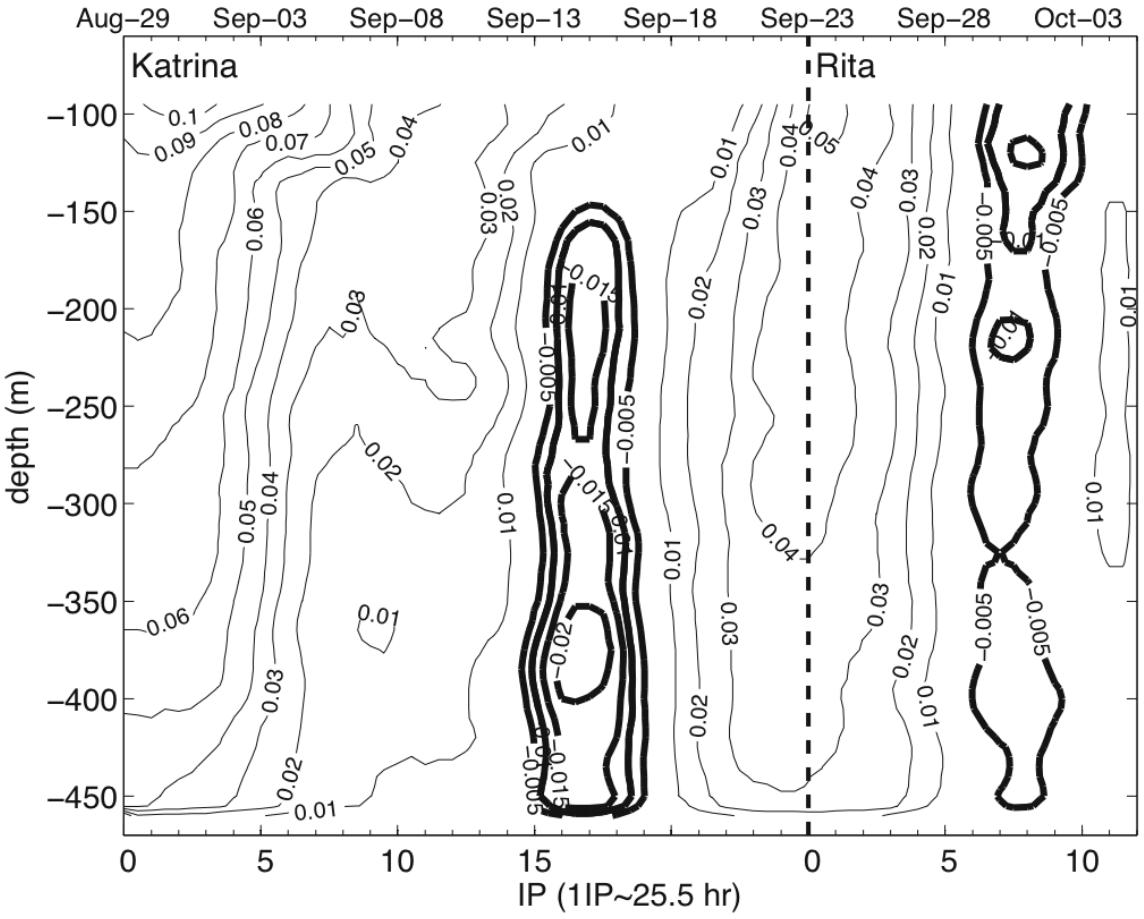

Figure 4.7: Evolution of background relative vorticity ζ_g (normalized by f) at the mooring array during the passage of hurricanes Katrina and Rita (5-IP running means, see text for details). The horizontal axis stands for inertial periods counted from the time of closest approach of the storm to the mooring array. Thin (bold) contours are for cyclonic (anticyclonic) relative vorticity.

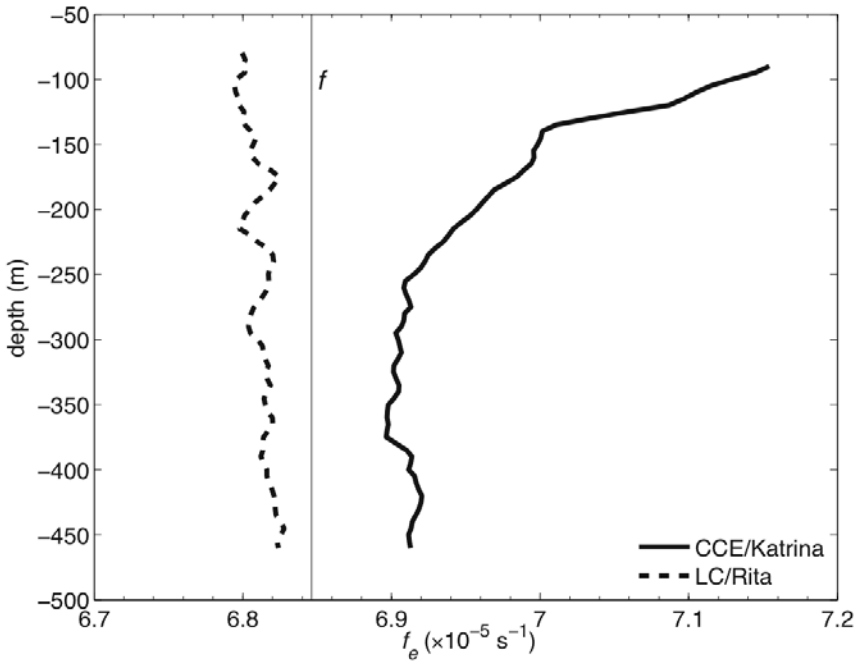

Figure 4.8: Time-averaged effective Coriolis parameter $f_e = f + \zeta_g/2$ at the mooring array, inside the CCE that interacted with Katrina (solid) and the LC bulge affected by Rita (dashed). ζ_g was time-averaged from 5 to 8 IP for the CCE, and from 7 to 10 IP for the LC bulge (see text for details). The vertical line represents the local Coriolis frequency *f*.

The time mean of the effective Coriolis parameter f_e calculated from the time-averaged ζ_g shows contrasting regimes between the CCE and LC (Fig. 4.8). The lower bound of the near-inertial internal wave band is shifted toward higher and lower frequencies in the CCE and LC bulge, respectively, as suggested in theoretical developments (Mooers 1975; Weller 1982; Kunze 1985), and observations (Kunze and Sanford 1984; Kunze 1986; Mied et al. 1986, 1987; Kunze et al. 1995). Notice that below the 250 m depth level, f_e is nearly symmetric between the LC and CCE. However, above this depth, f_e is surface intensified in the CCE as the vorticity gradients tighten. Thus, the expectation is for ζ_g to alter the near-inertial frequency pass-band and vertical wavenumbers that may exist within these eddies.

4.4.3 Frequency shifting

The data from the most western mooring (closest to Katrina and Rita's tracks) were used to diagnose the frequency of the near-inertial oscillations inside the CCE and LC bulge. For each depth level, the velocity components were rotated to the storm coordinate system (cross- and along-track velocities). Kinetic energy was conserved in this coordinate rotation. The perturbation currents were acquired by removing background velocities from 5 to 8 IP in the CCE, and from 7 to 10 IP in the LC bulge. A least-square frequency analysis involved using the perturbation velocities for a series of trial frequencies (Rossby and Sanford 1976; Mayer et al. 1981; Shay and Elsberry 1987). This analysis determines a set of weights (A_1 and A_2, or velocity amplitudes) for each velocity component

$$[u(z,t),\upsilon(z,t)] = A_1 \cos(\omega t) + A_2 \sin(\omega t) + u_r(t), \tag{4.6}$$

where $u(z,t)$ and $\upsilon(z,t)$ are observed perturbation velocities in the cross- and along-track directions, respectively, ω is the trial frequency (from $0.5f$ to $2.5f$), and u_r is the residual velocity after removing the signal with that frequency. The overall quality of the fit (considering the two velocity components) is given in terms of the correlation coefficient

$$r = \frac{\left(r_u^2 + r_\upsilon^2\right)^{1/2}}{2^{1/2}}, \tag{4.7}$$

where $[r_u, r_\upsilon] = ss_{xy}^2 / ss_{xx} ss_{yy}$, with r_u and r_υ the correlation coefficients between observed and modeled velocities for cross- and along-track velocities, respectively, ss_{xy} the covariance matrix between the observed and modeled velocities, and ss_{xx} and ss_{yy} the variance matrices of observed and modeled velocities, respectively. Because of the strength of the near-inertial response, it is assumed that a single carrier frequency exists

(Shay and Elsberry 1987). For each depth, this frequency is defined as the frequency that minimizes the residual covariance (in the present treatment with the highest *r*).

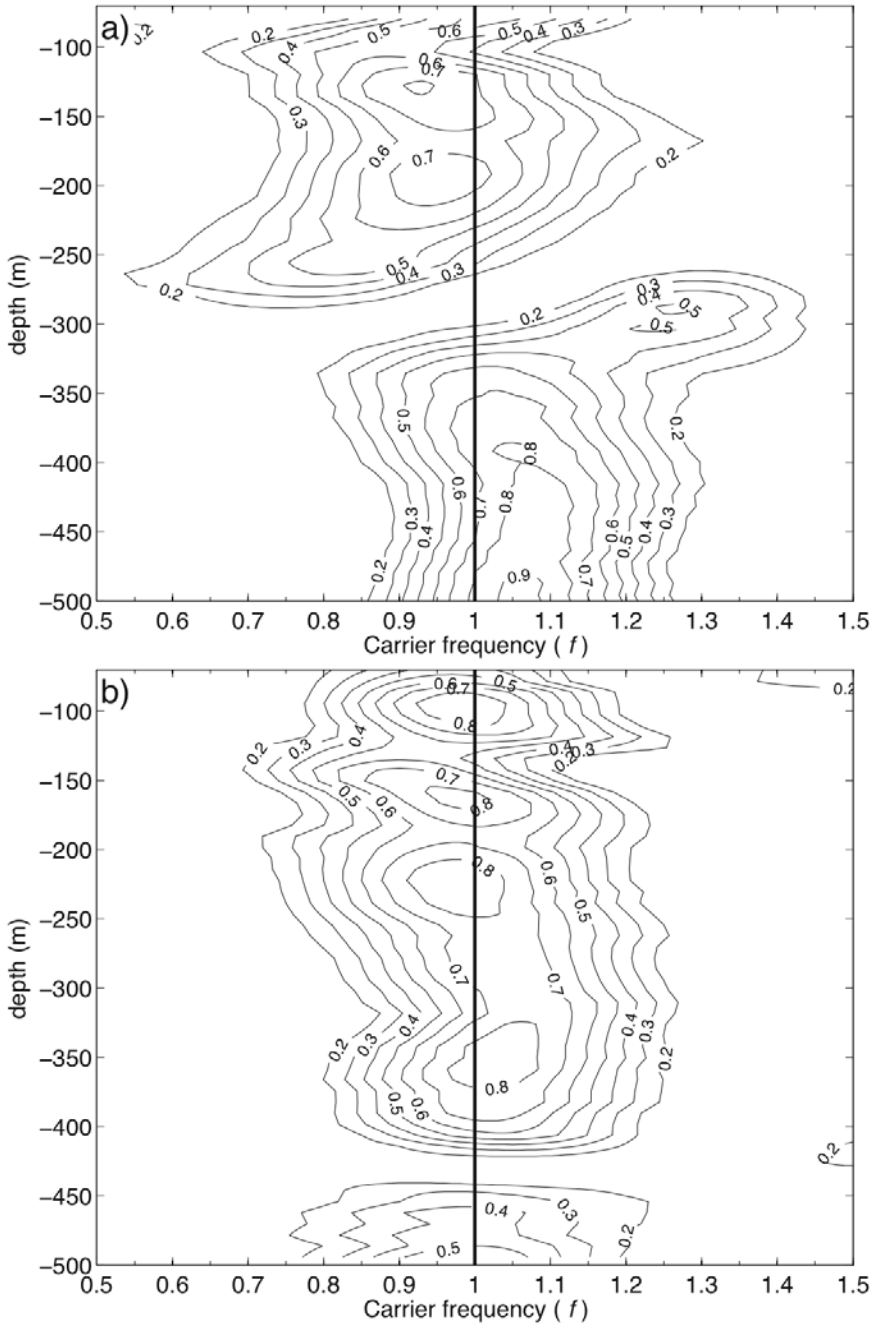

Figure 4.9: Carrier frequency of the near-inertial response inside (a) the CCE that interacted with Katrina, and (b) the LC bulge affected by Rita, based on least-square fits. Contours are the correlation coefficient *r* (Eq. 4.7) between observed (mooring data) and modeled (Eq. 4.6) perturbation velocities. Vertical line stands for the local Coriolis frequency ($f = 6.85\times10^{-5}$ s^{-1} at 27.998^{o}N) (Jaimes and Shay 2009b).

Inside the CCE, the near-inertial response to Katrina indicates two clear patterns of frequency shifting (Fig. 4.9a). In deeper waters (below 300 m) the best frequency fits occurred at higher frequencies than f, with a peak at ~1.05f. This blue-shift is in agreement with the distribution of f_e over this depth range (Fig. 4.8). By contrast, in surface waters (above 300 m), the optimal frequency fits occur at lower frequencies than f, with peak values of r (~0.70 to 0.75) at about 0.95f. This red-shift in surface waters cannot be explained by f_e, which suggest that other processes are involved. According to linear theory, in addition to f_e, the effective buoyant frequency and the vertical geostrophic shear (second and third terms in the r.h.s. of Eq. (4.4), respectively), also contribute to the intrinsic frequency, but these contributions are about two orders of magnitude smaller than f_e. However, the Doppler term $\mathbf{K} \cdot \mathbf{V}_g$ in Eq. (4.3) is of the same order than f_e. Given that, in the northern hemisphere, near-inertial oscillations rotate clockwise while $\mathbf{V}_g$ rotates anticlockwise in the CCE, the hypothesis is that the geostrophic Doppler term delays the near-inertial frequency in surfaces waters that shift the near-inertial response to sub-inertial frequencies.

In the case of the near-inertial response inside the LC bulge (Fig. 4.9b), the frequency fits are better than in the CCE above the 100-m depth level. In the upper 250 m, the fits are slightly skewed toward lower frequencies than f, and between 250 and 430 m depth there is a slight shift toward higher frequencies than f. The blue-shift in the LC is nearly homogeneous with depth in the upper 400 m, in agreement with the distribution of f_e (Fig. 4.8).

Table 4.2: Comparison of real (z_o) and stretched (z_s) depth levels at the mooring site. The unit sm stands for 'stretched' meters.

z_o [m]	0.0	70.4	102.4	150.4	198.4	254.4	302.4	350.4	398.4	454.4	494.4
z_s [sm]	0.0	103.9	188.2	276.4	351.8	438.0	507.7	576.9	644.3	722.9	778.5

4.4.4 Vertical wavenumber spectrum

Rotary spectra are computed to understand the rotational characteristics of the forced near-inertial waves in vertical wavenumber space (Gonella 1972). These vertical wavelengths were calculated with the procedure of Leaman and Sanford (1975) by: (i) removing vertical averages of the horizontal velocity components from each profile of the mooring data; (ii) time-averages of the horizontal velocity components were removed at each depth level; (iii) velocity components were WKBJ-scaled with

$$u_n(z) = u(z)/\left(\overline{N}(z)/N_o\right)^{1/2}, \tag{4.8a}$$

$$\upsilon_n(z) = \upsilon(z)/\left(\overline{N}(z)/N_o\right)^{1/2}, \tag{4.8b}$$

where u and υ are the original horizontal velocity components, u_n and υ_n are the scaled velocities, $\overline{N}(z)$ is the time averaged buoyancy frequency profile, and N_o is a reference buoyancy frequency equal to ~3 c.p.h.; (iv) vertical coordinate was stretched according to $dz_n = [\overline{N}(z)/N_o]dz$, where z is the original vertical coordinate (meters) and z_n the 'stretched' vertical coordinate (stretched meters, sm) (Table 4.2); (v) original profiles were interpolated to equally spaced z_n levels; (vi) the hourly stretched profiles were time-averaged from 5 to 7 IP for the CCE that interacted with Katrina, and from 8 to 10 IP for the LC bulge affected by Rita. The rotary spectra were independently calculated for the CCE and LC bulge.

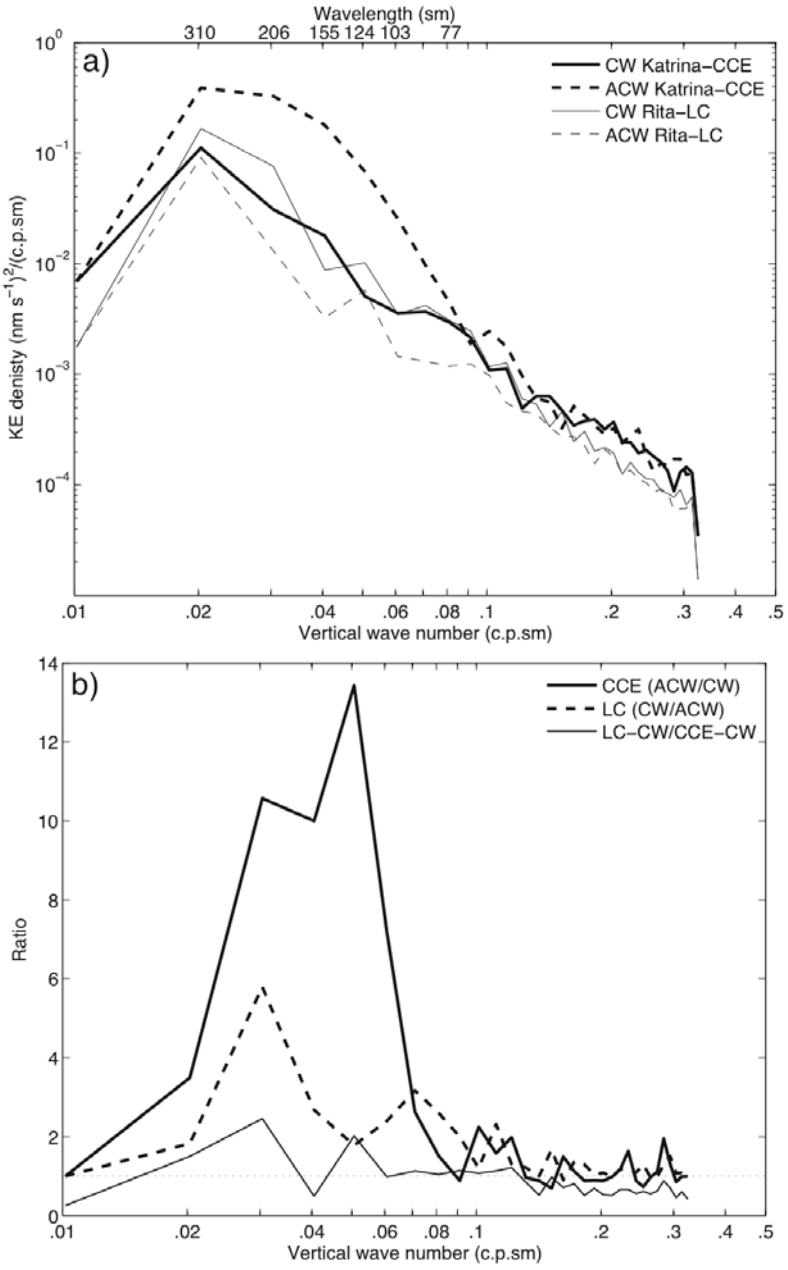

Figure 4.10: Vertical energy propagation inside the CCE that interacted with Katrina and the LC bulge affected by Rita. (a) Rotary spectra of the near-inertial velocity response inside the CCE (from 5 to 7 IP) and LC bulge (from 8 to 10 IP). The unit nm in this log-log plot stands for normalized meters and is associated with normalized velocities (Eq. 4.8), while sm is 'stretched' meters (Table 4.2), and c.p.sm is cycles per 'stretched' meter. Solid lines are for the CW component of the spectra, and dashed lines for the ACW component. (b) Ratios between different rotary spectra components (the *x*-axis in this plot is logarithmic): solid line is for the ratio ACW (dominant component) to CW energies inside CCE; dashed line is for the ratio CW (dominant component) to ACW energies inside the LC bulge; and, the thin line contrasts the CW energies from the LC bulge and CCE. The dotted line is a reference representing the ratio equal to one.

The dominance of the anticlockwise rotating (ACW) over the clockwise (CW) rotating part of the rotary spectrum is the most striking aspect of the near-inertial response inside the CCE (Fig. 4.10a,b), denoting upward energy propagation (Leaman and Sanford 1975; Leaman 1976). Inside this eddy, upgoing energy is about ten times larger than the downward energy for wavelengths from ~100 to 250 sm, and for shorter wavelengths, the spectra are nearly equally partitioned between ACW and CW components. Notice that the energy peak of the CW component is narrower and skewed toward longer wavelengths with a peak from about 200 to 300 sm. The rapid decay at larger wavelengths in both the ACW and CW spectra is an artifact, as wavelengths larger than 780 sm (~500 m, Table 4.2) were not resolved in the analysis. A region of cyclonic vorticity with more upgoing than downgoing near-inertial energy at the same wavelengths was observed in a Sargasso Sea front (Mied et al. 1986).

In the case of the LC bulge, the downward energy propagation dominates practically at all wavelengths (Fig. 4.10b), consistent with energy partitions from rotary spectra calculated from current profilers deployed in the GOM during Hurricane Gilbert (1988), that indicated that the CW rotating component dominated in 83% of the profilers, and the average ratio of CW to ACW energies was ~3.6, indicative of a preference for downward energy propagation from the wind-forced OML near-inertial currents into the thermocline (Shay and Jacob 2006). Comparison of CW energies between the LC bulge and CCE indicates that, for wavelengths from about 120 to 300 sm, downgoing energy is about two times larger inside the LC (thin line, Fig. 4.10b).

Table 4.3: Summary of vertical energy fluxes associated with the near-inertial waves induced by Katrina and Rita in the CCE and LC bulge, respectively. These numbers are integrated values of the product $E(m) \times Cg_z(m)$ (Leaman 1976), with $E(m)$ the spectral energy of the m-th wavenumber (from the rotary spectrum, Fig. 4.10a), and $Cg_z(m) \cong -2f\delta m^{-1}$ the vertical group velocity of the m-th wavenumber (Rossby and Sanford 1976), and δ is the departure from the local Coriolis frequency (+0.05 for downgoing energy, and -0.05 for upgoing energy, based on Fig. 4.9). Upgoing (downgoing) energy fluxes were calculated from the ACW (CW) components of the rotary spectrum. Values in parenthesis for the upgoing and downgoing energy fluxes represent the fraction of the total vertical energy flux for the particular geostrophic feature.

	Upgoing [$\times 10^{-2}$ W m^{-2}]	Downgoing [$\times 10^{-2}$ W m^{-2}]	CW/ACW
CCE	25.4 (82%)	-5.4 (18%)	0.2
LC	3.7 (32%)	-7.9 (68%)	2.1

In the CCE, the overall ratio of CW to ACW energies was 0.2, while in the LC bulge this ratio was 2.1 (Table 4.3). This confirms that inside the CCE only a small fraction of the KE supplied by the hurricane (~20%) is exported downward into the thermocline, and ~80% of this energy remains in upper layers where it is presumably available to increase vertical shears and induce turbulent vertical mixing and cooling, consistent with the ray tracing analysis discussed above and results of Lee and Niiler (1998). By contrast, in the LC bulge, less KE was available for vertical entrainment mixing events in upper layers, as ~70% of the wind-forced near-inertial energy was radiated into thermocline waters, similar to results by Kunze (1985, 1986).

4.4.5 Contribution to the global internal wave power

Given that not all the hurricane power injected by Katrina and Rita into the upper ocean was used to cool the OML, it is of interest to estimate the contribution to the global internal wave power from the near-inertial wave energy flux F_{iw} induced by these storms.

Table 4.4: Internal near-inertial wave energy flux F_{iw} [Eq. (4.9)] radiated into the thermocline, from mooring ADCP inside the CCE (induced by hurricane Katrina), and the LC bulge (induced by hurricane Rita). F_{iw} represents the fraction of eddy kinetic energy not used to entrain colder thermocline water into the OML (mixed layer energy sink). Cg_z is calculated from Eq. (4.5b) and parameters in Table 4.1.

	V (m s^{-1})	Cg_z (m day^{-1})	F_{iw} (W m^{-2})
CCE	0.6	8.6	1.8×10^{-2}
LC	0.3	233	12.1×10^{-2}

This flux is an energy sink of turbulent kinetic energy for the OML, and it is conventionally seen as a function of the stratification underneath the OML base (Linden 1975; Gill 1984; Nilsson 1995). Brooks (1983) estimated the vertical energy flux F_{iw} :

$$F_{iw} = Cg_z E_d , \tag{4.9}$$

where Cg_z is the vertical component of the group velocity vector [Eq. (4.5b)], and E_d is the layer kinetic energy density at the time of maximum near-inertial wave response. The layer kinetic energy density is:

$$E_d = \frac{1}{2}\rho_o V^2 ,$$

where V is the cross-track maximum near-inertial velocity response (Brooks 1983). Characteristic velocity responses inside the CCE (0.6 m s^{-1}) and the LC (0.3 m s^{-1}) were obtained from data shown in Fig. 4.2 and 4.3.

Vertical group velocities were about 9 m day^{-1} inside the CCE, and 233 m day^{-1} inside the LC bulge (Table 4.4). The corresponding near-inertial wave fluxes were between 1.8×10^{-2} and 12.1×10^{-2} W m^{-2} in the CCE and LC, respectively (cf. Table 4.3). That is, the near-inertial downward energy flux into the thermocline was significantly stronger in the LC than in the CCE.

Table 4.5: Hurricane-induced global internal near-inertial wave power for oceanic conditions similar to CCE (non parenthesis values) and LC bulge (values in parenthesis). W_i is the wave power induced by an individual storm over an arbitrary storm's wake of area $A=dxdy$. The values of the vertical energy flux F_{iw} are from Table 4.4. The global wave power W_g is calculated by assuming a global average of 67 storms per year (Emanuel 2001), that each individual storm was present during 20 days, and that the storms had similar characteristics than hurricanes Katrina or Rita. In an eddy-free ocean the global wave power should be somewhere in between the CCE and LC values.

Wake area	Wake description	$W_i = \int_x \int_y F_{iw} dydx$ [$\times 10^{10}$ W]	$W_g = W_i \times 67 \times (20/366)$ [$\times 10^{10}$ W]
200 km×200 km	area of a CCE/WCE	0.07 (0.5)	0.3 (1.8)
400 km×2000 km	average storm wake	1.4 (9.7)	5.1 (35.5)
1000 km×2000 km	Emanuel (2001)	3.6 (24.2)	13.2 (88.6)

As shown in Table 4.5, depending on the area of the hurricane's wake, and whether the near-inertial waves propagate inside positive or negative geostrophic relative vorticity features, the contribution to the global internal wave power ranges between 0.3×10^{10} to 89×10^{10} W, which is consistent with the estimate of $\sim10^{10}$ W of Nilsson (1995), and with values of 10^{11} W found by Shay and Jacob (2006) using velocity profiles in the wake of hurricane Gilbert. These results are a few orders of magnitude smaller than the value of $O(10^{15})$ W calculated by Emanuel (2001).

4.5 The critical layer in the cold core eddy

4.5.1 Amplification of near-inertial waves

From a theoretical perspective, near-inertial waves become more influenced by ambient rotation as they propagate in the direction of increasing f_e (Mooers 1975; Olbers 1981; Kunze 1985). In this context, of particular interest is to delineate the role of the

vertical distribution of f_e (Fig. 4.8) on the upgoing near-inertial energy in the CCE. Notice that in this eddy, waves traveling downward from the surface become less inertial, and so can propagate away from the cold eddy (cf. Fig. 4.6a).

Near-inertial waves propagating inside the CCE above the 250 m depth and toward the surface become more near-inertial, as they encounter a rapidly increasing f_e (Fig. 4.8). Under these circumstances, the theory predicts that the vertical wavenumber must shrink for the waves to continue satisfying their dispersion relation (Eq. 4.3). Consequently, the vertical group velocity also must diminish, becoming zero at the critical layer depth where the wave's intrinsic frequency ω_o equals f_e (Kunze 1985). To satisfy the wave action principle (Bretherton and Garrett 1969), the reduction of the vertical scale must be compensated by wave amplification in the horizontal, until a level in which vertical shears become unstable, enhancing turbulent vertical mixing at the critical depth.

The near-inertial current amplification in the CCE can be calculated with the weights [A_1, A_2] associated with the carrier frequency [Eq. (4.6)]. The weights [A_1, A_2] associated with this carrier frequency provide a proxy to the canonical amplitude of the near-inertial response $A_m = (A_u^2 + A_\upsilon^2)^{1/2}$, where $[A_u, A_\upsilon] = (A_1^2 + A_2^2)^{1/2}$, with A_u and A_v the velocity amplitudes in the cross- and along-track directions, respectively. As shown in Fig. 4.11, near-inertial amplitudes are surface-intensified in the upper 250 m of the CCE, coinciding with the increase of f_e. The maximum amplitude occurs at ~125 m depth, and above this depth, the amplitude rapidly decays about 50% over a distance of approximately 50 m. Below 300-m depth, the amplitude is slightly bottom-intensified where f_e grows weakly with depth.

For waves propagating vertically in a uniform, time-independent medium, the intrinsic frequency and vertical wavenumber are constant along a ray, i.e. $-\partial\omega_0/\partial z = 0$, and dk_z/dt = 0. However, in a nonuniformly moving medium (CCE, for instance), the intrinsic frequency ω_o varies along a ray (Bretherton and Garrett 1969), so that $dk_z/dt = \pm\partial\omega_0/\partial z$, or $d\lambda_z/dt \propto \partial\omega_0/\partial z$ for upgoing waves ($m > 0$). As shown in Fig. 4.11, the increase of ω_0 from the depth to the surface coincides with wave amplification, indicating that the reduction of the vertical wavelength is compensated by amplification of the horizontal velocity for waves propagating upward in the upper 250 m, in accord with theoretical predictions.

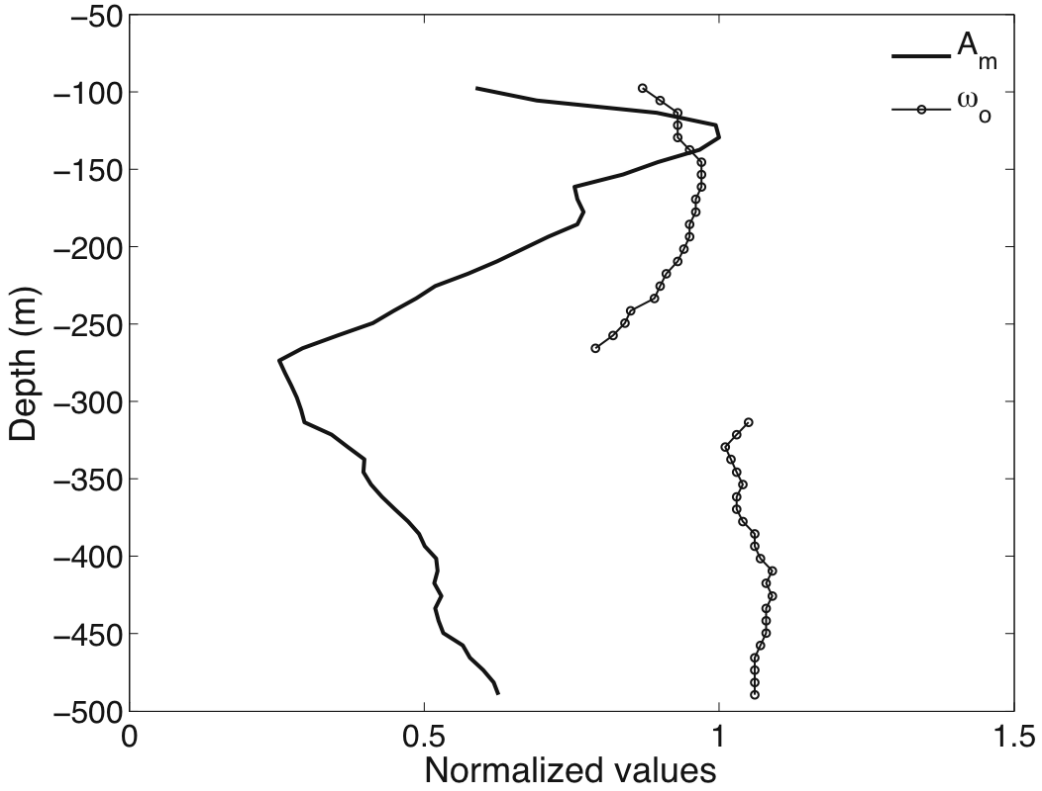

Figure 4.11: Amplitude (A_m) of near-inertial currents with the carrier frequency ω_o. A_m and ω_o are normalized by max(A_m) and f, respectively (Jaimes and Shay 2009b).

4.5.2 Relative contribution of buoyancy

In addition to the geostrophic relative vorticity, the density stratification can modulate the forced near-inertial oscillations, as variations in N cause the waves to change their horizontal kinetic energy and vertical wavenumber as they propagate vertically through the water column (Leaman and Sanford 1975). Thus, it is important to delineate the role of the vertical distribution of N on the change of amplitude of the Katrina- and Rita-forced waves as they propagated vertically inside the CCE and LC bulge, respectively. For this purpose, the original velocity data from the most western mooring were used to calculate the vertical distribution of time-averaged kinetic energy of the perturbations $\overline{K'}$. Perturbation velocities were obtained with steps (i) and (ii) of section 4.4.4 (i.e. non WKBJ-normalized velocities), by removing vertical and time averages from 5 to 8 IP, and from 7 to 10 IP, for the CCE and LC bulge, respectively. Perturbation kinetic energies K' were then calculated from these perturbation velocities at 1-hr intervals. Finally, $K'$was time-averaged over the periods described above.

In the case of the LC bulge, the $\overline{K'}$ scales with the buoyancy frequency (Fig. 4.12), indicating that in this feature background relative vorticity played a negligible role in modulating the amplitude of the near-inertial oscillations (see the nearly homogeneous vertical distribution of f_e inside the LC bulge, Fig. 4.8). However, in the CCE the behavior differs in that there is no apparent direct link between the variability in N and the amplitude of $\overline{K'}$. This supports the hypothesis that inside the CCE, the amplitude of the near-inertial oscillations was modulated by the relative vorticity of the basic state flow. In this eddy, there is a reduced level of $\overline{K'}$ at the depth of maximum buoyancy frequency (~100 m depth). This reduction of wave activity is associated with the

maximum in vertical shear instability, which dampens near-inertial energy of upgoing waves, via increased turbulent vertical mixing (critical layer).

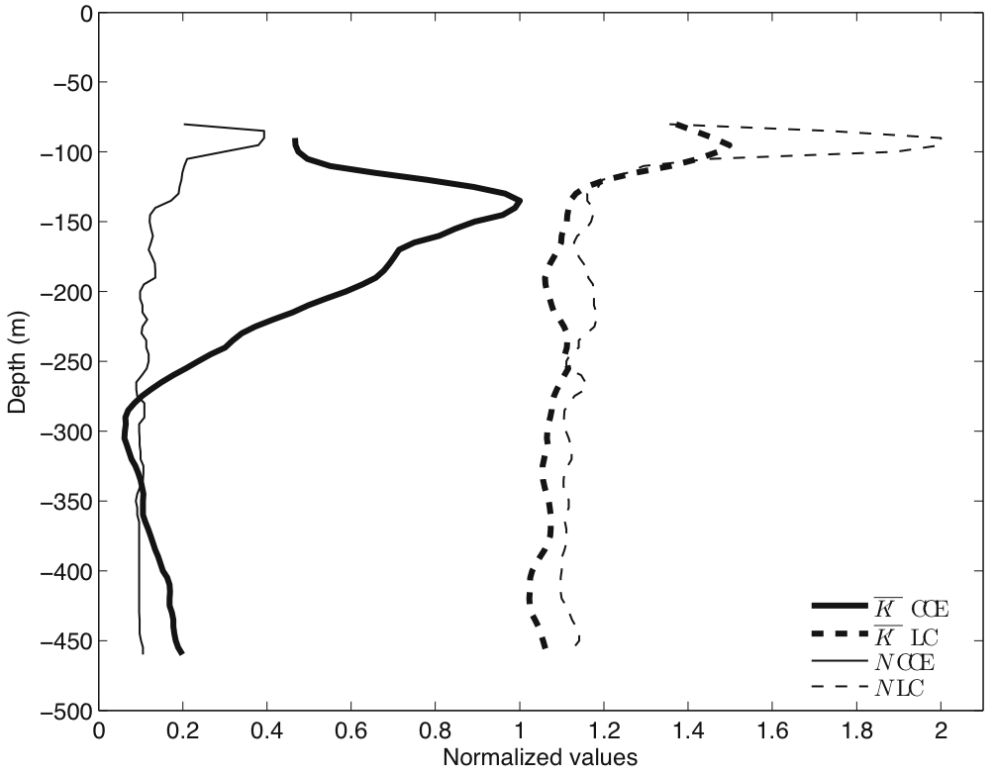

Figure 4.12: Vertical variability of the buoyancy frequency N and time-averaged perturbation kinetic energy $\overline{K'}$, inside the CCE and LC bulge. For comparative purpose, the two profiles of N are normalized by max(N) from the LC bulge, and the two profiles of $\overline{K'}$ are normalized by max($\overline{K'}$) from the CCE. For clarity in the presentation, the normalized values of the LC bulge are shifted one unit to the right.

4.5.3 Surface maximum of cyclonic relative vorticity

To explain the surface intensification of ζ_g inside the CCE, consider Fig. 4.7, which indicates two periods of cyclonic ζ_g at the mooring. The first period, corresponding to the CCE that interacted with Katrina, exhibits a baroclinic current structure between about 5 to 12 IP, with a strong vertical gradient from ~100 to 150 m depth. Over this 50-m depth interval, ζ_g intensifies from 0.04f to 0.1f in the upward

direction. This reveals that during the forced stage, the input of cyclonic vorticity from Katrina's wind stress strengthened the cyclonic circulation in the upper layers of the CCE, which had profound effects on the amplification of upward propagating near-inertial waves during the relaxation stage. That is, wind stress curl provided optimal conditions via increased f_e for a positive feedback mechanism on the ocean for increasing vertical shears and turbulent mixing cooling.

4.5.4 Origin of upgoing near-inertial waves

The direct generation at the OML of downward propagating near-inertial waves by a fast moving TC ($Fr > 1$, Geisler 1970) is generally well understood. However, near-inertial wave generation in the ocean's interior associated with the TC passage has not been reported. In the previous section, we discussed such waves, and their effects on vertical mixing and subsequent upper ocean cooling. The observations here suggest that these upward-propagating waves may have been generated by geostrophic adjustment, in analogy with processes studied in other context (Rossby 1938; Gill 1982). The focus is on the CCE affected by Katrina, as this fast moving storm produced a stronger near-inertial response of upward propagating waves in a water column extending from about 120 to 250 m depth levels (Fig. 4.2a).

In analogy to the upwelling/downwelling regimes induced by Rita over the LC system (section 3.3), the scenario is that during Katrina passage, wind-forced surface waters diverge and denser water is upwelled along the track. This oceanic flow is enhanced when wind stress is in the direction of the cyclonically rotating geostrophic flow. By contrast, there is horizontal convergence and downwelling of lighter water in

regions where the wind stress is against $\mathbf{V}_g$. Density anomalies associated with these contrasting upwelling/downwelling regimes extend to the thermocline and had to be removed by horizontal mass redistribution.

As shown in Fig. 4.13, the reduction of background kinetic energy $\overline{K}$ (crests in isolines of $\overline{K}$) between 5 to 9 IP (and between ~150 to 250-m depth levels) coincided with radiation of near-inertial wave energy K'. From 9 to 11 IP, the amplitude of the crests in $\overline{K}$ was reduced at the same time that the production of K' was dampened. Notice the tendency for $\overline{K}$ to be homogenized in the vertical as time evolves (i.e. reduced energy levels at the surface, and increased energy at depth), which is an indication that the subsurface horizontal pressure gradients associated with the hurricane-induced vorticity and density anomalies were removed via radiation of near-inertial internal waves. Notice that this simultaneous increase of K' and decrease of $\overline{K}$ occur in a water column (~100 to 200 m depth) below the OML base that extended at about 60 m depth.

4.6 Summary and concluding remarks

Katrina and Rita moved over the LC system as major hurricanes, and induced contrasting OML cooling levels depending on the distribution of geostrophic relative vorticity ζ_g in the upper ocean. Cooling was increased and reduced over cyclonic and anticyclonic ζ_g, respectively. To explain this differentiated cooling, observational data are used here to investigate the three-dimensional near-inertial wave wake induced by both TCs inside cyclonic and anticyclonic geostrophic features.

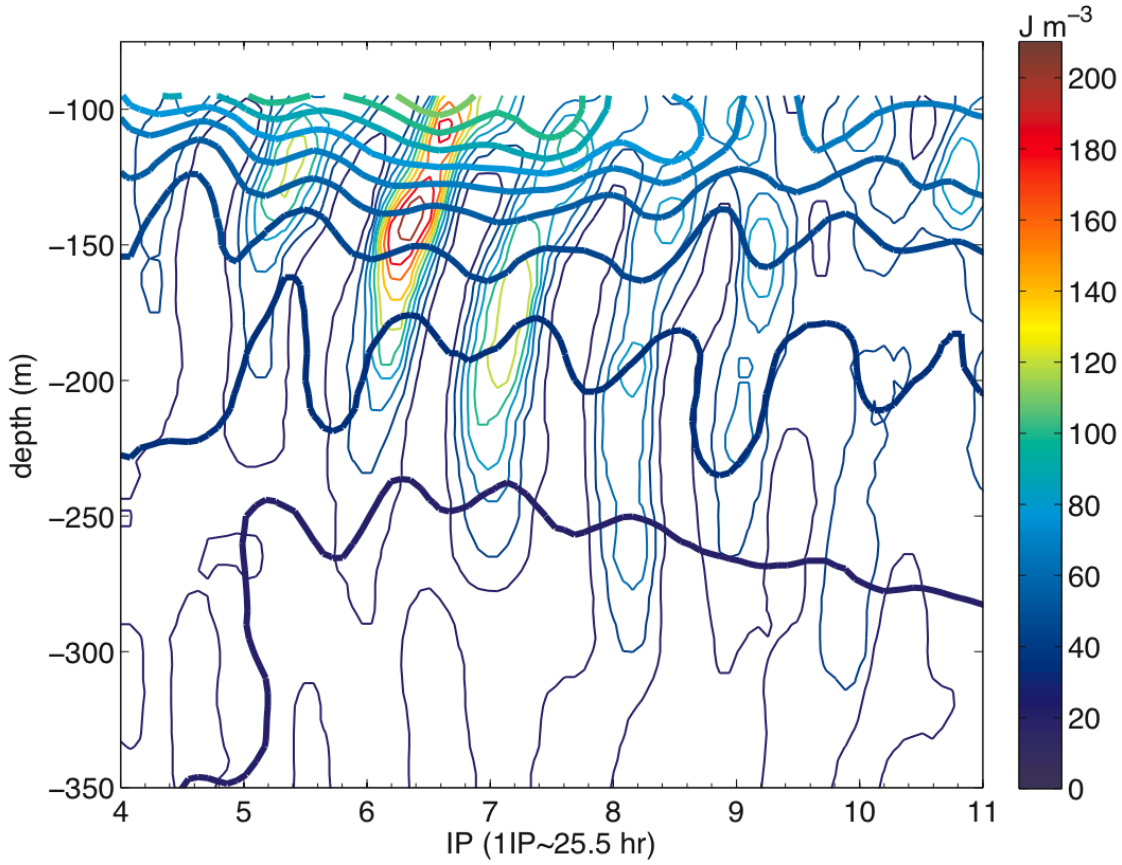

Figure 4.13: Evolution of the kinetic energy of the background flow $\overline{K}$ (bold contours) and the near-inertial perturbations K' (thin contours) inside the CCE, from ADCP mooring velocities. $\overline{K}$ was calculated from 5-IP running means of cross- and along-track velocity components ($\overline{u}$ and $\overline{\upsilon}$, respectively). K' was calculated from perturbation velocities u' and υ', where $u' = u - \overline{u}$, and $\upsilon' = \upsilon - \overline{\upsilon}$, with u and υ instantaneous WKBJ-scaled velocities (Jaimes and Shay 2009b).

Ray-tracing techniques in realistic geostrophic flow predicted that forced near-inertial waves initially moving downward from the OML are horizontally trapped in regions of negative ζ_g, where radiation into the thermocline dominates. These anticyclonic-rotating regimes coincided with distribution of reduced OML cooling, which suggests that rapid downward dispersion of near-inertial energy reduces vertical shears in upper layers of anticyclonic features, as observed in other oceanic regions (e.g. Kunze and Sanford 1984; Kunze 1986). By contrast, downward propagating near-inertial waves

are stalled in upper layers of cyclonic circulations (cf. Lee and Niiler 1998), where vertical shears and entrainment cooling are increased. Overall, the vertical mixing induced by Katrina and Rita was confined to the near-surface regime.

Upgoing energy dominates wave vertical dispersion inside the CCE that interacted with Katrina, in agreement with dominant upgoing near-inertial energy observed in a cyclonic eddy in the Sargasso Sea front (Mied et al. 1986). In the CCE, amplification of these upward propagating waves produced a critical layer (increased turbulent mixing) about 50 m underneath the OML base. Rather than with the buoyancy frequency *N*, these upgoing waves amplify as function of $f_e = f + \zeta_g / 2$.

Vertical wave energy fluxes of O(10^{10}) W were 4 to 10 times larger than in unforced cases (Leaman and Sanford 1975), but were comparable to those found in frontal regimes (Kunze and Sanford 1984) and during hurricane Gilbert (Shay and Jacob 2006). Downward vertical radiation of near-inertial wave energy was significantly stronger inside the LC bulge (12.1×10^{-2} W m^{-2}) compared to that in the CCE (1.8×10^{-2} W m^{-2}). Evidence of internal motions beyond 1.5*f* was found neither in the upper 500 m of the CCE nor in the LC bulge, as suggested by numerical studies that have found a peak at 2*f* for other regions (e.g. Niwa and Hibiya 1997; Danioux and Klein 2008).

Chapter 5

Numerical Studies

The observational and theoretical evidence presented in Chapter 3 and in Jaimes and Shay (2009a) underscore the impact of the underlying geostrophic oceanic eddies on the TC-forced upwelling velocity. This upper ocean response was shown to be a function of the background flow's rotational characteristics. In quest of a generalized result, a series of numerical experiments is conducted, in which the development of the upwelling velocity is analyzed as function of a *Ro* range characteristic of the Gulf of Mexico's geostrophic features.

In Chapter 4 and in Jaimes and Shay (2009b), it was shown that ζ_g plays a central role during the dispersion of TC-forced near-inertial waves. Contrasting dispersion patterns emerged as a function of ζ_g that presumably affected the distribution of momentum, vertical shear, and mixing through the water column. Moreover, near-inertial waves amplified as they encountered increasing values of f_e (a function of ζ_g) during upward propagation through a CCE. These waves eventually became dynamically unstable, where wave breaking occurred that produced vertical mixing. As discussed previously by Shay et al. (1989, 1998), shear instability of forced near-inertial waves is associated with the third and fourth forced baroclinic modes. Therefore the question is

whether the rotational constraints imposed by the geostrophic eddies can impact mode separation in the wake of TCs. Gill (1984) investigated the role of the OML thickness and planetary β during mode separation. Here, the effects of *Ro* on the wake of TCs are considered.

Another aspect considered here is the advection of the temperature anomaly produced by TCs over the upper ocean, presumably associated with the westward-propagating geostrophic eddies. This anomaly typically occurs on the right side of the TC track, over a distance of $O(10^3)$ km. However, after the passage of TCs Ivan (Walker et al. 2005), and Katrina and Rita (section 4.3.3; Jaimes and Shay 2009b), the dominant temperature anomaly occurred on the left side of the storm's track. In this context, the hypothesis that the internal wave wake of a TC is transported by the geostrophic eddies, is tested here. The model approach is:

- An isopycnic model (MICOM) is used to reduce spurious vertical mixing, where the top layer, which is non-isopycnic, represents the OML.
- The contribution from buoyancy fluxes across the air-sea interface to the vertical entrainment velocity is comparable to the contribution from wind erosion during the forced stage. However, in the present treatment, buoyancy fluxes are ignored both in the density equation and in the TKE equation (for consistency) because the interest is on the OML response due to internal oceanic processes (adiabatic ocean), which have been proven to drive most of the TC-induced OML cooling.
- The turbulence closure for the OML only considers: (i) instantaneous wind erosion driven by the third power of the frictional velocity w_* (Kraus and Turner

1967, or KT); and, (ii) shear-driven entrainment at the OML base and in the stratified ocean below (Price et al. 1986, or PWP).

- An *f*-plane is used to prevent self-propagation of the geostrophic eddies, which facilitates analyzing the near-inertial response at fixed points inside the stationary eddies. Notice that this approach cancels horizontal dispersion of near-inertial waves by meridional gradients in planetary vorticity (Gill 1984). Any resulting horizontal wave dispersion is driven by ζ_g.
- Idealized geostrophic vortices (WCEs and CCEs) are initialized from an analytical model and the observed density structure from the pre-Rita flight. These vortices are initially isolated (the area integral of the relative vorticity vanishes at all depths, i.e. the total circulation is initially zero in each layer), and they satisfy the quasi-geostrophic (QG) approximation.

5.1 Ocean model

In MICOM, the ocean interior is represented as a stack of density (isopycnic) layers governed by equations resembling shallow-water equations. The model consists of four prognostic equations for the horizontal velocity vector, mass continuity or layer thickness tendency, and two conservative equations for salt and heat. A non-isopycnic mixed layer forms the top layer of the model (Bleck and Chassignet 1994).

Isopycnic coordinate models suppress the diapycnal component of numerically caused dispersion of material and thermodynamic properties. This allows MICOM to preserve its water mass characteristics and prevents warming of deep water masses that

has been shown to occur in models framed in Cartesian coordinates (Chassignet et al. 1996; Griffies at al. 2000).

5.1.1 Numerical domain

The idealized computational domain is a 2000 km square ocean with an initially circular QG vortex (WCE or CCE) of ~150 to 300 km in diameter located at the center of the domain (Fig 5.1). The vertical extension of the vortex is 950 m that is representative of GOM's WCEs and CCEs (Table 1.1). The vortex is located on top of an initially quiescent isopycnal layer of 4000 m in thickness. The bottom is flat, and lateral boundary conditions are closed. The central latitude of the computational domain is 26.9^{o}N. This latitude was chosen to reproduce a near-inertial response closer to that observed at the latitude of the MMS mooring array. The horizontal grid resolution is 10 km, which allows explicitly resolving horizontal wavelengths larger than 20 km in the ocean model.

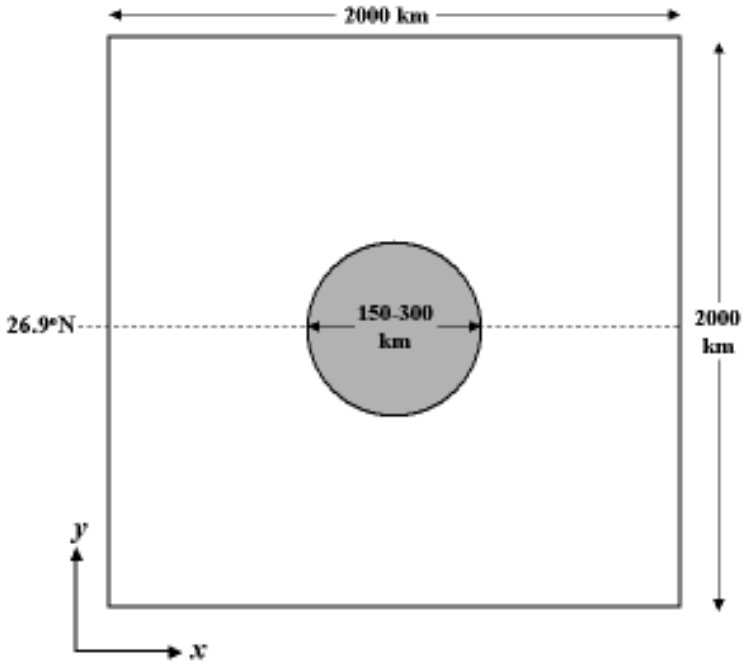

Figure 5.1: Dimensions of the computational domain.

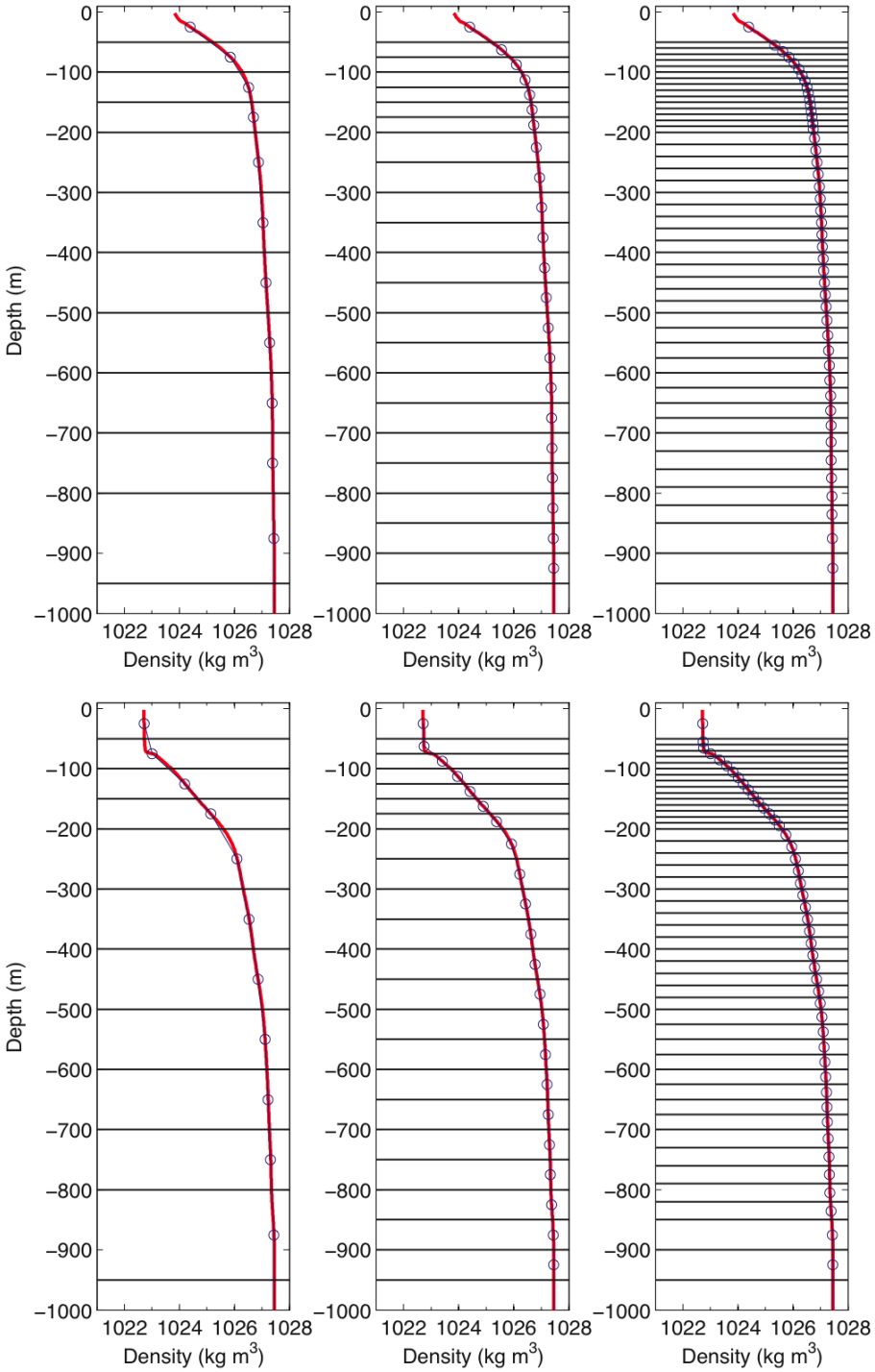

Figure 5.2: Model isopycnic layers: 12, 23, and 47, from left to right panels. Upper (lower) panels are for CCEs (WCEs). The circles represent the model density, and the red line is the observed profile (smoothed via polynomial fit). The horizontal lines represent the initial layer thickness outside the QG vortex. The top layer is the OML, and the bottom layer is not shown.

Three vertical resolutions are used: 12, 23, and 47 isopycnic layers (Fig. 5.2). In every case, the model's top layer represents the OML. The initial OML thickness is the same for every vertical resolution, and it is determined by the analytical model (section 5.2.2) as a function of the radius of the vortex, the target maximum azimuthal velocity, and the density profiles from pre-Rita observational data. Experiments with higher vertical resolution improve the representation of the stratified water underneath the OML, and so OML cooling, and vertical dispersion of near-inertial energy (section 5.7). The results presented here are from the 47 isopycnic layers experiments, which allows the model to explicitly resolve vertical wavelengths of 20 m and larger in the stratified ocean below the OML. The vertical resolution (10 m) used to reproduce these vertical wavelengths is closer to the vertical sampling grid used in the MMS moorings (~8 m).

5.1.2 Analytical model

The model vortex is constructed by introducing a potential vorticity anomaly (PVA) in a stack of initially unperturbed isopycnic layers. In the absence of forcing and dissipation, for each isopycnic layer, potential vorticity ($\mathrm{PV} = (\zeta + f)/h_k$) is conserved for each particle of the flow (Ertel 1942). The layer PVA is the departure from the ambient potential vorticity, and is defined by (Morel and McWilliams 2001; Morel and Thomas 2009):

$$\mathrm{PVA_k} = H_k\left(\frac{\zeta + f}{h_k} - \frac{f}{H_k}\right)$$

$$= \frac{H_k}{h_k}\left[\zeta - \frac{f(h_k - H_k)}{H_k}\right],$$

where k is a layer index, f / H_k is the ambient potential vorticity on the assumed f-plane, h_k is instantaneous layer thickness, and H_k is constant and represents the unperturbed layer thickness. PVA has the same properties of Lagrangian conservation as PV, has the dimensions of a vorticity and its value at rest is zero, which makes it easier to analyze (Morel and Thomas 2009).

An initial PVA profile is defined so that it satisfies both the QG approximation, and the condition that the vortex is isolated (the area integral of the relative vorticity ζ vanishes at all depths, Flierl 1987). In the case of the Gulf's WCEs and CCEs, these conditions are fulfilled by using a continuous-power exponential radial profile and annular shielding in the PVA for the isopycnic layers above the 700-m depth (Chérubin et al. 2006):

$$\mathrm{PVA}_k = \Delta Q_k \left[1 - \frac{\alpha}{2} \left(\frac{r}{R} \right)^{\alpha} \right] exp \left[- \left(\frac{r}{R} \right)^{\alpha} \right], \tag{5.1}$$

and a power exponential radial profile for isopycnic layers extending between the 700 m and 950 m depth where the annular shielding vanishes (according to GOM's WCEs and CCEs from MICOM simulations):

$$\mathrm{PVA}_k = \Delta Q_k \, exp \left[- \left(\frac{r}{R} \right)^{\alpha} \right]. \tag{5.2}$$

where $\mathrm{PVA}_k = 0$ in the bottom isopycnic layer, ΔQ_k is the maximum PVA in each layer, R is the vortex radius, r the radial distance from the vortex's center, and the parameter α determines the width of the vortex shield, that is, the horizontal shear at the vortex boundaries. These profiles ensure that the total circulation is zero for any α in each layer (Carton and Legras 1994). For fixed α and R, ΔQ_k is determined so that the set of

equations (5.1)–(5.2) reproduces the maximum vortex azimuthal speed observed in WCEs and CCEs. The background stratification in the idealized vortex is defined from the density field derived from pre-Rita observational data.

5.1.3 Wind forcing

To keep the experimentation both as simple and realistic as possible, the ocean model is forced with an idealized wind field derived from the NOAA/HRD H*Wind product (http://www.aoml.noaa.gov/hrd/data_sub/wind.html). The wind field of hurricane Katrina at maximum intensity over the LC system is used (2230 UTC August 28, 2005). Based on this snapshot, a constant wind stress field was derived using a drag coefficient C_d computed from the Large and Pond (1981) relationship, but capped at a maximum value of 2.6×10^{-3} based on recent results indicating a saturation value of C_d between 27 to 35 m s^{-1} wind speeds (Powell et al. 2003; Donelan et al. 2004; Shay and Jacob 2006; Jarosz et al. 2007). The saturation level is set at a wind speed of 27 m s^{-1}.

The storm moves over the computational domain along a straight track at an angle of 45^{o} respect to north (NW orientation, Fig. 5.3). Notice that Katrina and Rita propagated at an angle of 33.7^{o} and 63.4^{o} from true north in the LC System, respectively. By using a constant translation speed of hurricane Katrina of 6.3 m s^{-1} (Table 3.1), wind stress fields were constructed at 30-min intervals along the storm track. Linear interpolation from these 30-min wind fields is used to integrate the model every baroclinic time step (180 s) at each grid point.

5.1.4 Experiments

Based on the observed characteristics of the GOM's WCEs and CCEs (Table 1.1), four prototype QG vortexes are reproduced (Table 5.1 and Figure 5.4): WCE1 (*Ro*=0.06), WCE2 (*Ro*=0.08), CCE1 (*Ro*=0.06), and CCE2 (*Ro*=0.08), where *Ro* is the Rossby number. These vortices are initialized in model runs with several background stratifications, vertical grid resolutions, and turbulence closures for the OML, as summarized in Table 5.2.

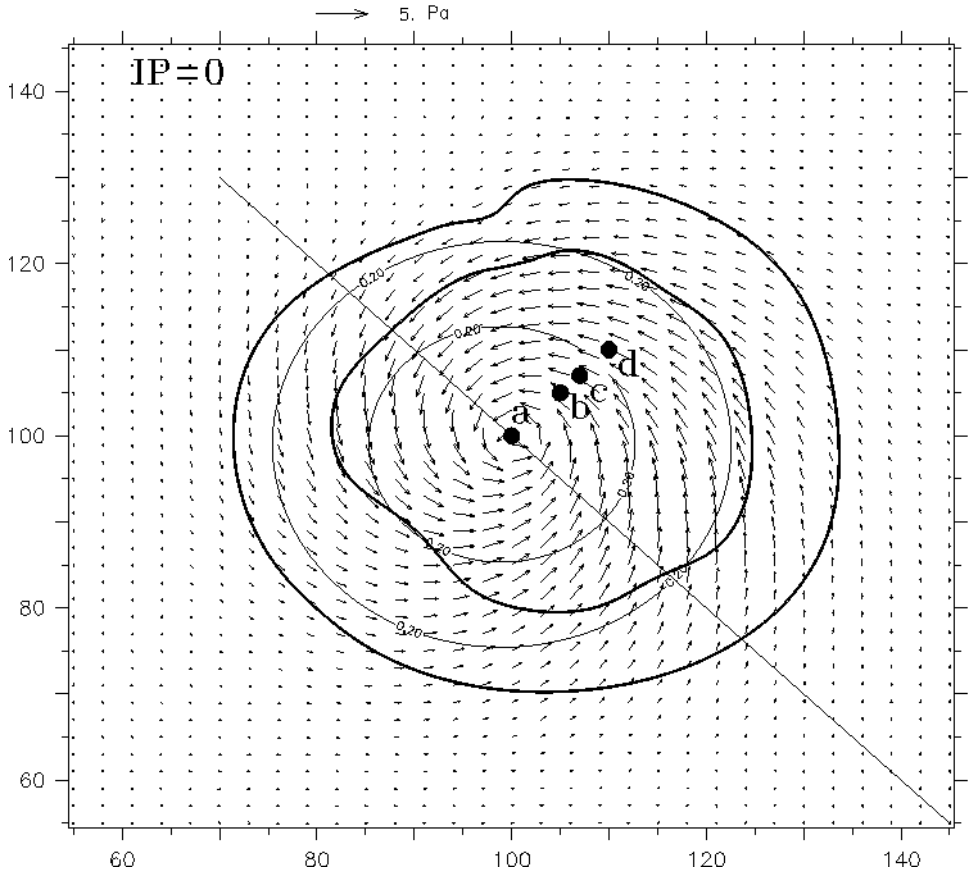

Figure 5.3: Constant wind field used to force the ocean model (from the H*Wind product). External and inner bold contours are for standard 10-m wind speed at tropical storm winds (20 m s^{-1}) and winds at saturation level (27 m s^{-1}), respectively. Vectors are wind stress calculated with a drag coefficient capped at saturation level. The straight line is the storm track. The large and small thin circles are 0.2 m s^{-1} contours of pre-storm OML currents for model WCEs and CCEs, respectively. IP stands for inertial period. Black dots are model moorings on the cross-track direction.

Table 5.1: Characteristics of modeled QG vortex (cf. Table 1.1).

Parameter	WCE1	WCE2	CCE1	CCE2
U [m s^{-1}]	0.95	1.5	0.6	0.8
L [km]	250	300	150	150
OML [m]	~70	~80	~30	~25
Ro (U/f L)	0.06	0.08	0.06	0.08

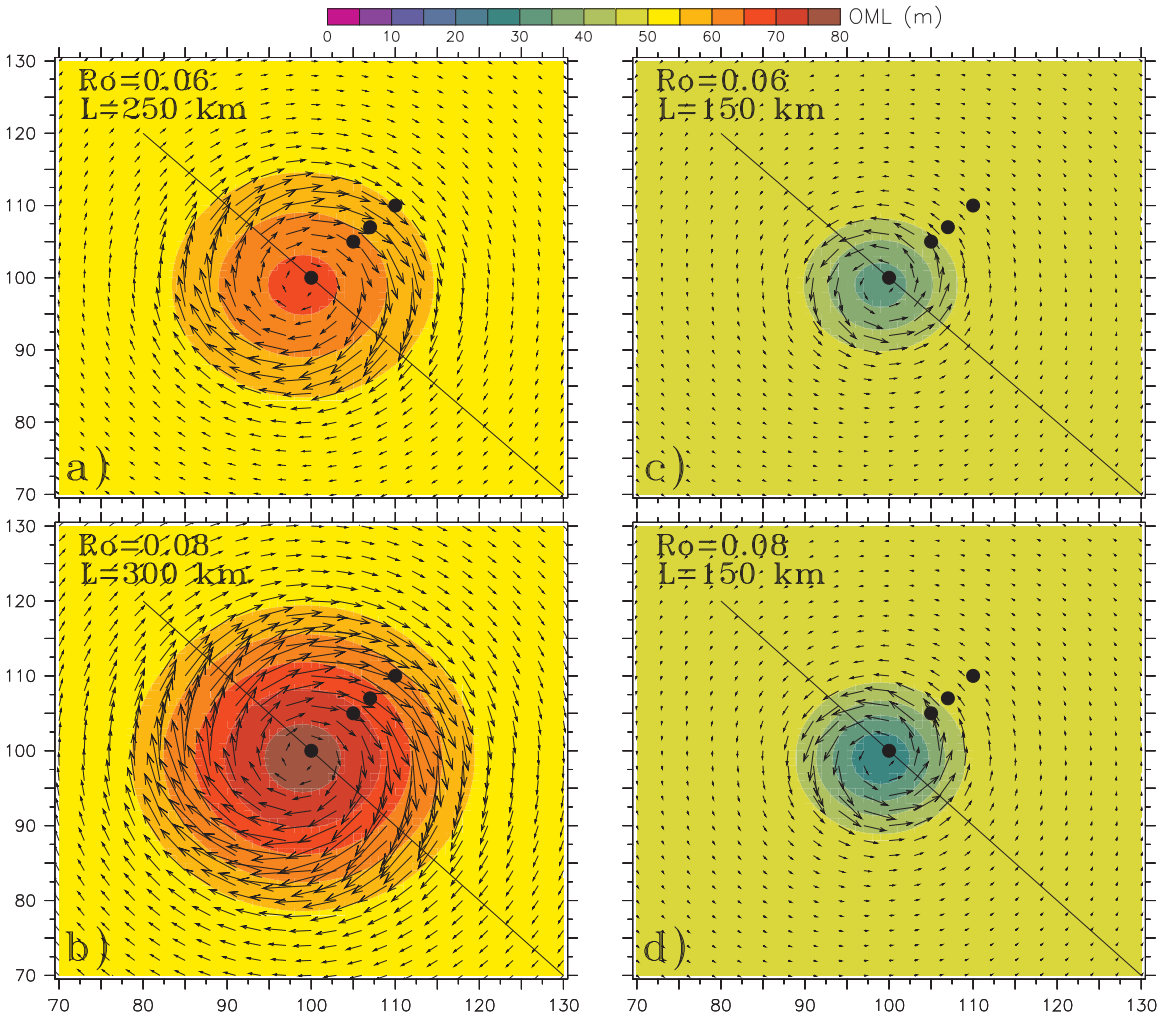

Figure 5.4: Initial conditions of the four types of model vortex. Vectors are the initial OML geostrophic currents. The black line is the storm track. L is the initial vortex's radius. Black dots are model moorings on the cross-track direction.

Table 5.2: List of experiments. The symbol ρ indicates the type of density field used to initialize the ocean model. KT and PWP stand for the Kraus-Turner and Price-Weller-Pinkel turbulence closures for the OML (section 5.4.1), respectively. Beta indicates β-plane. Control experiments are in italic bold, and changed parameters in bold. *Rc* is the critical limit of the gradient Richardson number. *K* is the number of isopycnic layers, and ΔQ_k is the maximum PVA.

WCE											
Experiment	*K*	ΔQ_k s^{-1}	Eddy	ρ	*U* m s^{-1}	*L* km	*Ro*	KT	PWP	*Rc*	Beta s^{-1} m^{-1}
wce1_01	***47***	***-5.77e-5***	***WCE1***	***wce***	***0.95***	***250***	***0.06***	**–**	**–**	**–**	***0***
wce1_02	**12**	-5.80e-5	WCE1	wce	0.95	250	0.06	**–**	**–**	**–**	0
wce1_03	**23**	-5.77e-5	WCE1	wce	0.95	250	0.06	**–**	**–**	**–**	0
wce1_04	47	-6.50e-5	WCE1	**gcw**	0.95	250	0.06	**–**	**–**	**–**	0
wce1_05	47	-5.77e-5	WCE1	wce	0.95	250	0.06	**yes**	**–**	**–**	0
wce1_06	47	-5.77e-5	WCE1	wce	0.95	250	0.06	**yes**	**yes**	**1**	0
wce1_07	47	-5.77e-5	WCE1	wce	0.95	250	0.06	**yes**	**yes**	**0.65**	0
wce2_01	47	-8.50e-5	WCE2	wce	1.50	300	**0.08**	**–**	**–**	**–**	0
wce2_02	47	-8.50e-5	WCE2	wce	1.50	300	**0.08**	**yes**	**–**	**–**	0
wce2_03	47	-8.50e-5	WCE2	wce	1.50	300	**0.08**	**yes**	**yes**	**1**	0

GCW											
Experiment	*K*	ΔQ_k	Eddy	ρ	*U*	*L*	*Ro*	KT	PWP	*Rc*	Beta
gcw1_01	***47***	***0***	**–**	***gcw***	***0***	***0***	***0***	**–**	**–**	**–**	***0***
gcw1_02	47	0	**–**	gcw	0	0	0	**yes**	**–**	**–**	0
gcw1_03	47	0	**–**	gcw	0	0	0	**yes**	**yes**	**1**	0

CCE											
Experiment	*K*	ΔQ_k	Eddy	ρ	*U*	*L*	*Ro*	KT	PWP	*Rc*	Beta
cce1_01	***47***	***6.05e-5***	***CCE1***	***cce***	***0.6***	***150***	***0.06***	**–**	**–**	**–**	***0***
cce1_02	**12**	6.10e-5	CCE1	cce	0.6	150	0.06	**–**	**–**	**–**	0
cce1_03	**23**	6.10e-5	CCE1	cce	0.6	150	0.06	**–**	**–**	**–**	0
cce1_04	47	5.27e-5	CCE1	**gcw**	0.6	150	0.06	**–**	**–**	**–**	0
cce1_05	47	6.05e-5	CCE1	cce	0.6	150	0.06	**yes**	**–**	**–**	0
cce1_06	47	6.05e-5	CCE1	cce	0.6	150	0.06	**yes**	**yes**	**1**	0
cce1_07	47	6.05e-5	CCE1	cce	0.6	150	0.06	**yes**	**yes**	**1**	**2.04×10^{-11}**
cce2_01	47	8.17e-5	CCE2	cce	0.8	150	**0.08**	**–**	**–**	**–**	0
cce2_02	47	8.17e-5	CCE2	cce	0.8	150	**0.08**	**yes**	**–**	**–**	0
cce2_03	47	8.17e-5	CCE2	cce	0.8	150	**0.08**	**yes**	**yes**	**1**	0
cce2_04	47	8.17e-5	CCE2	cce	0.8	150	**0.08**	**yes**	**yes**	**1**	**2.04×10^{-11}**
cce2_05	47	8.17e-5	CCE2	cce	0.8	150	**0.08**	**yes**	**yes**	**0.65**	0
cce2_06	47	8.17e-5	CCE2	cce	0.8	150	**0.08**	**–**	**–**	**–**	**2.04×10^{-11}**

5.2 Hurricane-induced upwelling in a quasi-geostrophic vortex

Under quiescent ocean conditions, the hurricane wind stress accelerates OML currents and displaces central waters from the storm center. Upwelling of cold thermocline water compensates this horizontal flow divergence. The region of maximum upwelling is confined to within twice the radius of maximum wind stress. The horizontal divergence produces a shallow OML under the storm's center, and a deeper OML outside the center (O'Brien and Reid 1967; O'Brien 1967). During the initial stage of the upwelling development, the wind-driven currents move in the direction of the wind stress. Subsequently, the Earth's rotation and friction act together to create the Ekman spiral and, in the northern hemisphere, the net mass transport is at about 90^{o} to the right of the wind stress.

The Ekman current that one could expect from a hurricane similar to Katrina (at maximum category 5 intensity) over GCW (eddy-free ocean) is ~0.7 m s^{-1}, which is comparable to OML geostrophic currents in CCEs, and is smaller than OML geostrophic currents in WCEs and the LC (1 to 2 m s^{-1}). Therefore, under strong geostrophic flow conditions there is no physical reason to expect a net Ekman current to the right of the wind stress, because before being influenced by the Earth's rotation, the wind-driven frictional velocity is instantaneously influenced by the strong OML geostrophic currents and their vorticity. The observational and theoretical evidence presented in section 3.3 suggests that the upwelling response is a function of the underlying OML geostrophic flow. This should be an expected result, because the wind stress and OML geostrophic currents are vectors that interact with each other. Notice that the r.h.s. term of Eq. (3.1) resembles the classical Ekman pumping. However, it is not associated with the wind curl,

but with the curl of the wind-driven acceleration along isopycnal surfaces when the vertical position of these surfaces varies in geostrophically balanced features.

To elaborate more on the hypothesis of an upwelling response influenced by the underlying geostrophic flow, a series of numerical experiments are conducted where a hurricane wind stress is applied onto WCEs, CCEs, and quiescent ocean conditions (GCW). The initial approach is to neglect vertical entrainment velocities across the OML base (no turbulence closure for the OML), so that changes in the thickness of this layer are produced only by horizontal divergence of wind-driven currents. Mathematically, this assumption is represented as following. For rather direct physical insight, the discussion focuses on OML bulk models, which are based on the density and momentum equations, given respectively by,

$$\frac{\partial \rho}{\partial t} = \frac{B}{\rho_0 g h} + \frac{\delta \rho}{h}\frac{\partial h}{\partial t}, \tag{5.3}$$

and

$$\frac{\partial \mathbf{v}}{\partial t} = -\mathbf{k}\cdot\left(f \times \mathbf{v}\right) + \frac{\tau}{h\rho_0} + \frac{\delta \mathbf{v}}{h}\frac{\partial h}{\partial t}, \tag{5.4}$$

where the air-sea buoyancy flux is $B = g\rho_0\left[\alpha Q + \beta S\left(E - P\right)\right]$, $E - P$ is evaporation minus precipitation, τ is the wind stress or a parameterization of the turbulent Reynolds stress ($\tau = \rho_a u_*^2$, ρ_a is air density and u_* the surface frictional velocity), h is the OML thickness, and the rest of the notation is conventional. Notice that the first term on the right hand side of Eq. (5.3) is ignored in the present treatment. The additional equation to close the system is (Niiler and Kraus 1975):

$$\frac{\partial h}{\partial t} = -\nabla\cdot\left(\mathbf{v}h\right) - w_e, \tag{5.5}$$

where w_e is the vertical entrainment velocity to be discussed in section 5.3, but neglected here. The OML thickness therefore is governed by divergence:

$$\frac{\partial h}{\partial t} = -\nabla \cdot (\mathbf{v}h), \tag{5.6}$$

where τ is the only source term according with Eq. (5.4).

As shown in Fig. 5.5, for the same wind forcing, the wind-driven horizontal current divergence under the storm's eye is a function of the underlying geostrophic flow, consistent with direct observations (Fig. 3.3) and theoretical predictions (Fig. 3.4). Notice that *Ro* has a negligible influence on the upwelling response during the first quarter of the IP (forced stage, or the short stage when the storm is overhead), and becomes more important afterwards (relaxation stage), impacting the near-inertial pumping and the coupling of the OML with the thermocline. In the vortex-free case (GCW), the amplitude of the upwelling response exhibits intermediate levels, compared with WCES and CCEs.

Outside the QG vortex, the vertical velocity response reproduces the classical pattern, where the region of minimum OML thickness extends under the storm's eye and within $2R_{max}$, and the OML is deeper outside this region (Fig. 5.6). The spatial distribution of upwelling/downwelling regimes inside the vortices does not change significantly by varying the distance from the storm track to the vortex's center. A dipolar distribution of vertical velocity emerges in the interior region, for both WCEs and CCEs. Regions of maximum upwelling/downwelling extend along streamlines of maximum azimuthal geostrophic velocity, for both WCEs and CCEs. By shifting the storm track westward, these regions of maximum upwelling/downwelling move radially toward more energetic geostrophic streamlines, as the inner vortex region becomes influenced by stronger winds (compare regions of maximum downwelling in Fig. 5.6d, e

and f at the second mooring from left to right). In terms of horizontal extension, upwelling (downwelling) regimes predominate inside CCEs (WCEs). However, the confined counterpart vertical velocity is stronger, and the area integral of the dipolar vertical velocity nearly vanishes in the OML, which satisfy mass conservation principles in the vortex's interior. The increase and reduction of OML thickness during the forced stage is about 16 m in WCE1 and CCE2, respectively.

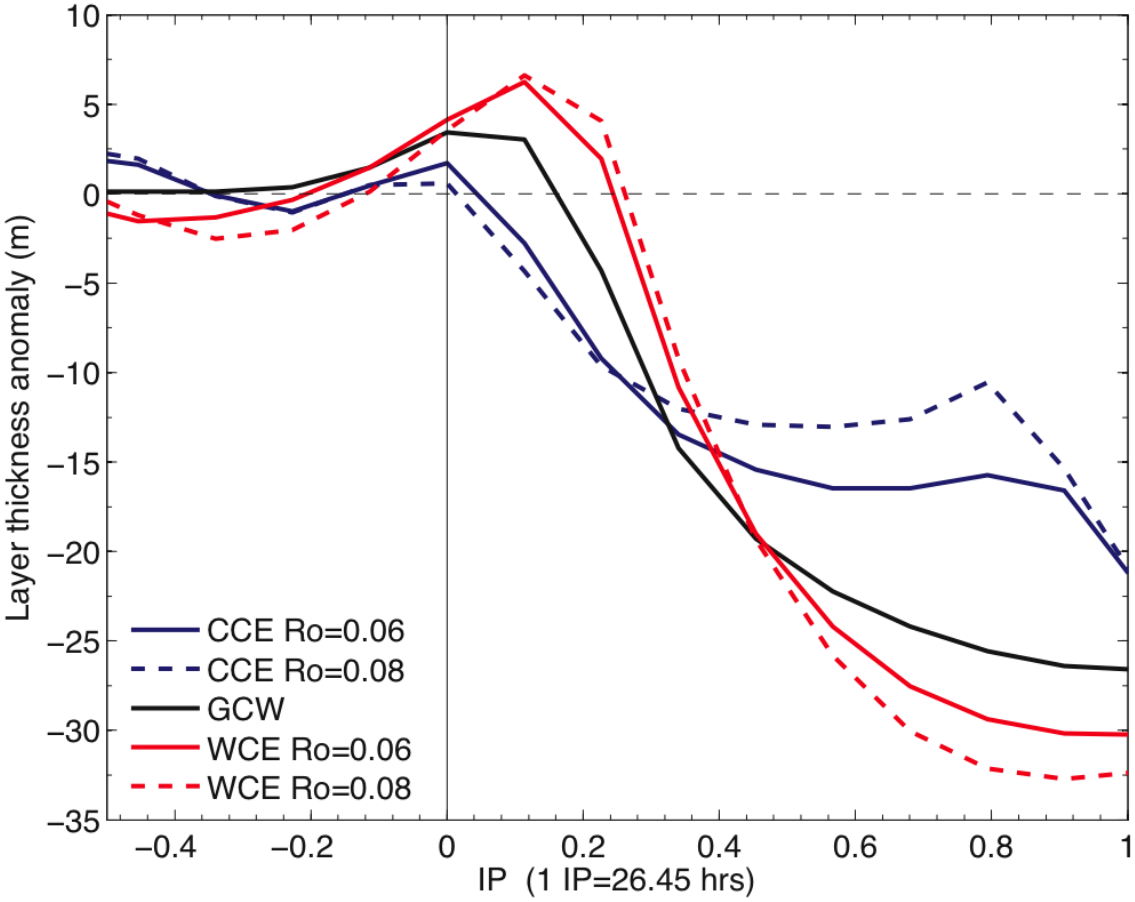

Figure 5.5: Evolution of layer thickness anomaly η in the top layer of the ocean model at mooring *a* (see Fig. 5.3), where η(IP) = h(IP) - h(IP =-1.5), and h is the instantaneous OML thickness. Mooring *a* was under the storm's eye approximately from IP=-0.25 to IP=0.25. The model initial state corresponds to IP=-1.5.

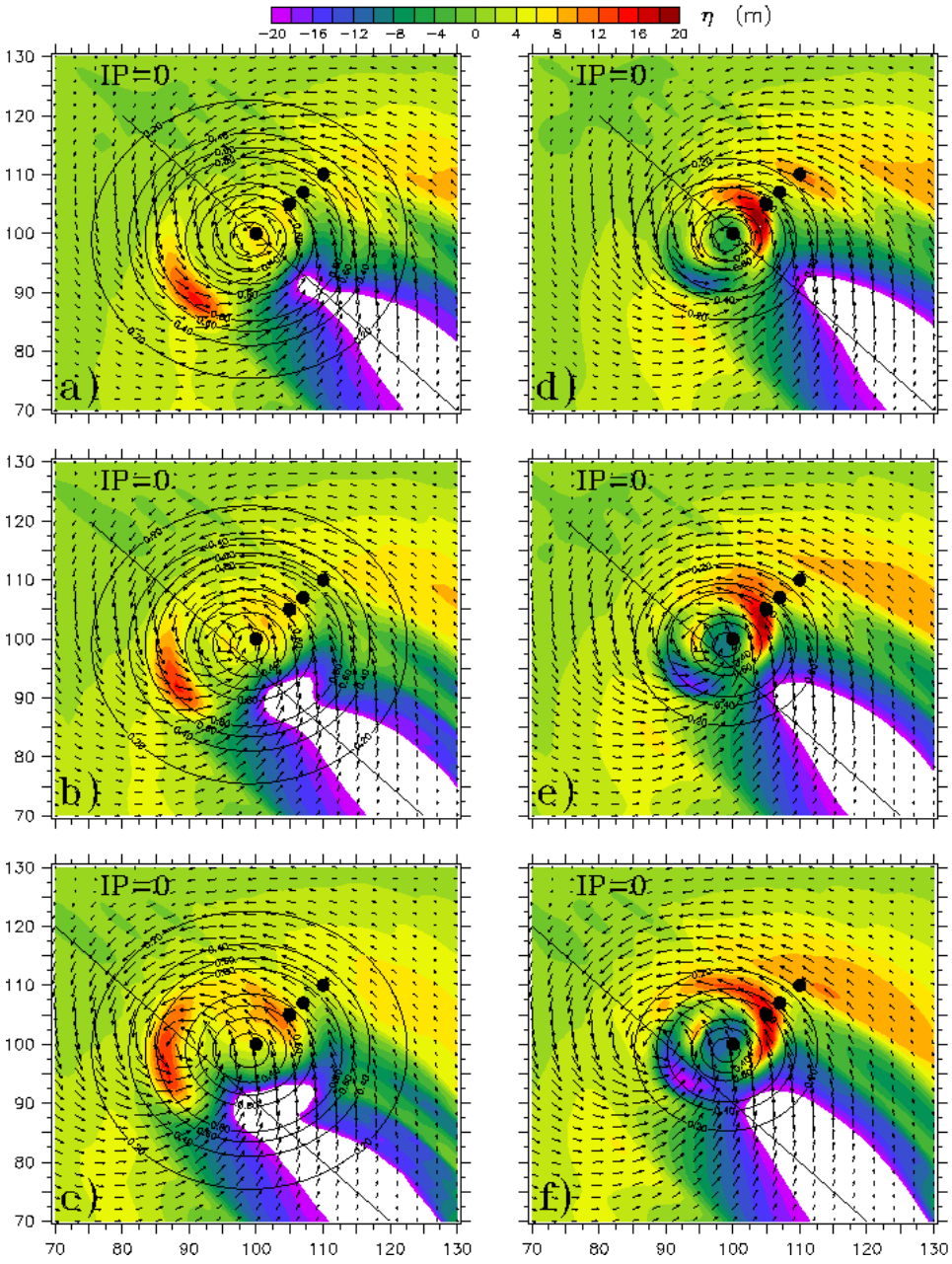

Figure 5.6: OML thickness anomaly η for WCE1 (left panels) and CCE2 (right panels), where $\eta = h(IP = 3) - h(IP = -1.5)$, and h is the instantaneous OML thickness. In (b) and (e) the storm track is shifted 0.5^{o} to the west, while in (c) and (f) the track shifting is 1^{o}. Circular contours are the initial magnitude of OML geostrophic currents; the contour interval is 0.2 m s^{-1}.

Morel and Thomas (2009) evaluated Stern's (1965) theory in a series of numerical experiments. They found that the dipole emerges in QG vortices even when these features

are influenced by a uniform wind stress with no curl. In Morel and Thomas' (2009) experiments (and so in Stern's theory), the dipole is driven by the curl of the wind-driven acceleration of geostrophic currents. This curl emerges where the initial OML thickness is not uniform (as in WCEs and CCEs). Under these circumstances, the strong gradient of geostrophic vorticity acts like a beta effect that creates secondary potential vorticity anomalies in the inner vortex region. The differential advection of geostrophic vorticity by the wind stress is the mechanism that creates the dipole. The two dipole's components are known as beta gyres, and they arises because $\nabla\zeta_g$ is positive on one half of the vortex interior, and negative on the other inner half.

In WCEs (Fig. 5.6a, b, c), the region of upwelling is confined to the southeast quadrant because when the frontal region of the storm passed over this area, both the wind stress and geostrophic currents were predominantly southward. Thus, the background currents were accelerated by the wind, becoming divergent over this region. The predominance of downwelling regimes over most of the inner region of WCEs results because during most of the time of direct interaction, the wind stress vector is against OML geostrophic currents. Under these circumstances, the background OML currents are weakened by the wind stress, which produces horizontal mass convergence that is compensated by a downwelling velocity. In the case of CCEs, an inverse scenario takes place.

5.3 OML deepening

The OML thicknesses shown in Fig. 5.5 and 5.6 are about 15 m shallower compared to post storm OML depths measured after hurricanes Katrina and Rita (Fig.

3.3). To reproduce a more realistic OML response, now we consider Eq. (5.5) that includes OML deepening driven by the vertical entrainment velocity w_e.

5.3.1 Entrainment model

The vertical entrainment velocity w_e across the OML base is calculated with a turbulence closure based in the model of Niiler and Kraus (1975). This closure assumes that the rate of production of turbulent kinetic energy (TKE) less dissipation equals the rate of work done by turbulence against buoyancy. By neglecting air-sea fluxes, the steady-state balance obtained by vertical integration of the TKE equation upon the OML is (parameterized form):

$$\underbrace{g\frac{\delta\rho}{\rho_0}\frac{h}{2}w_e}_{PE} = \underbrace{m_1 w_*^3}_{WIND} + \underbrace{m_2 w_e \frac{\delta \mathbf{v}^2}{2}}_{SHEAR}, \tag{5.7}$$

where *PE* is the rate of potential energy increase due to entrainment processes, *WIND* is turbulence production due to wind stress [$w_* = (\tau/\rho_0)^{1/2}$], and *SHEAR* is turbulence production due to vertical shear of horizontal currents. By assuming that the energy generated by *SHEAR* is either dissipated locally or used to entrain denser water from below with relatively little energy being radiated away, the effects of dissipation and internal waves are typically embedded into the empirical parameter m_2, which together with m_1 represent the mixing efficiency of the entrainment sources.

Kraus and Turner (1967) considered only the *WIND* source (m_2 = 0). Price at al. (1978) investigated the relative contribution of *WIND* and *SHEAR* to entrainment cooling during hurricane passage with two mutually exclusive simplifications of Eq. (5.7): (i) the turbulent erosion model (TEM) or stirring-induced entrainment (m_2 = 0), and (ii) the

dynamic instability model (DIM) or shear-driven entrainment (m_1 = 0). The central assumption in the DIM closure is that $m_2 = R_b = \left(g' h / \delta \mathbf{v}^2\right)$, where R_b is the bulk Richardson number. Jacob and Shay (2003) included air-sea fluxes in Eq. (5.7), and they used several simplifications of this equation to simulate the OML response to TC Gilbert.

A common practice is to use a bulk OML and set $m_1 = R_b = 1$ as a critical stability criterion in the DIM model: there will be no entrainment at sub-critical ($R_b > 1$); but there will be so much at super-critical ($R_b < 1$) that an adjustment back to critical is forced. The main assumption is that while h is increasing the flow is marginally stable, that is $g' h = \delta \mathbf{v}^2$ (Pollard et al. 1973). Critical limits at R_b = 0.65 have also been used (Price et al. 1978). OML deepening may require turbulent mixing not only at the OML base, but also in the stratified ocean underneath (D'Asaro 1985; Price et al. 1986). In this case, the stability criterion is defined in terms of a gradient Richardson number R_g, as discussed below.

Integration of Eq. (5.7) for a time step Δt gives:

$$w_e g \frac{\delta\rho}{\rho_0} h \Delta t = \Delta t \left(E_1 + E_2\right), \tag{5.8}$$

where $E_1 = 2 m_1 w_*^3$, and $E_2 = 5 \times 10^{-4} R_b^{-4} \delta \mathbf{v} g' h$ is the parametric form of the shear term of Eq. (5.7), derived from laboratory experiments and valid for $R_b \leq 1$ (Price et al. 1978). For cases in which OML deepening involves turbulent mixing in the stratified ocean below the layer (Price et al. 1986): $E_2 = 5 \times 10^{-4} R_g^{-4} \delta \mathbf{v} g' h$, where

$$R_g = g \frac{\partial\rho / \partial z}{\rho_0 \left(\partial \mathbf{v} / \partial z\right)^2}$$

is the gradient Richardson number. The turbulence closure used in this investigation considers the later definition of E_2. The closures for E_1=0 and E_2=0 are named Price-Weller-Pinkel (PWP) and Kraus-Turner (KT), respectively.

Two general cases are investigated: (i) instantaneous wind erosion alone (KT), that is the forced stage; and (ii) turbulent entrainment due to both instantaneous wind erosion and shear-driven mixing (KT+PWP). In the later case, for each model time step, the computation of KT is followed by the computation of PWP in the stratified ocean below the OML, until the stability criterion is satisfied (cf. Price et al. 1986). Two stability criteria are tested: R_g=[1, 0.65] (Table 5.2). The implementation of KT in MICOM is discussed in detail in Bleck et al. (1989).

5.3.2 Wind erosion during the forced stage

Compared with the upwelling velocity, instantaneous wind erosion produced an additional OML deepening of about 20 to 25 m in the WCE1, and from 10 to 15 m in the CCE2 (Fig. 5.7). The cooling associated with this OML deepening is of about 0.3, 1.5, and 3^{o}C in the WCE1, GCW, and CCE2, respectively (Fig. 5.8). The OML cooling of less than 0.5^{o}C, together with an important layer deepening of about 25 m, indicate that most of the vertical mixing in WCE1 takes place over a nearly homogeneous and deep warm water column. Weak stratification (Fig. 5.2) at the OML base of this warm feature facilitated wind erosion. By contrast, in CCE2 the stronger stratification reduced wind erosion during the forced stage.

Table 5.3: Stratification characteristics inside the QG vortices, with $g' = g(\rho_2 - \rho_1)/\rho_0$. ρ_1 is the initial OML density, and ρ_2 is the density of the contiguous layer below.

Vortex	ρ_1 (kg m^{-3})	ρ_2 (kg m^{-3})	ρ_0 (kg m^{-3})	g' (m s^{-2})	h (m)	$g'h$ (m^2 s^{-2})
CCE2	1024.40	1025.35	1025.00	9.2x10^{-3}	30	0.27
WCE1	1022.72	1022.74	1025.00	0.1 x10^{-3}	70	0.02

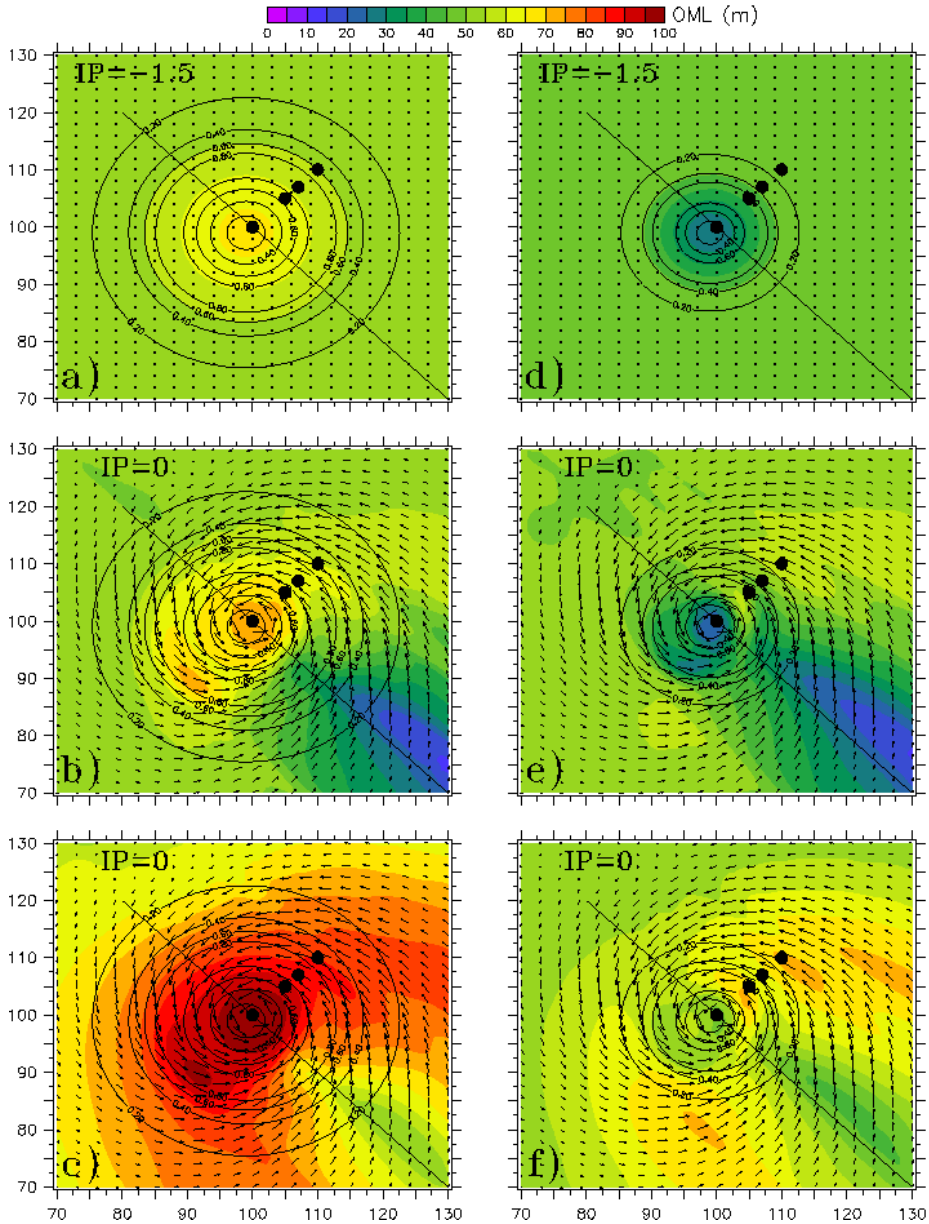

Figure 5.7: OML deepening during the forced stage in WCE1 (a-c) and CCE2 (d-f). (a, d) Pre-storm OML thickness. (b, e) Change of layer thickness due to horizontal current divergence (as in Fig. 5.6). (c, f) OML deepening due to instantaneous turbulent wind erosion (KT model).

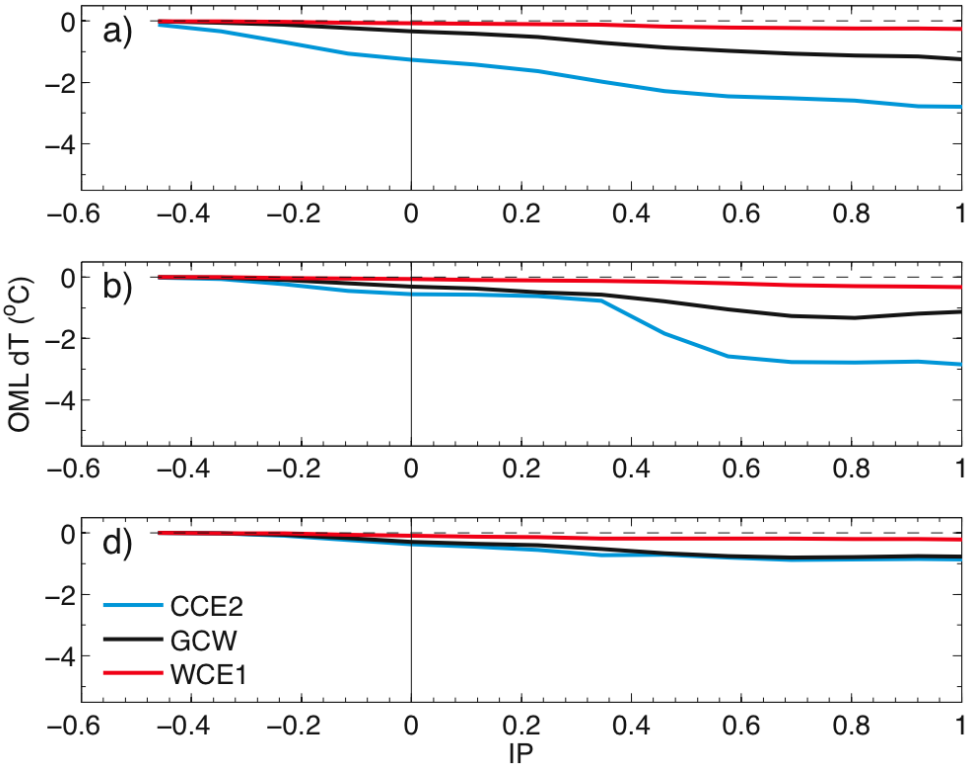

Figure 5.8: OML cooling during the forced stage at moorings a, b, and d, caused by instantaneous wind erosion (KT model), with dT(IP)=T(IP)-T(IP=-1.5).

Mathematically, from Eq. (5.8) and with E_2=0: $w_e \propto w_*^3/(g'h)$. As shown in Table 5.3, for the same wind forcing, the entrainment velocity due to wind erosion can be up to 10 times bigger in WCE1 than in CCE2, because $g'h$ inside the former feature is about 10 times smaller (weaker stratification).

5.3.3 Shear-driven entrainment

The incorporation of vertical shear-driven mixing (KT+PWP), for a critical limit R_g=1, reproduced an additional OML cooling of about 0.1°C (in average) for the region on the right side of the storm track in WCE1 (Fig. 5.9a, c). Maximum additional cooling of about 0.3°C was reproduced in the region of confluence of the dipole (in the vicinity of the moorings). Nevertheless, the small difference between KT and KT+PWP indicates

that in this warm anticyclone most of the cooling was driven by instantaneous wind erosion, and near-inertial vertical shear was not an important cooling mechanism, in accord with observational evidence presented elsewhere (Chapter 3 and 4; Shay and Uhlhorn 2008). In the case of CCE2, PWP reproduced an additional cooling of more than 1.2°C that confirms the importance of vertical shears for OML cooling in this cyclone (Fig. 5.9b, d).

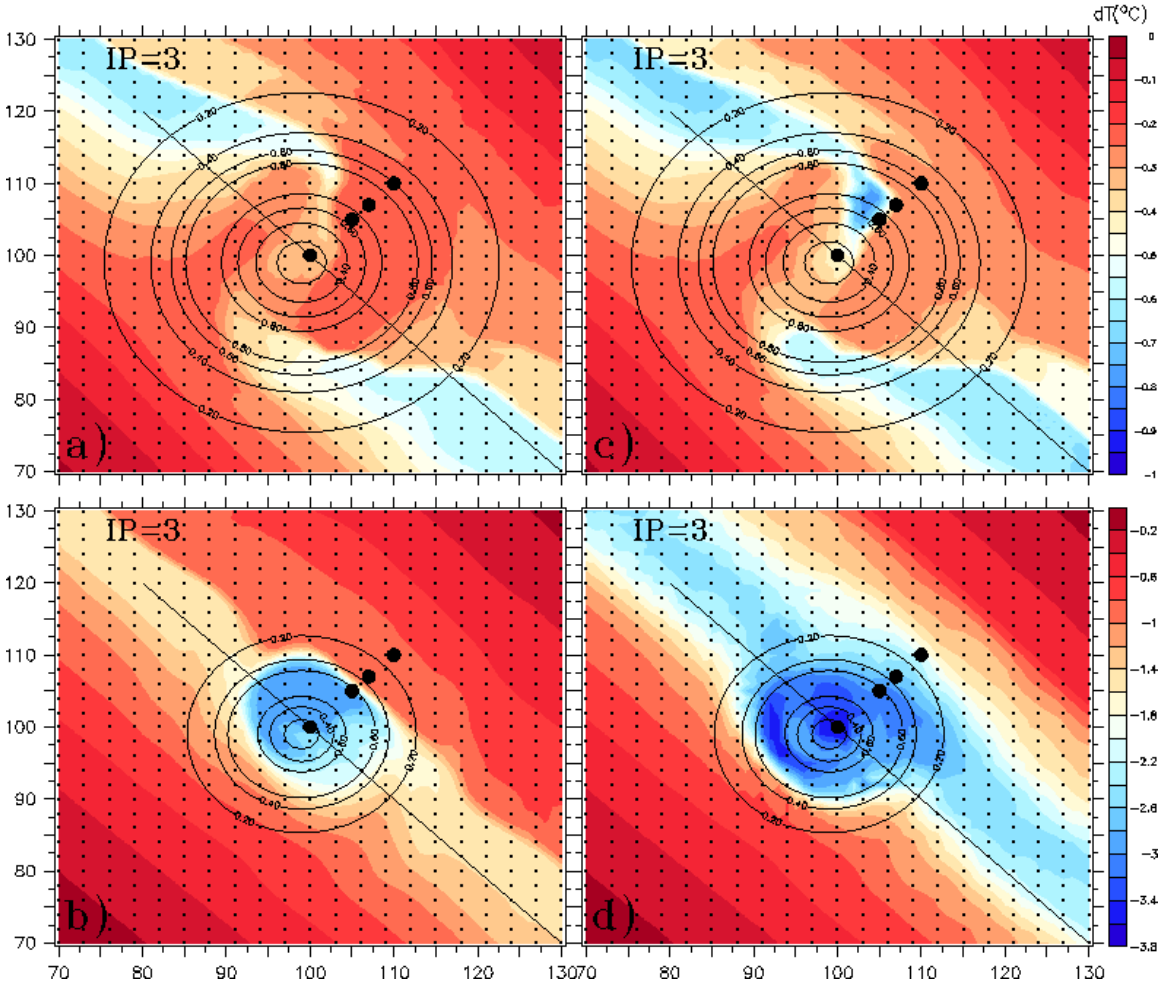

Figure 5.9: OML cooling *dT* in WCE1 (upper panels) and CCE2 (lower panels), in terms of the KT turbulence closure (a and b), and KT+PWP (c and d). Notice the difference in the temperature scale between upper and lower panels. $dT = T(IP = 3) - T(IP = -1.5)$.

5.4 Near-inertial velocity response

5.4.1 Decay of oceanic mixed layer near-inertial currents

During the first half of the IP, the OML velocity response in WCE1 is nearly in phase with the velocity response in CCE2 and GCW (Fig. 5.10). Later on, the background circulation influences the velocity response. In the case of WCE1, near-inertial currents increase their periodicity as the underlying anticyclonic circulation shifts the response toward lower frequencies. After the first 3 IP, OML near-inertial currents in WCE1 are 180^{o} out of phase compared to CCE2 and GCW. By contrast, OML near-inertial currents in CCE2 become about 90^{o} out of phase respect to GCW after 10 IP. Notice that the mixing schemes have a negligible impact on the frequency shifting.

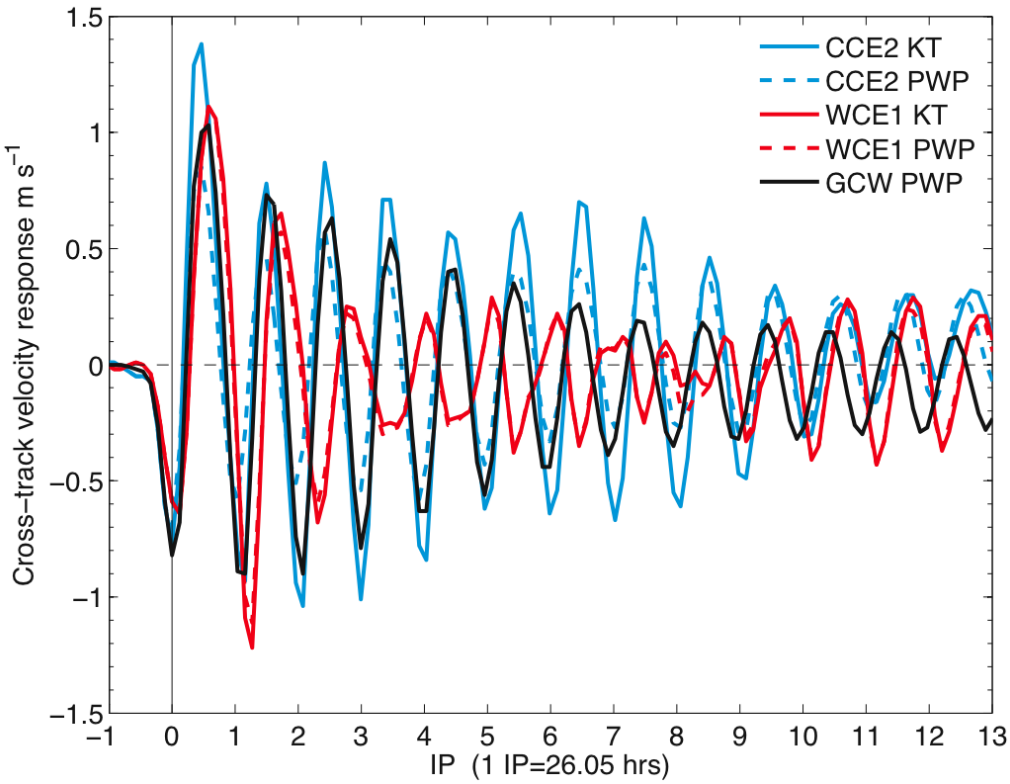

Figure 5.10: OML velocity response at mooring *b*, in function of vertical entrainment. The label PWP refers to KT+PWP.

However, the most striking effect of the background vorticity is on the amplitude of the velocity response, as OML near-inertial energy decays much faster in WCE1, and its decay is delayed in CCE2, relative to GCW. This contrasting behavior is consistent with observational data (Chapter 4), theoretical expectations (Kunze 1985) and numerical predictions (Lee and Niiler 1998). Hence, numerical models that neglect geostrophic features can significantly underestimate or overestimate the amount of OML near-inertial energy available for vertical entrainment and layer cooling (compare WCE1 and CCE2 with GCW).

The OML velocity response in WCE1 is nearly identical for KT and KT+PWP, which confirms that vertical shears at the OML base of this warm feature are of secondary importance during the layer response. This result is consistent with observational evidence acquired during hurricanes Katrina and Rita (Chapter 4), and Isidore and Lili (Shay and Uhlhorn 2008). By contrast, vertical shears in CCE2 reduce the OML velocity amplitude by about 40% over the first 6 IP (Fig. 5.10).

The OML velocity response takes place at higher frequencies for smaller *Ro* (Fig. 5.11). For example, after 10 IP there is a phase lag of about 45^{o} between OML near-inertial oscillations inside CCE1 (*Ro*=0.06) and those inside CCE2 (*Ro*=0.08). That is, near-inertial currents complete a cycle in a shorter time period (higher frequency) inside the more slowly rotating CCE1 than inside CCE2. This shifting toward higher frequencies at smaller *Ro* is more evident during the first 6 IP in WCEs. Near-inertial currents inside the more slowly rotating WCE1 (*Ro*=0.06) lead the OML velocity response, and after 6 IP there is a large phase lag of about 180^{o} respect to WCE2 (*Ro*=0.08).

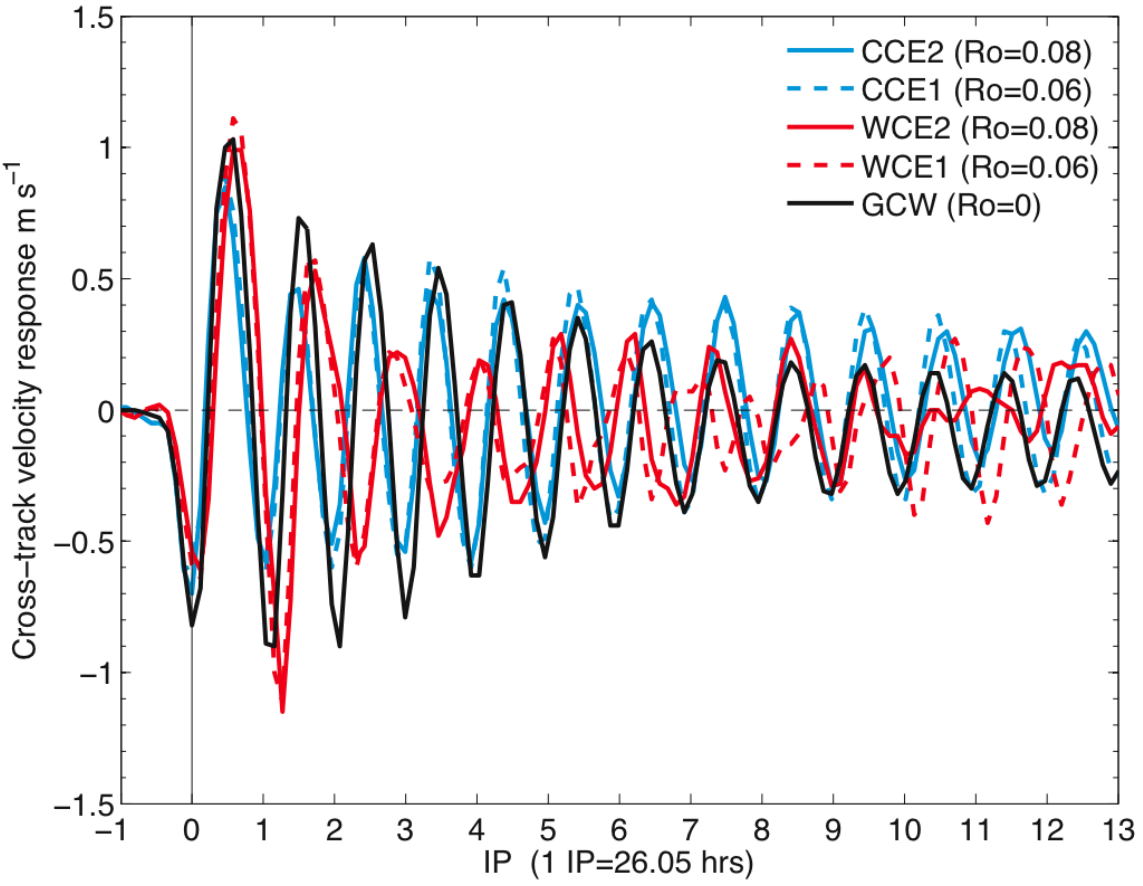

Figure 5.11: OML velocity response at mooring *b*, in function of *Ro* (see Table 5.1). KT+PWP is the turbulence closure used in this experiments.

Background relative vorticity modulates near-inertial currents over the total vertical extension of the QG vortex. The difference in phase of the near-inertial response between WCE1 and CCE2 increases with depth (Fig. 5.12). Moreover, near-inertial currents inside these features are out of phase up to 180^{o} respect to quiescent ocean conditions (GCW). Near-inertial currents are more energetic below the OML and above the 150-m depth inside WCE1. However, between 3 to 9 IP, the near-inertial response is more intense at a depth of about 200 m inside CCE2.

An important feature of the velocity response inside CCE2 is the flattening of currents' amplitude at about 100 m depth (Fig. 5.12, upper panel). This flattening

indicates periods when vertical shears reach criticality, so that the mixing scheme (PWP) removed excess energy to maintain the currents at dynamically stable levels. These intermittent periods therefore represent a sink of near-inertial wave energy, consistent with direct measurements inside the CCE affected by Katrina (section 4.5). By contrast, near-inertial currents at a depth of about 100 m inside WCE1 do not reach criticality, because they are in phase with the currents underneath (little vertical shear).

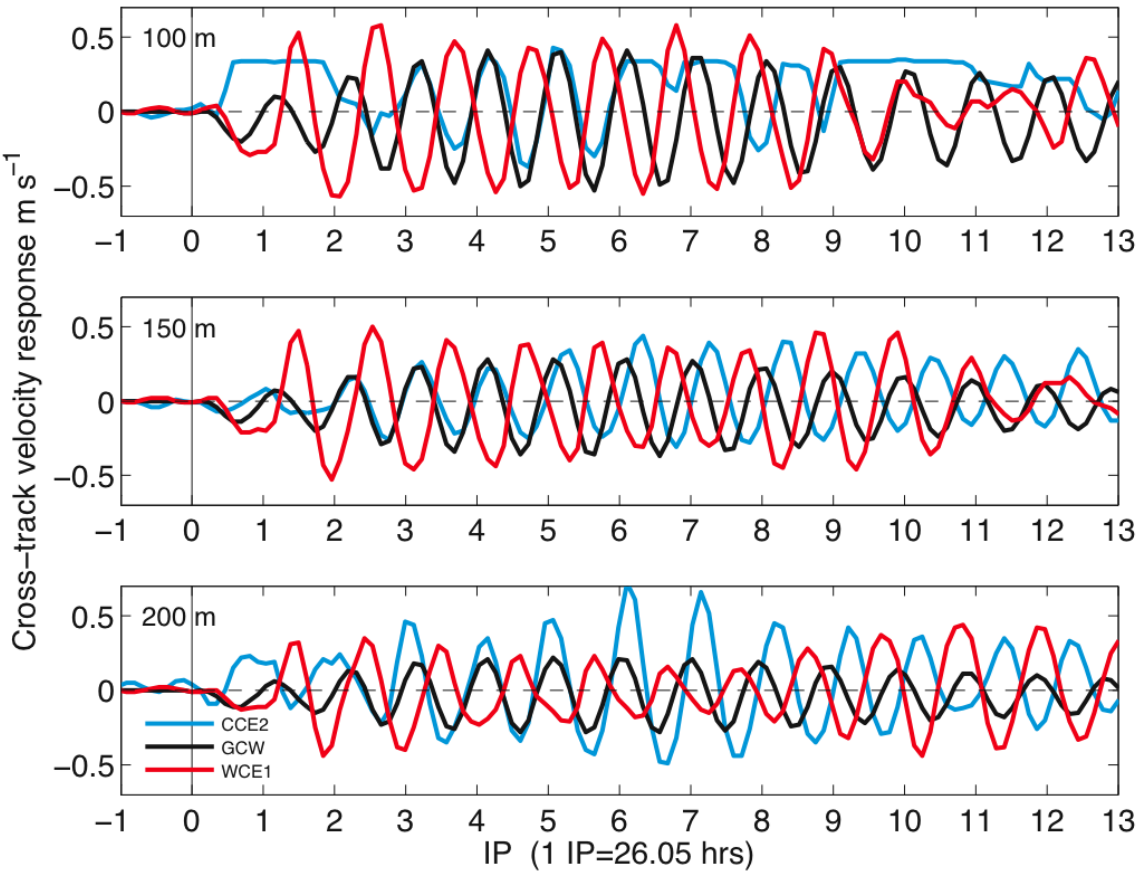

Figure 5.12: Near-inertial velocity response in the upper 200 m at mooring *b* (KT+PWP closure).

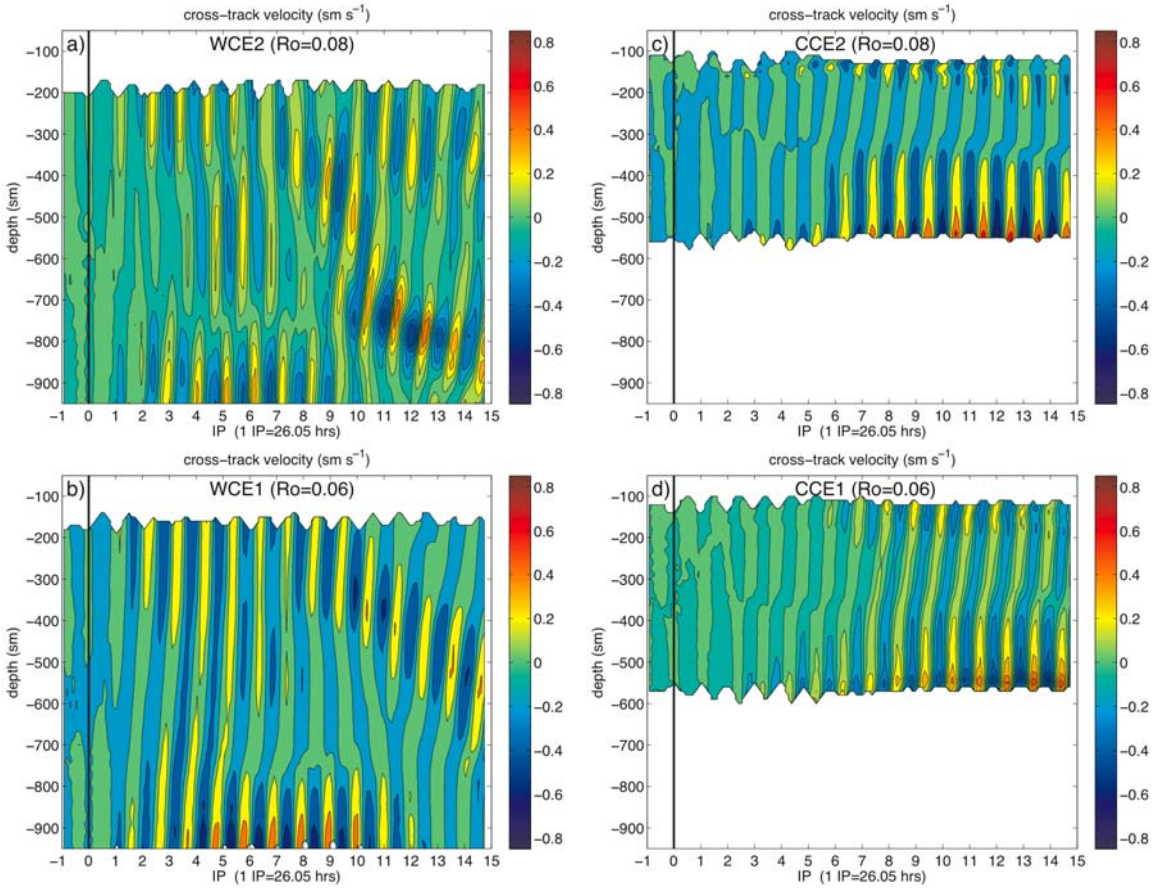

Figure 5.13: WKBJ-scaled velocity response at mooring *b* (KT+PWP closure). The unit 'sm' stands for stretched meters. Notice that depth is also scaled. These velocity fields are interpolated into a regular vertical grid.

To better illustrate the effects of ζ_g on the near-inertial response below the OML, WKBJ-scaled velocities are presented in Fig. 5.13. One of the most salient aspects is the propagation of more downward beams inside WCEs (Fig. 5.13a, b). This characteristic, together with the rapid decay of OML currents (Fig. 5.10), confirms that in these anticyclones most of the kinetic energy injected by the hurricane is radiated into the ocean interior. Inside the CCEs, wave activity is reduced below the OML (Fig. 5.13c, d), as near-inertial energy is trapped in upper layers. This contrasting near-inertial velocity response is in agreement with the direct measurements discussed in Chapter 4. The bursts

of deep near-inertial energy, in both WCEs and CCEs, can be associated to the development of forced baroclinic modes (cf. Kundu and Thomson 1985; Shay et al. 1989).

Inside the WCEs, the surface currents are 180^o out of phase respect to the bottom currents during the first 5 IP (Fig. 5.13a, b), which is consistent with the velocity structure of the first baroclinic mode. The velocity inflection point is located at about 500 m depth, which suggests that the vertical length of this normal mode is ~1000 m (or the approximate vertical length of the WCEs). CCEs also exhibit velocity structures consistent with the first normal mode that prevails during the first 15 IP. In this case, the change of current direction occurs at ~300 m depth, corresponding to a vertical scale of about 600 m for the first baroclinic mode. This length scale is apparently defined by the vertical distribution of positive values of ζ_g inside the vortex that vanishes below this depth. An examination of the observational data shows that the velocity inflection points are located at a depth of about 300 m and 450 m inside realistic CCE and WCE structures, respectively (Fig. 4.9), in agreement with the model results. This suggests that rather than the vertical scale of the water column, it is the vortex's vertical length that determines the vertical scale of normal modes.

Mode separation is more evident in WCE2 (Fig. 5.13a), where the number of velocity inflection points in the water column increases with time (dispersion of higher modes). Mode separation is delayed inside the more slowly rotating WCE1 (Fig. 5.13b). From 10 to 15 IP, and for each IP, the current structure inside this vortex exhibits two flow reversals with depth that suggest a current structure consistent with the second baroclinic mode. The apparent lack of near-inertial wave activity at higher modes inside

WCE1 could be the result that f_e is smaller, so that higher modes can freely leave the vortex (Kunze 1985). Another possibility is that the stronger rotational constrains collapse the near-inertial response into a narrower sub-inertial band (section 5.4.2). This tendency for homogenizing frequency is also present in CCE1, where the phase is more uniform with depth than in CCE2. The lack of near-inertial wave activity at higher modes (more vertical structure) below the OML base inside these CCEs suggests that higher modes are trapped in surface layers. The energy of these higher modes is expelled toward the outside (as indicated by wave rays in Fig. 4.6), and is used to increase vertical shears and entrainment cooling (cf. Shay et al. 1989).

The high energy levels at the bottom of WCEs, together with intermittent wave packets propagating downward, suggest near-inertial wave amplification with depth, consistent with theoretical predictions (Kunze 1985) and numerical experiments (Lee and Niiler 1998). However, in the case of CCEs, the high energy levels at the bottom do not seem to depend on direct propagation from the surface. Gill (1984) argued that motion at the bottom is possible as soon as the forcing is turned on, presumably due to reflection of the first forced mode structure.

5.4.2 Frequency shifting

A frequency analysis similar to that introduced in section 4.4.3 is shown in Figure 5.14. In the vortex-free ocean (Fig. 5.14c), the frequency of near-inertial current response is nearly homogeneous with depth, and it is centered mostly at 1.05*f*. This blue shifting under quiescent ocean conditions is a distinctive characteristic of near-inertial energy

(Kundu and Thomson 1985), and its caused by the contribution from the buoyant frequency that allows vertical propagation from the OML.

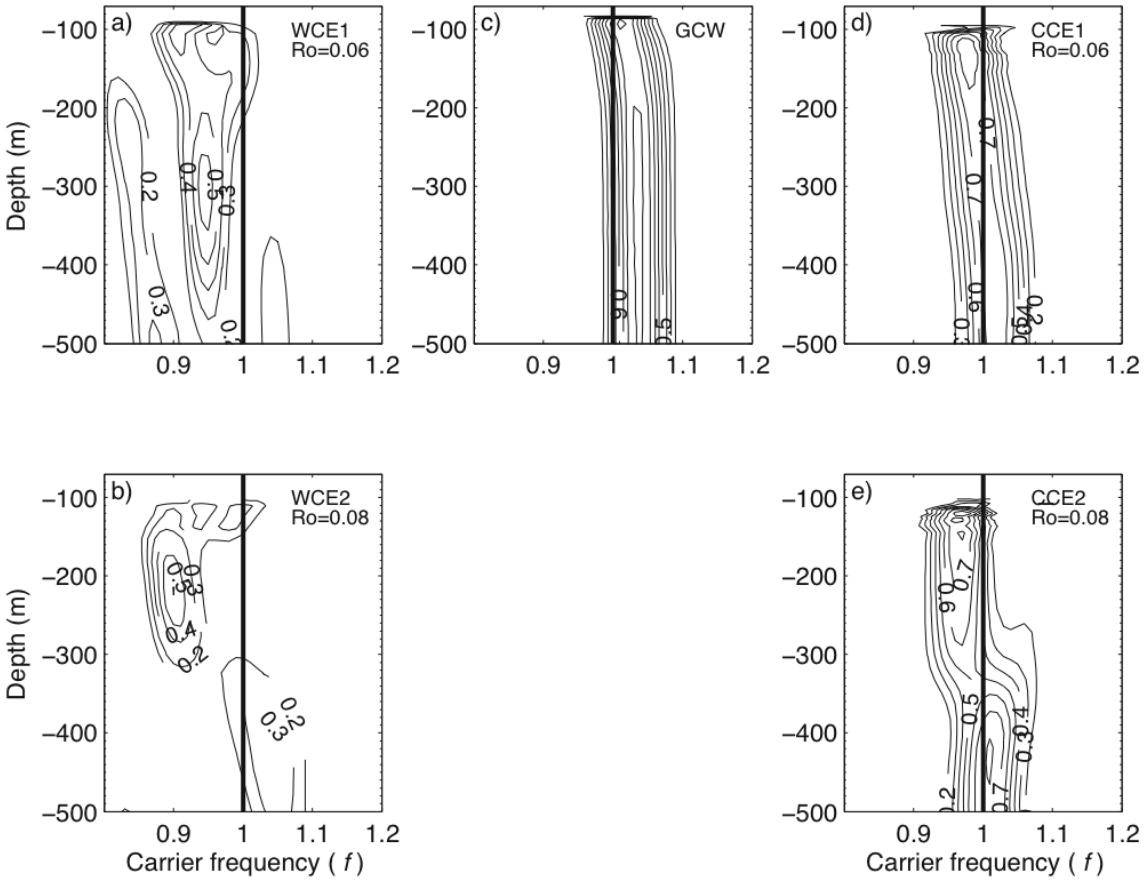

Figure 5.14: Frequency of the near-inertial response at mooring *b*, in terms of frequency fits (section 4.3.3) and the PWP turbulence closure. Contour interval is 0.1*f*.

For similar *Ro* (Fig. 5.14a, d), the near-inertial response occurs at lower frequencies in WCEs compared with CCEs, because f_e is smaller. At higher *Ro*, the more rapid rotation of the vortex moves the near-inertial response into a more sub-inertial frequency passband. The more rapidly rotating vortices (Ro=0.08) produce a bimodal distribution of frequencies, where the near-inertial response occurs at sub-inertial frequencies in upper waters, and at super-inertial frequencies in deep waters. The sharp

transition from sub-inertial to super-inertial frequencies occurs at a depth of ~300 m. Notice that in CCE2 (Ro=0.08), the vertical distribution of near-inertial frequencies is similar to that induced by Katrina inside a CCE (Fig. 4.9). Both in this real CCE and in the model CCE2, the reversal from sub-inertial to super-inertial frequencies occurs at a depth of about 300 m. This depth coincides with the depth of velocity reversal presumably associated with the first baroclinic mode for a 600 m vertical scale (Fig. 5.13c and 5.14e). As discussed in section 4.4.3, the red-shift in upper layers of CCEs could be the result of a frequency delay produced by the geostrophic Doppler term in Eq. (4.3).

5.4.3 Vertical wavenumber spectrum

Near-inertial wave kinetic energy spectra change as a function of the cross-track distance from the vortex center (Fig. 5.15, compare left and right panels). For example, at mooring *b*, the model CW spectra are one order of magnitude larger than the CW spectrum from observational data, while the model ACW components are similar to the observed ACW spectrum at small vertical wavenumbers. At mooring *d*, the model and observed spectra have similar energy levels for both ACW and CW components, though there is a lack of energy at small wavenumbers. Notice that mooring *b* is located in a region of cyclonic relative vorticity ($\partial \upsilon / \partial r > 0$, r is the radial distance from the vortex's center), while mooring *d* is located in a region of anticyclonic relative vorticity ($\partial \upsilon / \partial r < 0$).

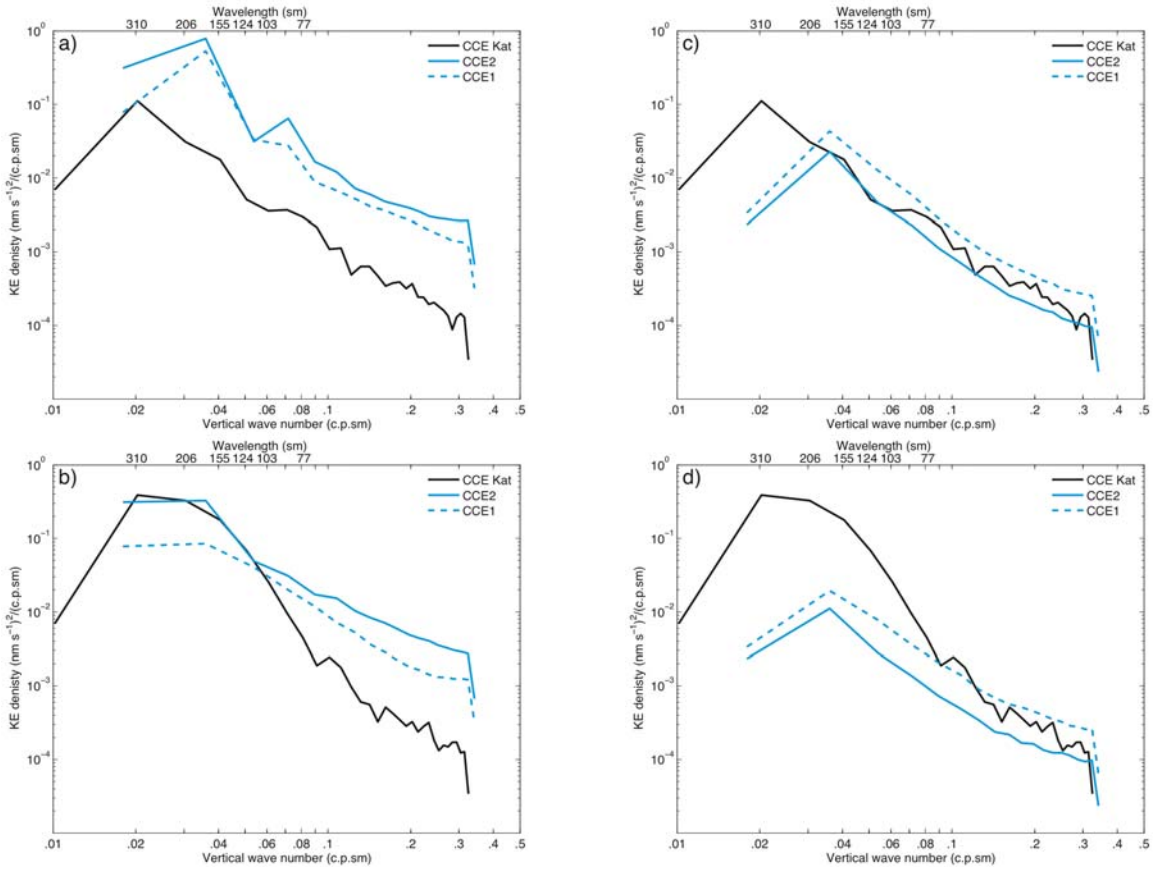

Figure 5.15: Vertical wavenumber rotary spectrum. (a, b) Mooring *b*, and (c, d) mooring *d*. Upper panels are CW spectra (downgoing energy), and lower panels are ACW spectra (upgoing energy). Solid black lines are spectra from observational data acquired during hurricane Katrina (section 4.4.4).

At mooring *b*, for the same mixing scheme (KT+PWP), energy levels are larger in CCE2 (*Ro*=0.08) that in CCE1 (*Ro*=0.06), for both CW and ACW components. That is, the more rapidly rotating vortex (CCE2) enhances vertical dispersion in its interior. By contrast, in mooring *d* (exterior side of the vortex, i.e. region of anticyclonic vorticity), energy levels are larger in CCE1 compared with CCE2. This indicates that the weaker rotational constraint in CCE1 allows high-frequency near-inertial waves to propagate horizontally from the center (mooring b, Fig. 5.15a, b) toward the exterior (mooring d,

Fig. 5.15c, d), where the anticyclonic relative vorticity enhances vertical dispersion. This is consistent with the wave rays in CCEs (Fig. 4.6).

Several aspects can explain some of the differences between observed and model spectra: (i) the actual CCE is not stationary due to planetary β and interactions with the LC and other frontal CCEs (that is, the radial distance from the mooring to the vortex's center was changing); and (ii) the real wind stress and translation speed of the storm are not constant. Despite the relative simplicity of the numerical experiments, they reproduce the general structure and energy levels of the observed spectra.

5.5 Critical layer in the cold core eddy

As discussed in section 4.5, a critical layer of increased vertical shear and mixing developed between the depths of 100 and 150 m in the CCE that interacted with Katrina. It is therefore of interest to identify the processes involved in the development of this region of intense mixing and cooling. To this end, vertical distributions of perturbation kinetic energy $\overline{K'}$ are computed from the numerical experiments (Fig. 5.16), as in section 4.5.2.

By comparing with the profile from observational data, it is clear that the more slowly rotating CCE1 does not develop the critical layer (Fig. 5.16a). However, an incipient critical layer develops inside this eddy through shear-driven entrainment and mixing processes. The resulting critical layer is better reproduced at a higher *Ro* (CCE2, Fig. 5.16b). While the KT mixing model does not reproduce the vertical mixing associated with this critical layer, a more realistic distribution of $\overline{K'}$ is obtained by allowing shear-driven entrainment mixing in the stratified ocean. Notice that, the vertical

distribution of $\overline{K'}$ suggests a current structure associated with the first normal baroclinic mode. The minimum in $\overline{K'}$ corresponds to the velocity inflection point of this mode. Apparently, the stronger rotational constraints at higher Ro prevent horizontal radial dispersion of near-inertial energy that facilitates the development of the critical layer.

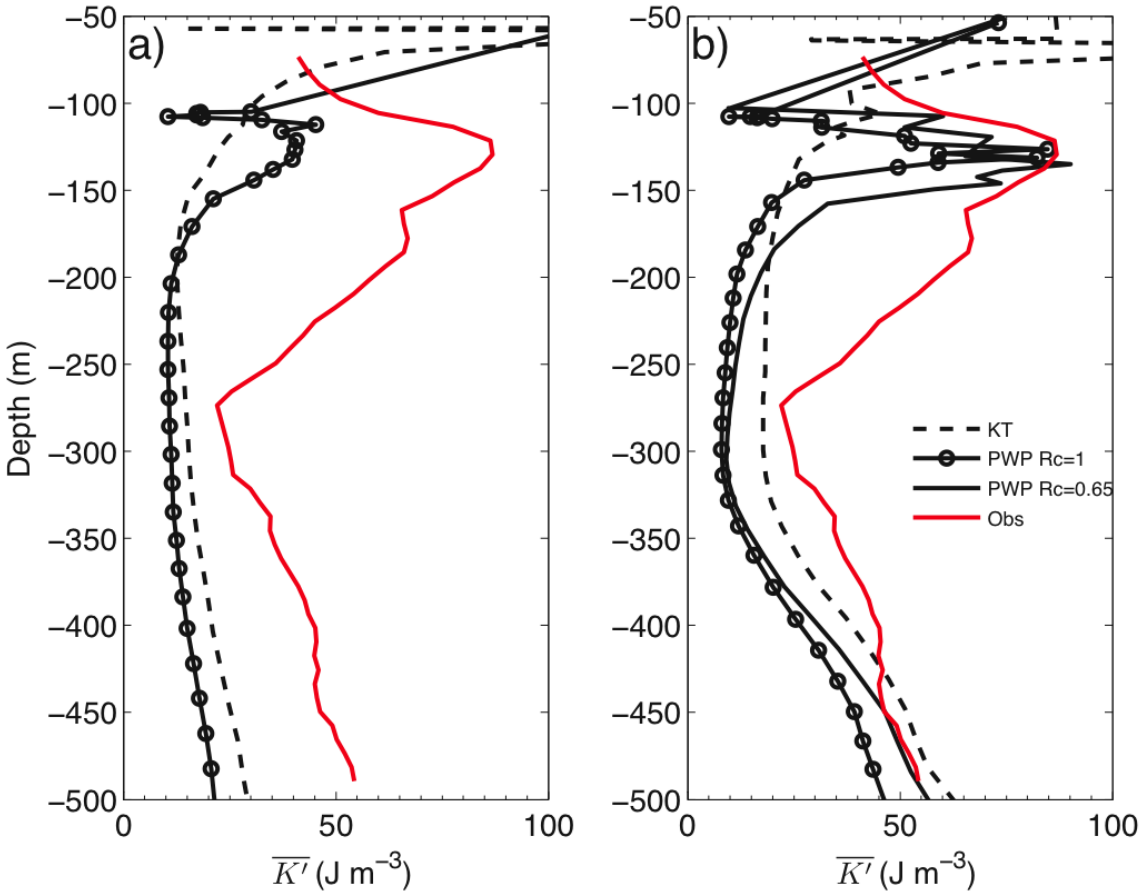

Figure 5.16: Vertical distribution of time-averaged (from 8 to 11 IP) perturbation kinetic energy $\overline{K'}$ at mooring *b*. (a) CCE1 (*Ro*=0.06), and (b) CCE2 (*Ro*=0.08). Red lines are from direct measurements inside the CCE that interacted with Katrina. *Rc* stands for the critical limit of the gradient Richardson number.

5.6 Trapped internal wave wake

As shown in Fig. 4.5a, the region of maximum OML cooling induced by Katrina was located to the left of the storm track two weeks after the passage of the storm, which

suggests that this temperature anomaly was transported by a propagating CCE. To evaluate this idea, two experiments were conducted (one for CCE1 and another for CCE2) in which the β-plane is turned at one IP, or a few hours after the direct hurricane-CCE interaction. There are two corresponding f-plane experiments to compare with (Table 5.2). To evaluate the effects of the hurricane wind stress on the propagation characteristics of CCE2, another β-plane experiment was conducted for this vortex in absence of wind forcing.

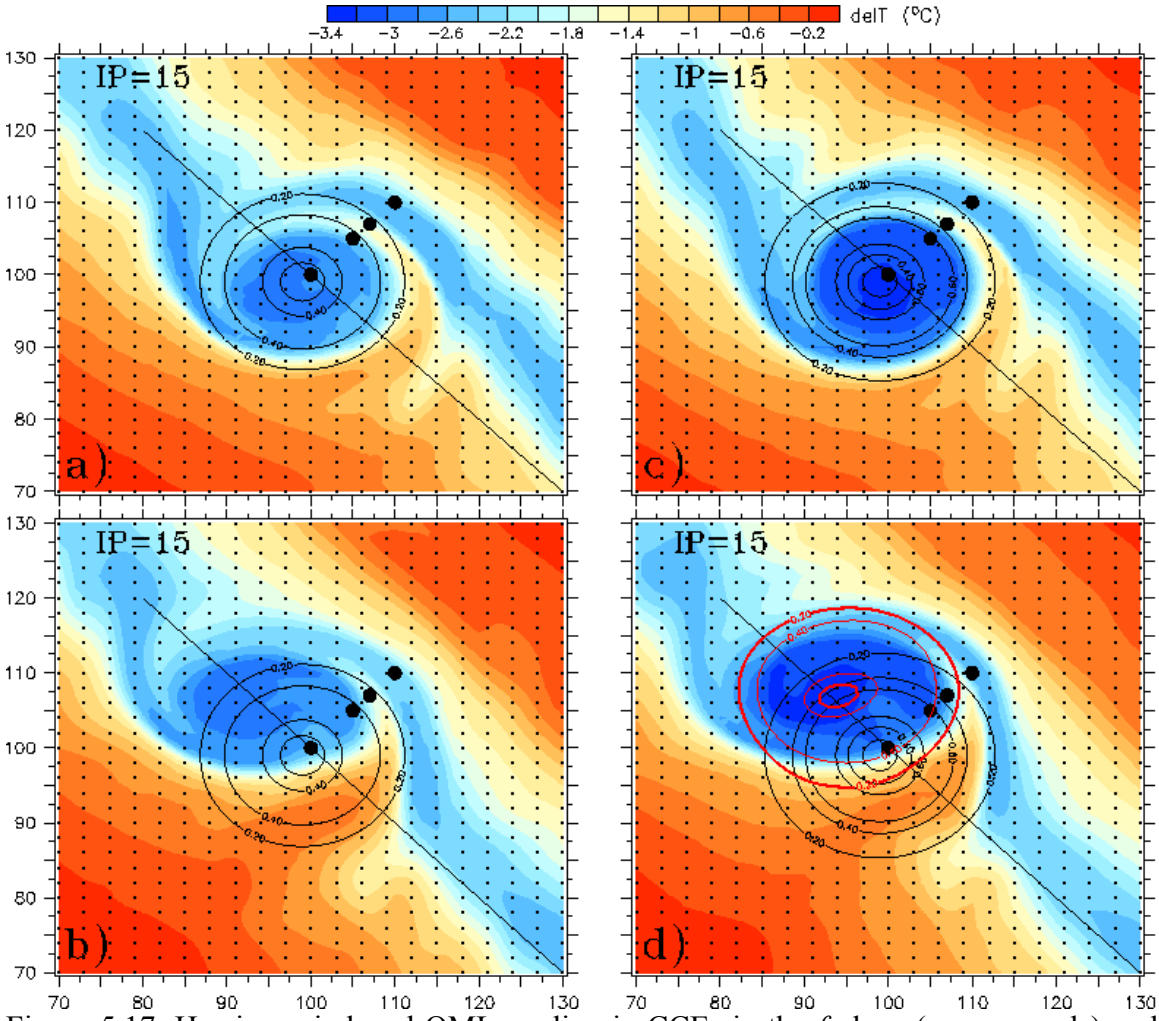

Figure 5.17: Hurricane-induced OML cooling in CCEs in the f-plane (upper panels) and β-plane (lower panels). (a, b) CCE1 (Ro=0.06), and (c, d) CCE2 (Ro=0.08). Circular black contours are the magnitude of OML currents at t = -1.5 IP (initial conditions). Red contours in (d) are the magnitude of OML currents at t = 15 IP for CCE2 in the β-plane, in absence of wind forcing.

In the case of the *f*-plane, the region of maximum hurricane-induced cooling remained stationary with the CCE during the first 15 IP (Fig. 5.17a, c). This indicates that the impulsive hurricane wind stress did not move the CCE from its original position. By contrast, in the β-plane experiments, the CCE drifted northwestward about 100 km from its original position, transporting the temperature anomaly induced by the hurricane wind stress (Fig. 5.17b, d). Notice the additional cooling of about 0.5^{o}C reproduced in the β-plane experiments. The position of CCE2 at IP=15 is basically the same for both the wind forced and non-wind forced β-plane experiments. This confirms that the impulsive wind stress did not have an important impact on the propagation characteristics of CCE2. This northwestward propagation of mesoscale cyclones in a two-layer, primitive-equations, isopycnic-coordinate model is discussed in Cushman-Roisin et al. (1990).

5.7 Effects of the vertical resolution

In models with coarser vertical resolution there is more vertical dispersion of near-inertial energy, and the critical layer is deeper (Fig. 5.18). Given that temperature jumps are higher in models with coarser vertical resolution, the PWP turbulence closure tends to overcool the OML (Fig. 5.19) that impacts sea-air heat fluxes. However, PWP reproduced more realistic OML cooling when high vertical resolution is considered in the stratified ocean below the OML. Therefore, for models to realistically reproduce OML cooling and near-inertial energy decay, they should resolve the stratified ocean between the OML base and the thermocline.

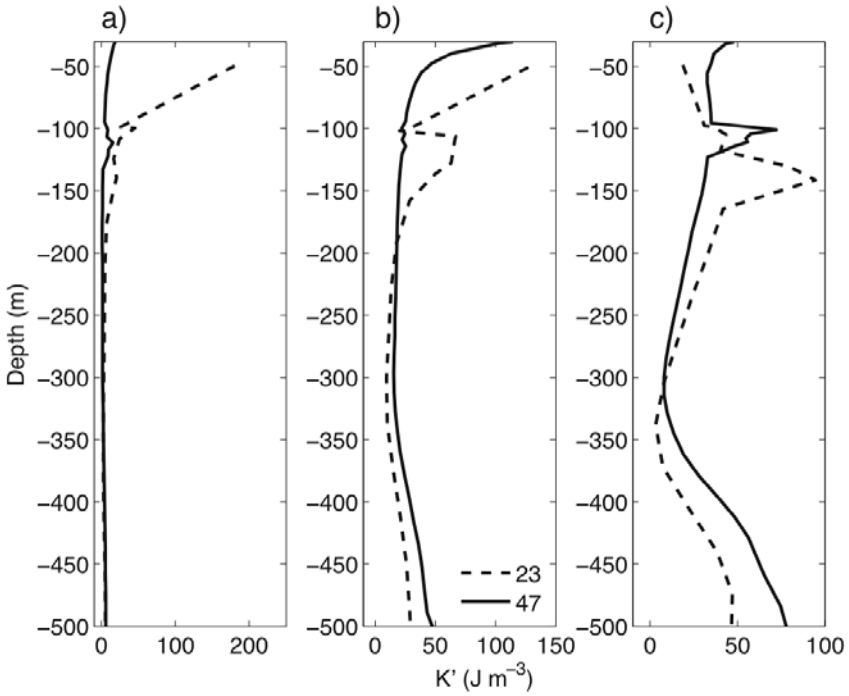

Figure 5.18: Vertical distribution of time-averaged near-inertial kinetic energy inside CCE2. (a) from 1 to 5 IP; (b) from 6 to 10 IP; and, (c) from 11 to 15 IP. 23 and 47 are the number of layers.

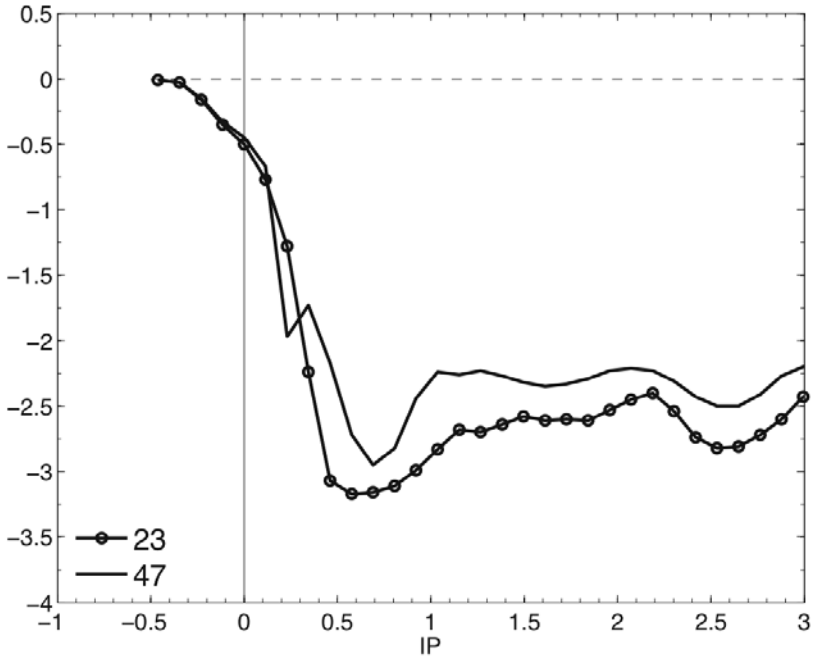

Figure 5.19: OML cooling inside CCE2, as a function of vertical resolution for the KT+PWP turbulence closure; 23 and 47 are the number of layers.

5.8 Summary and concluding remarks

The thermal and velocity response to a hurricane in idealized mesoscale oceanic eddies is investigated, for both cyclones and anticyclones, and for two *Ro* numbers: 0.06 and 0.08. A turbulence closure for the OML is implemented that considers: (i) instantaneous wind erosion proportional to the third power of the surface frictional velocity (KT closure), and (ii) shear-driven entrainment at the OML base and in the stratified ocean underneath (PWP closure).

During the forced stage (first half of the inertial period), the wind-driven horizontal current divergence under the storm's eye is a function of the underlying geostrophic relative vorticity. Upwelling (downwelling) regimes develop when the wind stress vector is with (against) the geostrophic OML velocity vector. This result is consistent with observational data introduced in section 3.3, theoretical predictions (Stern 1965), and more realistic numerical experiments (Halliwell et al. 2008).

Instantaneous wind erosion produces most of the OML cooling in WCEs. The reduced cooling of less than 1^{o}C in this warm feature is a consequence that turbulent mixing occurs over a deep and nearly homogeneous warm water column. This result underscores the importance of the oceanic heat content (relative to the 26^{o}C isotherm depth) for feedback mechanisms to storm intensity. In CCEs, upwelling of cold waters and instantaneous wind stirring during the forced stage produce an OML cooling of about 2.2^{o}C. An additional OML cooling of about 1.6^{o}C was produced by near-inertial shear-driven entrainment along streamlines of maximum azimuthal geostrophic velocity. Considering vertical mixing in the stratified ocean below the OML reproduced more realistic TC-induced layer cooling levels. The reproduced cooling levels in WCEs and

CCEs are consistent with the observational data presented in chapters 3 and 4, and with observational studies reported elsewhere (see section 1.1).

Background geostrophic relative vorticity modulates the vertical dispersion of OML near-inertial energy. The near-inertial velocity response is shifted toward more sub-inertial frequencies inside WCEs, where rapid vertical dispersion prevents accumulation of kinetic energy in the OML, thereby reducing vertical shear development and entrainment cooling. By contrast, higher mode OML near-inertial currents are damped inside CCEs. This energy stalling accelerates OML currents that increase vertical shears and mixing. This contrasting dispersion of near inertial energy is consistent with the observational evidence acquired during Katrina and Rita (chapter 4), with theoretical developments (Kunze 1985), and with non-linear numerical experiments (Lee and Niiler 1998). In general, the blue-shift and red-shit reproduced in CCEs and WCEs, respectively, can be explained by the vertical structure of f_e, with exception of the upper layers in CCEs forced by TCs. Over this depth range, a frequency delay produced by the geostrophic Doppler term could be the mechanism responsible for the red-shift. This hypothesis requires a more detailed investigation.

The rotational and translation properties of the QG vortex have an important impact on the internal wave wake produced by TCs. Observed characteristics of the wake of Katrina inside a CCE, such as the critical layer and the vertical structure of near-inertial currents, were better reproduced at higher *Ro*. As *Ro* increases in CCEs, stronger rotational constraints prevent horizontal dispersion of near-inertial energy toward the vortex's exterior, which facilitates the development of vertical shears and mixing in the interior. Moreover, the upper ocean temperature anomaly and lower frequency near-

inertial oscillations induced by TCs are carried away by the westward-propagating QG vortex.

Observational data and model results indicate that rather than the total water column depth, it is the vertical length of the vortex that determines the vertical scale of forced baroclinic modes. In the case of the GOM, this vertical scale is larger in WCEs than in CCEs. This suggests that, in CCEs, the constrained vertical scale of forced modes is compensated with stronger horizontal currents, because the vorticity injected by the TC is integrated over a shorter vertical length scale. By contrast, in WCEs, this vorticity input is integrated over a larger vertical scale that reduces the amplitude of horizontal OML currents. In quiescent ocean regimes the OML velocity response is a function of the layer thickness, and it is reduced for deeper OMLs because the first baroclinic mode as a larger projection in the layer (Gill 1984).

Chapter 6

Summary and Discussion

Tropical cyclones in the Gulf of Mexico often propagate over the LC, WCEs, and CCEs. These robust mesoscale oceanic features are present at any time, and they often impact the OML thermal response to TCs and feedback mechanisms to storm intensity. For example, observational data acquired during the passage of TCs Katrina and Rita over the eastern Gulf indicated that both storms rapidly intensified over warm, anticyclonically rotating oceanic features (LC and WCEs) where the OML cooling response was reduced ($\Delta T < 1^{o}$C). By contrast, they rapidly weakened over cyclonically rotating CCEs where OML cooling was enhanced ($\Delta T \sim 4.5^{o}$C). In this context, the goal of this dissertation is to delineate this contrasting velocity and thermal response to TCs in mesoscale oceanic eddies.

Airborne-, mooring-, and satellite-based data acquired in the LC system during the passage of Katrina and Rita are used to evaluate the following aspects of the response to TCs in mesoscale oceanic eddies: (i) OML cooling levels; (ii) amplitude of OML horizontal currents; (iii) divergence of TC-forced OML currents and compensating vertical velocity; and (iv) dispersion of TC-forced near-inertial currents. This observational approach is complemented with numerical experimentation with an isopycnic ocean model (MICOM). This model includes a turbulence closure for the OML

that considers: (i) instantaneous wind erosion proportional to the third power of the wind stress (KT closures); and (ii) shear-driven mixing at the OML base and in the stratified ocean underneath (PWP closure). The aim of the numerical approach is to delineate the response to an idealized TC in function of the rotational rate in a QG vortex (sensitivity to *Ro*).

The observational data indicated that, rather than with SST, intensity changes of Katrina and Rita correlate better with the 26^{o}C isotherm depth (proxy of the OHC) that varied in function of the distribution of underlying mesoscale ocean features. More research is needed to evaluate the relative contribution of mesoscale oceanic features to TC intensity fluctuations over the global oceans, compared with atmospheric processes.

Early results indicated that pre-storm OML thickness preconditions the amplitude of horizontal currents in the layer (Jacob and Shay 2003), and the rate of OML energy decay due to vertical dispersion of wind-forced near-inertial currents (Gill 1984). These results were confirmed here, and an additional dynamical process emerged that modulates the OML velocity response: underlying geostrophic relative vorticity ζ_g. The distribution of ζ_g has an important impact on the upwelling of cold water driven by the TC's wind stress, which affects the feedback on storm intensity. The oversimplified use of homogeneous OML distributions (that ignore ζ_g) compromises the predictions of TC-induced OML cooling, which impacts the thermal forcing to atmospheric processes and storm's intensity in numerical models.

TC-induced vertical mixing and cooling in the upper ocean were early linked to vertical shear instability of the third and fourth normal baroclinic modes (Shay and Elsberry 1989). The numerical experiments introduced in Chapter 5 indicate that these

modes are vertically stretched and rapidly disperse vertically inside WCEs, which prevents shear development and mixing. By contrast, these higher modes are stalled in OMLs of CCEs that increases vertical shear and mixing. In this cyclonic features, horizontal dispersion dominates vertical dispersion of higher normal modes. This contrasting near-inertial wave dispersion might explain an important fraction of the reduced TC-induced OML cooling observed in anticyclonic features (Shay et al. 2000; Jacob and Shay 2003; Shay and Uhlhorn 2008; Shay 2009), and increased cooling in cyclonic circulations (Walker et al. 2005; Halliwell et al. 2008; JS09). Direct Eulerian and Lagrangian three-dimensional observations are needed to better depict the three-dimensional dispersion in the wake of TC in the intense GOM's geostrophic circulations. Of particular importance would be verifying the dependence of wave dispersion on *Ro* predicted by the numerical experiments.

Vertical propagation of TC-forced near-inertial wave energy was found to be highly non-linear (Shay and Jacob 2006; JS09). Thus, the presence of mesoscale ocean features can have an important influence in shaping the internal wave spectrum as wind-forced near-inertial waves propagate vertically in the water column. This can be a relevant issue, and more investigation and observations are needed to incorporate the effects of ζ_g for a wide spectrum of *Ro*, density structures, wind intensity, and TC's translation speed.

The contribution of Katrina and Rita winds to the global internal wave power of $O(10^{10})$ W is limited compared with values estimated for the global energy flux from barotropic to internal tides ($\sim 1.3\times10^{12}$, Sjöberg and Stigebrant 1992). These results do not support the hypothesis (Emanuel 2001) that hurricanes significantly drive the Meridional

Overturning Circulation. Given the strength of Katrina and Rita surface winds, and their transfer of momentum to OML and thermocline currents, the result presented here should represent the upper bound to the wind-driven vertical mixing and near-inertial motions in the world ocean.

From a broader perspective, numerical models should be initialized with geostrophic features to improve the representation of wind-induced vertical mixing, and near-inertial wave dispersion. These two processes affect the dispersion of tracers and larvae in the upper ocean, and SST distributions commonly used in climatic predictions. Of particular importance is to separate near-inertial waves from turbulence in turbulence closure schemes, as waves are affected by ζ_g and Earth's rotation, while turbulence is not.

Bibliography

Bleck, R., and E. P. Chassignet, 1994: Simulating the oceanic circulation with isopycnic-coordinate models. *The Oceans: Physical-Chemical Dynamics and Human Impact*, S. K. Majumdar et al., Eds., The Pennsylvania Academy of Science, 17-39.

Bleck, R., H. P. Hanson, D. Hu, and E. B. Kraus, 1989: Mixed layer-thermocline interaction in a three-dimensional isopycnic coordinate model. *J. Phys. Oceanogr.*, **19**, 1417–1439.

Boyd, J., 1987: Improved depth and temperature conversion equations for Sippican AXBTs. *J. Atmos. Oceanic Technol.*, **4**, 545–551.

Bühler, 0., and M. E. McIntyre, 2005: Wave capture and wave–vortex duality. *J. Fluid Mech.*, **534**, 67-95, doi:10.1017/S0022112005004374.

Bretherton, F. P., and C. J. R. Garrett, 1969: Wavetrains in inhomogeneous moving media. *Proc. Roy. Soc. A.*, **302**, 529-554.

Brooks, D. A., 1983: The wake of Hurricane Allen in the western Gulf of Mexico. *J. Phys. Oceanogr.*, **13**, 117–129.

Carton X. J., and B. Legras, 1994: The life-cycle of tripoles in 2D incompressible flows. *J. Fluid Mech.*, **267**, 53-82.

Chang, S. and R. Anthes, 1978: Numerical simulations of the ocean's nonlinear baroclinic response to translating hurricanes. *J. Phys. Oceanogr.*, **8**, 468–480.

Chassignet, E. P., L. T. Smith, R. Bleck, and F. O. Bryan, 1996: A model comparison: Numerical simulations of the North and equatorial Atlantic oceanic circulation in depth and isopycnic coordinates. *J. Phys. Oceanogr.*, **26**, 1849-1867.

Chérubin, L. M., Y. Morel, and E. P. Chassignet, 2006: Loop Current ring shedding: The formation of cyclones and the effect of topography. *J. Phys. Oceanogr.*, **36**, 569–591.

Cushman-Roisin, B., B. Tang, and E. P. Chassignet, 1990: Westward motion of mesoscale eddies. *J. Phys. Oceanogr.*, **20**, 758-768.

D'Asaro, E., 1985: Upper ocean temperature structure, inertial currents, and Richardson numbers observed during strong meteorological forcing. *J. Phys. Oceanogr.*, **15**, 943-962.

D'Asaro, E., 2003: The ocean boundary layer below Hurricane Dennis. *J. Phys. Oceanogr.*, **33**, 561-579.

Danioux, E., and P. Klein, 2008: A resonance mechanism leading to wind-forced motions with a 2*f* Frequency. *J. Phys. Oceanogr.*, **38**, 2322–2329.

DeMaria, M. and J. Kaplan, 1994: Sea surface temperature and the maximum intensity of Atlantic tropical cyclones. *J. of Climate*, **7**, 1324–1334.

DeMaria, M., M. Mainelli, L. K. Shay, J. Knaff, and J. Kaplan, 2005: Further improvements to the statistical hurricane intensity prediction scheme. *Wea. and Forecasting*, **20**, 531-543.

Donelan, M. A., B. K. Haus, N. Reul, W. J. Plant, M. Stiassnie, H. C. Graber, O. B. Brown, and E. S. Saltzman, 2004: On the limiting aerodynamic roughness of the ocean in very strong winds. *Geophys. Res. Lett.*, **31**, L18306, doi:10.1029/2004GL019460.

Elliot, B. A., 1982: Anticyclonic rings in the Gulf of Mexico. *J. Phys. Oceanogr.*, **12**, 1292–1309.

Emanuel, K. A., 1986: An air-sea interaction theory for tropical cyclones. Part I: steady-state maintenance. *J. Atmos. Sci.*, **43**, 585-604.

Emanuel, K. A., 1988: The maximum intensity of hurricanes. *J. Atmos. Sci.*, 45, 1143-1155.

Emanuel, K. A. 1999: Thermodynamic control of hurricane intensity. *Nature*, **401**, 665-669.

Emanuel, K. A., 2001: Contribution of tropical cyclones to meridional heat transport by the oceans. *J. Geophys. Res.*, **106**, 14771–14781.

Emanuel, K. A., C. DesAutels, C. Holloway, and R. Korty, 2004: Environmental control of tropical cyclone intensity. *J. Atmos. Sci.*, **61**, 843-858.

Ertel H., 1942: Ein neuer hydrodynamischer Wirbelsatz (A new scalar to characterize hydrodynamic eddies). *Meteor. Z.*, **59**, 271-281.

Flierl G. R., 1987: Isolated eddy models in geophysics. *Annu. Rev. Fluid Mech.*, **19**, 493-530.

Geisler, J. E., 1970: Linear theory on the response of a two layer ocean to a moving hurricane. *Geophys. Fluid Dyn.*, **1**, 249-272.

Gill, A. E., 1982: *Atmosphere–Ocean Dynamics*. Academic Press, 662 pp.

Gill, A. E., 1984: On the behavior of internal waves in the wake of storms. *J. Phys. Oceanogr.*, **14**, 1129–1151.

Goni, G. J, S. Garzoli, and D. Olson, 1996: Dynamics of the Brazil/Malvinas confluence based on inverted echo sounders and altimetry. *J. Geophys. Res.*, **95**, 22103–22120.

Gonella, J., 1972: A rotary component method for analyzing meteorological and oceanographic time series. *Deep-Sea Res.*, **19**, 833-846.

Greatbatch, R. J., 1984: On the response of the ocean to a moving storm: parameters and scales. *J. Phys. Oceanogr.*, **14**, 59–78.

Griffies, S. M., R. C. Pacanowski, and R. W. Hallberg, 2000: Spurious diapycnal mixing associated with advection in a *z*-coordinate ocean model. *Mon. Wea. Rev.*, **128**, 538-564.

Halliwell Jr. G. R., L. K. Shay, J. Brewster, and W. Teague, 2009: Evaluation and sensitivity analysis of an ocean model to hurricane Ivan in the northern Gulf of Mexico. *Mon. Wea. Rev.* (Submitted).

Halliwell Jr. G. R., L. K. Shay, S. D. Jacob, O. M. Smedstad, and E. W. Uhlhorn, 2008: Improving ocean model initialization for coupled tropical cyclone forecast models using GODAE nowcasts. *Mon Wea. Rev.*, **136**, 2576-2591.

Hamilton, P., 1992: Lower continental slope cyclonic eddies in the central Gulf of Mexico. *J. Geophys. Res.*, **97**, 2185–2200.

Hofmann, E. E. and S. J. Worley, 1986: An investigation of the circulation of the Gulf of Mexico. *J. Geophys. Res.*, **91**, 14221–14236.

Holland, G. J., 1997: The maximum potential intensity of tropical cyclones. *J. Atmos. Sci.*, **54**, 2519-2541.

Hong, X., S. W. Chang, S. Raman, L. K. Shay, and R. Hodur, 2000: The interaction between Hurricane Opal (1995) and a warm core ring in the Gulf of Mexico. *Mon. Wea. Rev.*, **128**, 1347–1365.

Huang, N. E., 1986: An estimate of the influence of breaking waves on the dynamics of the upper ocean. *Wave dynamics and radio probing of the ocean surface*, O. M. Phillips and K. Hasselmann, Eds., Plenum Press, 295–313.

Jacob, S. D. and L. K. Shay, 2003: The role of mesoscale features on the tropical cyclone–induced mixed layer response: a case study. *J. Phys. Oceanogr.*, **33**, 649–676.

Jacob, S. D., L. K. Shay, A. J. Mariano, and P. G. Black, 2000: The 3D mixed layer response to Hurricane Gilbert. *J. Phys. Oceanogr.*, **30**, 1407–1429.

Jaimes, B., and L. K. Shay, 2009a: Mixed layer cooling in mesoscale oceanic eddies during hurricanes Katrina and Rita. *Mon. Wea. Rev.*: In Press, DOI: 10.1175/2009MWR2849.1.

Jaimes, B., and L. K. Shay, 2009b: Near-inertial wave wake of hurricanes Katrina and Rita over mesoscale oceanic eddies. *J. Phys. Oceanogr.*: Accepted.

Jarosz, E., D. A. Mitchell, D. W. Wang, and W. J. Teague, 2007: Bottom-up determination of air-sea momentum exchange under a major tropical cyclone. *Science*, **315**, 1707–1709.

Johnson, G.C., 1995: Revised XCTD fall-rate equation coefficients from CTD data. *J. Atmos. Oceanic Technol.*, **12**, 1367–1373.

Knabb, R. D., D. P. Brown, and J. R. Rhome, 2006: Tropical cyclone report: Hurricane Rita (18-26 September 2005). Tech. Rep. National Hurricane Center, National Oceanographic and Atmospheric Administration, 33 pp. (Available online at http://www.nhc.noaa.gov/pdf/TCR-AL182005_Rita.pdf).

Knabb, R. D., J. R. Rhome, and D. P. Brown, 2005: Tropical cyclone report: Hurricane Katrina (23-30 August 2005). Tech. Rep. National Hurricane Center, National Oceanographic and Atmospheric Administration, 43 pp. (Available online at http://www.nhc.noaa.gov/pdf/TCR-AL122005_Katrina.pdf).

Kundu, P. K., and R. E. Thomson, 1985: Inertial oscillations due to a moving front. *J. Phys. Oceanogr.*, **15**, 1076–1084.

Kunze, E., 1985: Near-inertial wave propagation in geostrophic shear. *J. Phys. Oceanogr.*, **15**, 544–565.

Kunze, E., 1986: The mean and near-inertial velocity fields in a warm-core ring. *J. Phys. Oceanogr.*, **16**, 1444–1461.

Kunze, E., and T. B. Sanford, 1984: Observations of near-inertial waves in a front. *J. Phys. Oceanogr.*, **14**, 566–581.

Kunze, E., R. W. Schmitt, and J. M. Toole, 1995: The energy balance in a warm-core ring's near-inertial critical layer. *J. Phys. Oceanogr.*, **25**, 942–957.

Klein, P., and A. Treguier, 1993: Inertial resonance induced by an oceanic jet. *J. Phys. Oceanogr.*, **23**, 1897–1915.

Klein, P., and B. L. Hua, 1988: Mesoscale heterogeneity of the wind-driven mixed layer: influence of a quasigeostrophic flow. *J. Mar. Res.*, **46**, 495–525.

Kraus, E. B., and J. S. Turner, 1967: A one-dimensional model of the seasonal thermocline. II: The general theory and its consequences, *Tellus*, **19**, 98-105.

Large, W. G. and S. Pond, 1981: Open ocean momentum flux measurements in moderate to strong wind. *J. Phys. Oceanogr.*, **11**, 324–336.

Leaman, K. D., 1976: Observations of the vertical polarization and energy flux of near-inertial waves. *J. Phys. Oceanogr.*, **6**, 894–908.

Leaman, K., and T. Sanford, 1975: Vertical energy propagation of inertial waves: A vector spectral analysis of velocity profiles. *J. Geophys. Res.*, **80**(15), 1975–1978.

Lee, D.-K., and P. P. Niiler, 1998: The inertial chimney: The near-inertial energy drainage from the ocean surface to the deep layer, *J. Geophys. Res.*, **103**(C4), 7579–7591.

Leipper, D. and D. Volgenau, 1972: Hurricane heat potential of the Gulf of Mexico. *J. Phys. Oceanogr.*, **2**, 218–224.

Linden, P. F., 1975: The deepening of a mixed layer in a stratified fluid. *J. Fluid Mech.*, 71, 385–405.

Lumpkin, R. and M. Pazos, 2007: Measuring surface currents with Surface Velocity Program drifters: the instrument, its data, and some recent results. *Lagrangian Analysis and Prediction of Coastal and Ocean Dynamics*, Griffa, A., A. Kirwan, A. Mariano, T. Ozgokmen, and T. Rossby, Eds., Cambridge University Press, U.K., 39–67.

Mainelli, M., 2000: *On the role of the upper ocean in tropical cyclone intensity change*. M.S. thesis, University of Miami, Miami, FL 22149, 75 pp.

Mainelli, M., M. DeMaria, L. K. Shay, and G. Goni, 2008: Application of Oceanic Heat Content Estimation to Operational Forecasting of Recent Atlantic Category 5 Hurricanes. *Wea. Forecasting*, **23**, 3–16.

Malkus, J. S., and H. Riehl, 1960: On the dynamics and energy transformations in steady-state hurricanes. *Tellus*, **12**, 1-20.

Mariano, A. J. and O. B. Brown, 1992: Efficient objective analysis of dynamically heterogeneous and nonstationary fields via the parameter matrix. *Deep-Sea Res.*, **39**, 1255–1271.

Mayer, D. A., H. O. Mofjeld, and K. D. Leaman, 1981: Near-inertial internal waves observed on the outer shelf in the Middle Atlantic Bight in the wake of hurricane Belle. *J. Phys. Oceanogr.*, **11**, 87–106.

Mied, R. P., C. Y. Shen, C. L. Trump, and G. J. Lindemann, 1986: Internal-inertial waves in a Sargasso Sea front. *J. Phys. Oceanogr.*, **16**, 1751–1762.

Mied, R. P., G. J. Lindemann, and C. L. Trump, 1987: Inertial wave dynamics in the North Atlantic Subtropical Zone, *J. Geophys. Res.*, **92**(C12), 13 063–13 074.

Miles, J. W., 1961: On the stability of heterogeneous shear flows. *J. Fluid Mech.*, **10**, 496-508.

Miller, B. I., 1958: On the maximum intensity of hurricanes. *J. Meteor.*, **15**, 184-195.

Molinari, R. L., and J. Morrison, 1988: The separation of the Yucatan Current from the Campeche Bank and the intrusion of the Loop Current into the Gulf of Mexico. *J. Geophys. Res.,* **93**, 10645-10654.

Mooers C. N. K., 1975: Several effects of a baroclinic current on the cross-stream propagation of inertial-internal waves. *Geophys. Fluid Dyn.*, **6**, 245–275.

Mooers C. N. K., and G. Maul, 1998: Intra-Americas sea circulation. *The Sea*, A. Robinson and K. H. Brink, Eds., The Global Coastal Ocean, Regional Studies and Syntheses, Vol. 11, Wiley and Sons, 183–208.

Morel, Y., and J. McWilliams, 2001: Effects of isopycnal and diapycnal mixing on the stability of oceanic currents. *J. Phys. Oceanogr.*, **31**, 2280–2296.

Morel, Y., and L. N. Thomas, 2009: Ekman drift and vortical structures. *Ocean Modelling*, **27**, 185-197.

Niiler, P. P., and E. B. Kraus, 1975: One-dimensional models of the upper ocean. *Modelling and Prediction of the Upper Layers of the Ocean*, E.B. Kraus, Ed., Pergamon Press, 143-172.

Nilsson, J., 1995: Energy flux from traveling hurricanes to the oceanic internal wave field. *J. Phys. Oceanogr.*, **25**, 558–573.

Niwa, Y., and T. Hibiya, 1997: Nonlinear processes of energy transfer from traveling hurricanes to the deep ocean internal wave field, *J. Geophys. Res.*, **102**(C6), 12,469–12,477.

Nowlin, W. D. Jr., and J. M. Hubertz, 1972: Contrasting summer circulation patterns for the eastern Gulf. In: *Contributions on the Physical Oceanography of the Gulf of Mexico, Tex. A&M Oceanogr. Stud.*, vol. 2, edited by L. R. A. Capurro and J. L. Reid, pp. 119-138, Gulf Pub. Co.

O'Brien, J. J., 1967: The non-linear response of a two-layer, baroclinic ocean to a stationary, axially-symmetric hurricane: Part II. Upwelling and mixing induced by momentum transfer. *J. Atmos. Sci.*, **24**, 208-215.

O'Brien, J. J., and R. O. Reid, 1967: The non-linear response of a two-layer, baroclinic ocean to a stationary, axially-symmetric hurricane: Part I. Upwelling induced by momentum transfer. *J. Atmos. Sci.*, **24**, 197-207.

Olbers, D. J., 1981: The propagation of internal waves in a geostrophic current. *J. Phys. Oceanogr.*, **11**, 1224–1233.

Palmen, E., 1948: On the formation and structure of the tropical hurricane. *Geophysica*, **3**, 26-38.

Pollard, R. T., P. B. Rhines, and R. O. R. Y. Thompson, 1973: The deepening of the wind-mixed layer. *Geophys. Fluid Dyn.*, **3**, 381-404.

Powell, M. D., S. H. Houston, and T. A. Reinhold, 1996: Hurricane Andrew's landfall in South Florida. Part I : standardizing measurements for documentation of surface wind fields. *Wea. Forecast.*, **11**, 304–328.

Powell, M. D., P. J. Vickery, and T. A. Reinhold, 2003: Reduced drag coefficient for high wind speeds in tropical cyclones. *Nature*, **422**, 279–283.

Price, J. F., 1981: Upper ocean response to a hurricane. *J. Phys. Oceanogr.*, **11**, 153–175.

Price, J. F., 1983: Internal wave wake of a moving storm. Part I: Scales, energy budget and observations. *J. Phys. Oceanogr.*, **13**, 949–965.

Price, J. F., C. N. K. Mooers, and J. C. Van Leer, 1978: Observation and simulation of storm-induced mixed-layer deepening. *J. Phys. Oceanogr.*, **8**, 582-599.

Price, J. F., R. A. Weller, and R. Pinkel, 1986: Diurnal cycling: Observations and models of the upper ocean response to diurnal heating, cooling, and wind mixing. *J. Geophys. Res.*, **91**(C7), 8411-8427.

Rio, M.-H., and F. Hernandez, 2004: A mean dynamic topography computed over the world ocean from altimetry, in situ measurements, and a geoid model. *J. Geophys. Res.*, **109**, C12032, doi:10.1029/2003JC002226.

Rogers, R., S. Aberson, M. Black, P. Black, J. Cione, P. Dodge, J. Dunion, J. Gamache, J. Kaplan, M. Powell, L. K. Shay, N. Surgi, and E. Uhlhorn, 2006: The intensity forecasting experiment (IFEX), a NOAA multiple year field program for improving intensity forecasts. *BAMS*, **87**(11), 1523-1537.

Rossby C. -G., 1938: On the mutual adjustment of pressure and velocity distribution in simple current systems, 2. *J. Mar. Res.*, **1**, 239–263.

Rossby, H. T., and T. B. Sanford, 1976: A study of velocity profiles through the thermocline. *J. Phys. Oceanogr.,* **6,** 766–774.

Rotunno, R., and K. A. Emanuel, 1987: An air-sea interaction theory for tropical cyclones. Part II: evolutionary study using a nonhydrostatic axisymetric numerical model. *J. Atmos. Sci.*, **44**, 542-561.

Rubenstein, D. M., 1983: Vertical dispersion of inertial waves in the upper ocean, *J. Geophys. Res.*, **88**(C7), 4368–4380.

Rubenstein, D. M., and G. O. Roberts, 1986: Scattering of inertial waves by an ocean front. *J. Phys. Oceanogr.*, **16**, 121–131.

Scharroo, R., W. H. F. Smith, and J. L. Lillibridge, 2005: Satellite altimetry and the intensification of hurricane Katrina, *Eos Trans. AGU*, **86**(40), doi:10.1029/2005EO400004.

Schmitz, W. J. Jr, 2005: Cyclones and westward propagation in the shedding of anticyclonic rings from the Loop Current, in *Circulation in the Gulf of Mexico: observations and models*, edited by W. Sturges and A. Lugo-Fernandez, Geophysical Monograph Series 161, 241-261, American Geophysical Union.

Shay, L. K., 2009: Upper ocean structure: Response to strong forcing events. *Encyclopedia of Ocean Sciences*, J. Steele et al., Eds., Elsevier Press Int.,4619-4637. doi:10.1016/B978-012374473-9.00628-7.

Shay, L. K., and R. L. Elsberry, 1987: Near-inertial ocean current response to Hurricane Frederic. *J. Phys. Oceanogr.*, **17**, 1249–1269.

Shay, L. K. and S. D. Jacob, 2006: Relationship between oceanic energy fluxes and surfaces winds during tropical cyclone passage. *Atmosphere-Ocean Interactions*, Perrie,W., Ed., WIT Press, Southampton, U.K., No. 2 in Advances in Fluid Mechanics, 115–142.

Shay, L. K., and E. W. Uhlhorn, 2008: Loop Current response to Hurricanes Isidore and Lili. *Mon. Wea. Rev.*, **136,** 3248-3274.

Shay, L. K., R. L. Elsberry, and P. G. Black, 1989: Vertical structure of the ocean current response to a hurricane. *J. Phys. Oceanogr.*, **19**, 649–669.

Shay, L. K., P. G. Black, A. J. Mariano, J. D. Hawkins, and R. L. Elsberry, 1992: Upper ocean response to Hurricane Gilbert. *J. Geophys. Res.*, 97(C12), 20,227–20,248.

Shay, L. K., A. J. Mariano, S. D. Jacob, and E. H. Ryan, 1998: Mean and near-inertial response to hurricane Gilbert. *J. Phys. Oceanogr.*, **28**, 858–889.

Shay, L. K., G. J. Goni, and P. G. Black, 2000: Effects of a warm oceanic feature on Hurricane Opal. *Mon. Wea. Rev.*, **128**, 1366–1383.

Sjöberg, B., and A. Stigebrant, 1992: Computation of the geographical distribution of the energy flux to mixing processes via internal tides and the associated vertical circulation in the oceans. *Deep Sea Res.*, **39**, 269–291, 1992.

Stern, M. E., 1965: Interaction of a uniform wind stress with a geostrophic vortex. *Deep-Sea Res.*, **12**, 355-367.

Sturges, W. and R. Leben, 2000: Frequency of ring separations from the Loop Current in the Gulf of Mexico: A revised estimate. *J. Phys. Oceanogr.*, **30**, 1814–1819.

Sun, D., R. Gautam, G. Cervone, Z. Boybeyi, and M. Kafatos, 2006: Comment on "Satellite altimetry and the intensification of hurricane Katrina", *Eos Trans. AGU*, **87**, doi:10.1029/2006EO080006.

Teague, W.J., E. Jarosz, D.W. Wang, and D.A. Mitchell, 2007: Observed oceanic response over the upper continental slope and outer shelf during Hurricane Ivan. *J. Phys. Oceanogr.*, **37**, 2181-2206.

Vukovich, F. M., 2007: Climatology of ocean features in the Gulf of Mexico using satellite remote sensing data. *J. Phys. Oceanogr.*, **37**, 689–707.

Walker, N., R. R. Leben, and S. Balasubramanian, 2005: Hurricane forced upwelling and chlorophyll a enhancement within cold core cyclones in the Gulf of Mexico. *Geophys. Res. Letters*, 32, L18610, doi: 10.1029/2005GL023716.

Walker, N. , S. Myint, A. Babin, and A. Haag, 2003: Advances in satellite radiometry for the surveillance of surface temperatures, ocean eddies and upwelling processes in the Gulf of Mexico using GOES-8 measurements during summer, *Geophys. Res. Letters,* **30**(16), 1854, doi:10.1029/2003GL017555.

Weller, R. A., 1982: The relation of near-inertial motions observed in the mixed layer during the JASIN (1978) Experiment to the local wind stress and to the quasi-geostrophic flow field. *J. Phys. Oceanogr.*, **12**, 1122–1136.

Zavala-Hidalgo, J., S. L. Morey, and J. J. O'Brien, 2003: Cyclonic eddies northeast of the Campeche Bank from altimetry data. *J. Phys. Oceanogr.*, **33**, 623–629.

Zervakis, V., and M. D. Levine, 1995: Near-inertial energy propagation from the mixed layer: Theoretical considerations. *J. Phys. Oceanogr.*, **25**, 2872–2889.